UNIVERSITY OF CALIFORNIA

Los Angeles

Resonant Laser Plasma Interactions and Electron Acceleration

A dissertation submitted in partial satisfaction of the
requirements for the degree
Doctor of Philosophy in Electrical Engineering

by

Daniel Francis Gordon

1999

The dissertation of Daniel Francis Gordon is approved.

John M. Dawson

Francis F. Chen

Warren B. Mori

Chan Joshi, Committee Chair

University of California, Los Angeles

1999

Contents

List of Figures

ACKNOWLEDGMENTS

I would like to express my gratitude to a number of people in connection with this dissertation.

The most instrumental figure was of course my advisor, Chan Joshi. I owe him a great debt for his guidance and for providing me with the opportunity to be part of an outstanding group. On the experimental side, my mentor has been Chris Clayton. I would like to thank Chris for his expert help and advice regarding countless experimental problems. Another key figure on the experimental side has been Ken Marsh. Ken was indispensible when it came to building, maintaining, and repairing the experimental apparatus. On the theory side, I would like to thank Warren Mori for helping me learn to do particle simulations, and for helping me adjust to a theoretical "second half" of my graduate career.

Apart from my experience at UCLA, I have also had the good fortune to work with colleagues from Europe on experiments at the Rutherford Appleton Laboratories (RAL) in England. I would like to thank the groups from Imperial College and Ecole Poytechnique for inviting me to participate in these experiments. I would also like to thank RAL for the use of their excellent facility.

VITA

March 19, 1969	Born, Thousand Oaks, California
1991	B.S., Electrical Engineering, University of California, Los Angeles
1994	M.S., Electrical Engineering, University of California, Los Angeles
1991–99	Graduate Student Researcher, Departments of Physics and Electrical Engineering, University of California, Los Angeles

PUBLICATIONS

D. Gordon, K.-C. Tzeng, C.E. Clayton, A.E. Dangor, V. Malka, K.A. Marsh, A. Modena, W.B. Mori, P. Muggli, Z. Najmudin, D. Neely, C. Danson, C. Joshi, "Observation of Electron Energies Beyond the Linear Dephasing Limit from a Laser-Excited Relativistic Plasma Wave", Physical Review Letters **80**, 10, p. 2133 (1998)

D. Gordon, C.E. Clayton, T. Katsouleas, W.B. Mori, C. Joshi, "Microbunching of Relativistic Electrons Using a Two-Frequency Laser", Physical Review E **57**, 1, p. 1035 (1998)

C.E. Clayton, K.-C. Tzeng, D. Gordon, P. Muggli, W.B. Mori, C. Joshi, V. Malka, Z. Najmudin, A. Modena, D. Neely, A.E. Dangor, "Plasma Wave Generation in a Self-Focused Channel of a Relativistically Intense Laser Pulse", Physical Review Letters **81**, 1, p. 100 (1998)

A.K. Lal, D. Gordon, K. Wharton, C.E. Clayton, K.A. Marsh, W.B. Mori, C. Joshi, M.J. Everett, T.W. Johnston, "Spatio-Temporal Dynamics of the Resonantly Excited Relativistic Plasma Wave Driven by a CO_2 laser", Physics of Plasmas **4**, 5, p. 1434 (1997)

D. Gordon, A. Lal, K. Wharton, C.E. Clayton, C. Joshi, "Two-Dimensional Cherenkov Emission Array for Studies of Relativistic Electron Dynamics in a Laser Plasma", Review of Scientific Instruments, **68**, 1, p. 358 (1997)

A. Lal, D. Gordon, K. Marsh, K. Wharton, C.E. Clayton, C. Joshi, "Exact forward scattering of a CO_2 Laser Beam from a Relativistic Plasma Wave by Time Resolved Frequency Mixing in $AgGaS_2$", Review of Scientific Instruments, **68**, 1, p. 690 (1997)

M.J. Everett, A. Lal, D. Gordon, K. Wharton, C.E. Clayton, W.B. Mori, C. Joshi, "Evolution of Stimulated Raman into Stimulated Compton scattering of Laser Light via Wave-Breaking of Plasma Waves", Physical Review Letters **74**, 8, p. 1355 (1995)

A. Lal, K. Wharton, D. Gordon, M.J. Everett, C.E. Clayton, C. Joshi, "Measurements of the Beatwave Dynamics in Time and Space", Proceedings of the 1995 Particle Accelerator Conference **2**, p. 767 (1995)

D. Gordon, K. Wharton, C.E. Clayton, M.J. Everett, C. Joshi, "A Novel Technique for Probing the Transverse Interactions Between an Electron Beam and a Plasma", Proceedings of the 1995 Particle Accelerator Conference **2**, p. 770 (1995)

C.E. Clayton, M.J. Everett, A. Lal, D. Gordon, K.A. Marsh, C. Joshi, "Acceleration and Scattering of Injected Electrons in Plasma Beat Wave Accelerator Experiments", Physics of Plasmas **1**, 5, p. 1753 (1994)

M. Everett, A. Lal, D. Gordon, C.E. Clayton, K.A. Marsh, C. Joshi, "Trapped Electron Acceleration by a Laser-Driven Relativistic Plasma Wave", Nature **368**, 6471, p. 527 (1994)

ABSTRACT OF THE DISSERTATION

Resonant Laser Plasma Interactions and Electron Acceleration

by

Daniel Francis Gordon

Doctor of Philosophy in Electrical Engineering

University of California, Los Angeles, 1999

Professor Chan Joshi, Chair

The interaction between intense laser radiation and a plasma is often dominated by the generation of large amplitude plasma waves. These plasma waves can drastically affect both the plasma particles of which they are composed and the laser radiation by which they are driven. This dissertation addresses two facets of these processes. In part I, the acceleration of electrons by highly nonlinear plasma waves is addressed. It is shown experimentally that energy gains exceeding the dephasing limit of linear theory are possible. In part II, the recent theory of electromagnetically induced transparency in a plasma is examined. It is found that the requirements of causality do not allow for the transmission of electromagnetic radiation through an overdense plasma as conceived in the original theory. However, it is possible for radiation below the cutoff frequency to be generated by a plasma. Also, a Raman-type instability is found to afflict electromagnetic waves in a plasma even when the density exceeds quarter-critical.

Chapter 1

Introduction

The availability of very high power short pulse lasers has created new experimental opportunities for scientific researchers studying the interaction of radiation with matter. These experiments inevitably involve the interaction between laser radiation and plasma since the target is bound to be ionized as higher and higher intensities are achieved. One important aspect of the laser-plasma interaction is the possibility of generating large amplitude plasma waves, whose high phase velocity and enormous axial fields make them a suitable structure for the acceleration of charged particles.

Part I of this dissertation is concerned with plasma based accelerators. The use of plasma waves as accelerating structures was originally proposed by Tajima and Dawson in 1979 [1]. The need for plasma based accelerators follows from the fact that conventional accelerators are limited to an acceleration gradient between 10 and 100 MeV/m because of RF breakdown in the cavity. A structure composed of plasma, already being ionized, suffers from no such limitation. Accelerating gradients on the order of 10 GeV/m have been observed in a number of experiments [2, and references therein], and are again demonstrated in this

dissertation. In addition, it is shown that energies in excess of the dephasing limit imposed by linear theory are possible when the plasma wave is driven to wavebreaking.

Part II of this dissertation is concerned with electromagnetically induced transparency (EIT) in a plasma. The original proposal for EIT in a plasma, which was put forth by S.E. Harris in 1996 [3], suggests that an electromagnetic wave with a frequency below cutoff might be transmitted in the presence of an intense pump wave with frequency above cutoff. The essence of EIT is the same as that of Raman scattering in that both processes rely on the driving of a plasma wave by photon pressure and the acceleration or deceleration of photons by a plasma wave. EIT is distinct from Raman scattering, however, in that the regime of interest for EIT is $n > n_c/4$ where n is the plasma density and n_c is the critical density. The regime of interest for Raman scattering has traditionally been $n < n_c/4$, the exact opposite. EIT is also distinguished by the fact that the energy contained in each frequency is conserved, whereas in the case of Raman scattering energy is generally drained from the carrier frequency to feed the sidebands. In this dissertation, the concept of EIT is examined not only from the point of view of the Raman dispersion relation, but also from the point of view of a boundary value problem. It is found that when boundaries are taken into account, the requirements of causality lead to serious limitations on the validity of the EIT concept. Computer simulations are used extensively to corroborate the analysis.

Part I

Nonlinear Acceleration in a Self Modulated Laser Wakefield

Chapter 2

Introduction and Background

2.1 Introduction

Plasma based accelerators can take a number of different forms, depending on how the plasma wave is driven. The simplest laser driven scheme is the laser wakefield accelerator (LWFA), which utilizes an intense pulse of radiation whose pulse-length is chosen to be a half plasma period. The plasma wave takes the form of a wake which follows the laser pulse. The wake is driven by the ponderomotive force

$$\mathbf{F}_{NL} = -\frac{1}{2}\frac{q^2}{m}\nabla\left\langle A^2\right\rangle \tag{2.1}$$

where q and m are the charge and mass of the affected particle and A is the vector potential associated with the laser. The brackets represent averaging over several laser oscillations. The condition on the length of the laser pulse is chosen so that the ponderomotive force interacts resonantly with the plasma. The leading edge of the pulse pushes electrons forward, while the trailing edge pushes electrons backward. The wake will be largest when the backward push coincides with the restoring force exerted by the ions. Also important for accelerator applications

is the phase velocity of wake, which will be approximately equal to the group velocity of the driving laser pulse.

Other laser driven acceleration schemes are variations on the principle of the LWFA. In the plasma beatwave accelerator (PBWA), a two frequency laser beam is used to produce a beam of photons modulated at the plasma frequency. This is equivalent to a repeated application of LWFA pulses. In the self-modulated laser wakefield accelerator (SMLWFA), a single frequency laser several plasma periods long is modulated automatically as it interacts with the plasma. In the one-dimensional limit, this is due to the Raman forward scattering (RFS) instability. The RFS instability results from the fact that the density ripple associated with a small plasma wave causes a similar ripple in the group velocity of photons in the plasma. The phasing is such that photons tend to collect at the positive slope inflection points of the plasma wave. These photons then reinforce the plasma wave through the ponderomotive force. The resulting feedback loop causes both the amplitude of the plasma wave and the depth of the laser modulation to grow exponentially until they saturate.

In this dissertation, we present the results of experiments on the SMLWFA in which electrons were captured from the thermal distribution of a tunnel-ionized plasma and accelerated in the plasma to form a directed beam of high energy electrons. Table 2.1 gives the values of some typical experimental parameters. The electron beam was energy analyzed using a large electromagnet in combination with an array of solid state detectors. This measurement was complemented by frequency and spatial resolution of the plasma wave via Thomson scattering, which provides a direct measurement of acceleration gradients in the plasma.

Table 2.1: Experimental Parameters

Laser Wavelength	1.053 μm
Laser Energy	20 J
Laser Pulse Length	1 ps
Laser Power	20 TW
Laser Spot Diameter	20 μm
Laser Intensity	5×10^{18} W/cm^2
Quiver Momentum	$2mc$
Gas	Helium
Backing Pressure	20 bar
Gas Jet Diameter	5 mm
Plasma Density	1.5×10^{19} cm^{-3}
Plasma Frequency	2.2×10^{14} rad/s
Wavebreaking Field	3.7 GV/cm
Group Velocity of 1 μm Light	$\gamma = 8.5$

The electron measurements revealed evidence of nonlinear acceleration mechanisms which result in energy gains greater than those predicted by linear theory. The Thomson scattering measurements resulted in evidence of self-focusing and the generation of plasma waves in the laser-induced channels.

2.2 Spatio-Temporal Theory of RFS

When a laser beam propagates through a plasma, backward propagating plasma fluctuations can only interact with it for a length of time on the order of the laser pulse length. Hence, if the laser pulse is short compared to the length of the interaction region, backward propagating instabilities will grow very little compared with forward propagating instabilites. In the experiments discussed in this dissertation, the laser pulse was about 300 μm long while the Rayleigh

length of the laser was about 600 μm long. Under these conditions, RFS has a chance to dominate the interaction.

The standard purely temporal analysis of RFS is inadequate when the laser pulse length becomes too short. The laser's rising edge is essentially a boundary which affects the solution to any differential equations describing the laser's evolution near that boundary. When the pulse is very short, every point is near the boundary, and a spatio-temporal theory is required. Such an analysis has been carried out by Mori *et al.* [4, 5]. We outline the results here.

In any theory of RFS, one begins with a wave equation for the laser field and a harmonic oscillator equation for the plasma response. In the purely temporal theory, one would Fourier-analyze these equations, taking wavenumbers to be real, and determine the growth rate by examining the imaginary part of the frequency. In the spatio-temporal analysis, by contrast, all quantities were supposed to be of the form

$$\phi = \phi_0(\psi, \tau) e^{-i[k\psi + (\omega - k)\tau]} \tag{2.2}$$

where ψ and τ are the laser coordinates defined by $\psi = t - x/c$ and $\tau = t$, and ω and k are taken to be real. This allows one to find equations for the envelope ϕ_0 which can subsequently be simplified using the quasistatic approximation ($\partial_\tau \ll \partial_\psi$) [6]. In the analysis of reference [4], analytical solutions were found using Laplace transform techniques. This allowed specification of the boundary conditions $\phi_0(\psi = 0, \tau) = \phi_0(\psi, \tau = 0) = \phi_n$ and $\partial_\tau \phi_0(\psi, \tau = 0) = 0$. The physical meaning of these boundary conditions is that the noise source, ϕ_n, is initially constant everywhere, and never changes at the head of the laser pulse. The solution for the scalar potential of the plasma response is approximately (taking

$\partial_{\tau\tau} = 0$)

$$\phi = \phi_n H(\psi) H(\tau) I_0(g) \tag{2.3}$$

where H is the Heaviside step function, I_0 is the modified Bessel function of the first kind, and

$$g = \frac{a_0}{(1 + a_0^2/2)} \frac{\omega_p^2}{\omega_0} \sqrt{\frac{\tau\psi}{2}} \tag{2.4}$$

The asymptotic expansion of I_0 for large g gives the overall gain as $G = e^g/\sqrt{2\pi g}$. We see that the gain depends exponentially on the geometric mean between the distance from the head of the pulse (ψ) and the amount of time in the plasma (τ). In the non-relativistic limit, the gain also depends exponentially on both laser intensity and density. However, the relativisitic term $1 + a^2/2$ causes the growth rate to role over at high intensities, and eventually, to diminish. There are two reasons for this. First, the relativistic mass increase makes the plasma more difficult to set in motion. Second, the plasma wavelength becomes longer which makes the ponderomotive force less effective.

2.3 Wavebreaking

The greatest electric field that can be generated by a plasma wave is estimated quite well by the non-relativistic, cold wavebreaking field:

$$E_{\max} = \omega_p \frac{mc}{e} \tag{2.5}$$

Indeed, the amplitude of a plasma wave is often given by the normalized parameter

$$\epsilon = \frac{E}{E_{\max}} \tag{2.6}$$

The field $E_{\max}$ is derived by setting the maximum velocity of a fluid element in the wave equal to the phase velocity of the wave. At this point, large numbers of particles become resonant with the wave and energy is traded between the wave and the particles in an irreversible manner. This results in the generation of high energy electrons and a loss of coherence of the plasma wave. In the experiment, large numbers of high energy electrons were indeed detected, and a broadening in the spectrum of the transmitted laser light was seen as indicative of the loss of wave coherence.

It has been shown [7] that relativistic and nonlinear effects lead to a wave-breaking field greater than $E_{\max}$ by a factor of $\sqrt{2}(\gamma_{\rm ph} - 1)^{1/2}$. Here $\gamma_{\rm ph}$ is the relativistic Lorentz factor associated with the phase velocity of the wave, which can be quite large in laser-excited plasmas. For the experiments considered in this dissertation, $\gamma_{\rm ph} \approx 8.5$ so that in principle one might have $\epsilon \approx 4$. In PIC simulations paralleling the experimental parameters [8], such fields are indeed seen, but only very early in the evolution of the laser pulse. Once wavebreaking occurs, the energy exchange with resonant particles immediately limits the wave amplitude to $\epsilon < 1$. During this initial energy exchange, large numbers of particles are accelerated, but the energies attained are less than those attained later in time after the wave amplitude has been reduced to $\epsilon \approx 0.5$. This is because of complex dynamical phase relationships between the particles and the wave. This subject is addressed at length later in the dissertation.

2.4 Trapped Particles and Dephasing

The energy a particle can gain in a plasma wave is limited not only by the plasma wave amplitude but also by dephasing [9]. The mechanism of dephasing can be understood diagramatically by plotting the phase space trajectories of test particles in a linear plasma wave. Such a diagram is shown in Figure 2.1 for plasma wave parameters pertinent to the experiment. The diagram was generated by pushing particles through a field of the form

$$E = \epsilon E_{\max} \sin \psi \tag{2.7}$$

where $\psi = \omega_p t - k_p x$. The wave amplitude was taken as $\epsilon = 0.5$ and k_p was chosen to give a phase velocity corresponding to $\gamma_{\rm ph} = 8.5$. This corresponds to the group velocity of a 1 μm laser beam in a plasma of density 1.5×10^{19} cm^{-3}.

The horizontal axis in figure 2.1 is the phase of the plasma wave, ψ. The Phases $-180 < \psi < 0$ are accelerating while the phases $0 < \psi < 180$ are decelerating. As illustrated in the figure, dephasing occurs when a particle leaves the accelerating region and begins to lose energy rather than gain it. The dephasing limit gives the maximum energy a particle can gain before this happens. In three dimensions, the plasma wave also generates focusing and defocusing forces which are 90° out of phase with the axial forces. Because of this, only 90° of the accelerating structure is useful, and the dephasing limit is half what it would be in one dimension.

Also illustrated in figure 2.1 is the concept of particle trapping. A trapped particle is one which executes closed orbits in phase space when evaluated in the wave frame. These orbits are all contained within a region bounded by a special

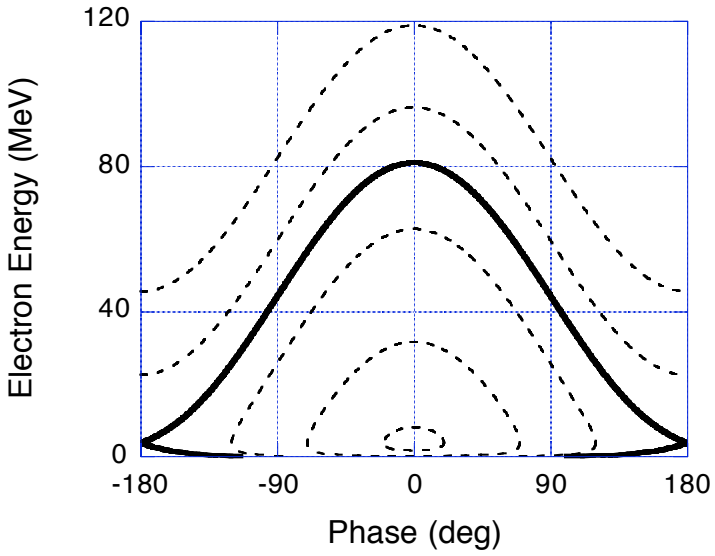

Figure 2.1: Phase space trajectories of test particles in a plasma wave with $\gamma_{\rm ph} = 8.5$ and $\epsilon = 0.5$. The heavy line is the separatrix. The orbits within the separatrix represent trapped particles.

orbit called the *separatrix*, depicted in the figure by a heavy line. The separatrix is the orbit corresponding to a particle with $\psi \to 180$ and $\gamma = \gamma_{\rm ph}$. The lowest point of the separatrix is called the "trapping threshold", since this is the minimum energy a particle must have before it is trapped. In accelerator applications, the trapping threshold is significant since the particle orbits cannot cross the separatrix without some external perturbation. This implies that particles with energies below the trapping threshold are limited to $\gamma < \gamma_{\rm ph}$. Trapped particles can originate either from an external source, or from the hot tail of the plasma's electron distribution function. Trapped particles originating from the background plasma are said to be "self-trapped."

Figure 2.2 zooms in on the low energy region of figure 2.1. We see that the trapping threshold in this case corresponds to a negative momentum, resulting from the fact that the wave is very large and $\gamma_{\rm ph}$ is relatively low. This does not mean, however, that a cold background of electrons will be self-trapped. To illustrate this, we also show the orbit of a fluid element participating in the plasma oscillation. In a cold plasma, all the electrons would lie on this orbit, which is clearly below the separatrix. As the plasma is heated, however, the electron motion is described by a distribution of orbits centered about the fluid orbit. When the distribution overlaps the separatrix, self-trapping can occur. For the case illustrated in figure 2.2, this occurs when the thermal velocity corresponds to a momentum of $\approx 0.3mc$, implying a temperature of

$$T = (\gamma_{\rm th} - 1)\, mc^2 \approx 20 \text{ keV} \tag{2.8}$$

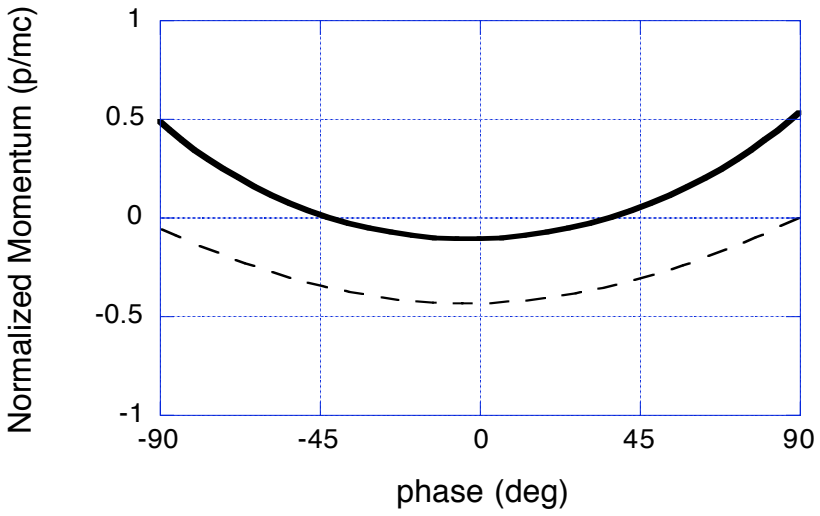

Figure 2.2: Trapping threshold with $\gamma_{\rm ph} = 8.5$ and $\epsilon = 0.5$. The heavy line is the separatrix and the dashed line is the orbit of a fluid element participating in the plasma wave motion. The difference between the two curves therefore determines the temperature required for self-trapping.

2.5 Self Focusing

In three dimensions, an intense laser pulse modifies the refractive index of a plasma such that focusing forces come about [10, 11, 12]. There are two main reasons for this. First, as plasma electrons are expelled radially due to the ponderomotive force, the electron density becomes an increasing function of the radial coordinate. The resulting gradient in the refractive index causes light rays to bend inward. Second, the relativistic mass of the electrons is greatest near the axis where the laser intensity is greatest. This too affects the refractive index of the plasma such that light rays bend inward.

A parameter often used to determine the propensity of a beam for self-focusing is the critical power for relativistic self-focusing, P_c. This is defined as the power for which relativistic focusing forces exactly offset the natural diffraction of the beam. It is given by [2]

$$P_c[\mathrm{GW}] \approx 17\frac{\omega^2}{\omega_p^2} \tag{2.9}$$

where ω is the frequency of the laser and ω_p is the plasma frequency. In the experiment, the laser power was about $20P_c$, and indeed, self focusing was evident since large amplitude plasma waves were observed to persist for up to 12 Rayleigh lengths.

Chapter 3

Experimental Apparatus

The fundamental components of the experiment are a column of gas and an intense laser beam. By merely firing the laser into the gas, a fully ionized plasma is created and an energetic beam of electrons is generated. In these experiments, the laser radiation was provided by the 1.053 μm laser system Vulcan [13] of the Central Laser Facility at the Rutherford Appleton Laboratories (RAL). Vulcan provided up to 20 J of energy in a nominally 1 ps laser pulse. The beam could be focused to a 20 μm diameter spot using an $f/4.5$ off axis-paraboloid mirror. The column of gas was created using a supersonic gas jet. The gas jet backing pressure was typically about 25 bar. Opening the solenoid actuated valve created a laminar plume of helium gas 4 mm in diameter with an experimentally inferred density of about 1.5×10^{19} cm^{-3}. The laser was usually focused onto the edge of the gas.

An overview of the experiment with the three main diagnostics is shown in figure 3.1. After passing through the plasma, the main laser beam is reflected by a pellicle with a small hole in the center. It is then refocused into a spectrometer so that any sidebands generated in the plasma can be observed. The electrons

transmitted by the hole in the pellicle are passed through a dipole magnet of the Browne and Buechner type. The magnet disperses the electron energies onto an image plane where an array of silicon surface barrier detectors (SSBD) measures the electron flux at various discrete energies. Also shown is a transversely probing green laser which is used for Thomson scattering. The scattered light is imaged and frequency resolved which allows the amplitude, frequency, and spatial extent of certain plasma modes to be determined.

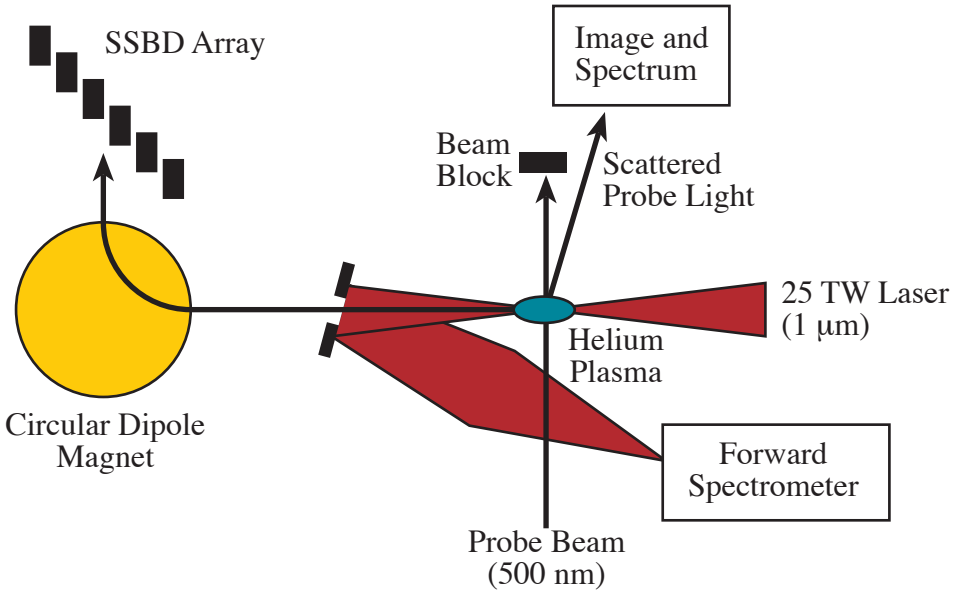

Figure 3.1: Schematic of the Experimental Setup

In what follows we describe in detail the electron diagnostic and the Thomson scattering diagnostic, since these are central to the material presented in this dissertation. We do not describe the Vulcan laser, but rather regard it as a black box capable of delivering its output to the target on demand. During the experiment, this was indeed the case thanks to the technical staff at RAL.

3.1 Electron Diagnostic

3.1.1 Electron Spectrometer Theory

The centerpiece of the electron diagnostic is a Browne and Buechner type dipole magnet, which utilizes circular pole pieces to resolve a broad range of electron energies. Figure 3.2 depicts a particle traversing the magnetic field, which is assumed uniform throughout a cylindrical region. A line drawn through the center of the circle defined by the magnetic field and the center of the circle defined by the particle trajectory forms an axis of symmetry for the system. This implies that a ray entering the field region at normal incidence will also exit at normal incidence. It further follows that any rays entering the magnet at normal incidence will appear to emanate from a virtual source located at the center of the magnet. Making use of these realizations, one can show using simple geometry that the exit angle θ (as defined in figure 3.2) is given by

$$\theta = 2\tan^{-1}\frac{R}{r} \tag{3.1}$$

Since r is just the Larmor radius of the particle, this becomes

$$\theta = 2\tan^{-1}\frac{e}{mv}\frac{RB}{\gamma} \tag{3.2}$$

where γ is the relativistic Lorentz factor associated with the particle and v is its speed. This gives a one to one relationship between exit angle and energy assuming all rays are normally incident.

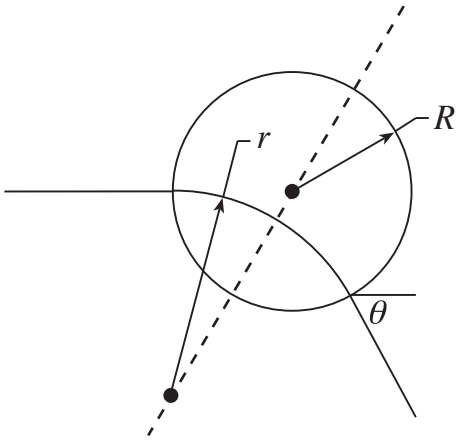

Figure 3.2: Normally incident ray entering a circular magnetic field. The dotted line is an axis of symmetry.

Ray Matrix Analysis

The case where the rays do not all enter the magnet at normal incidence can be analyzed using the well known theory of the sector magnet [14]. If the spot size of the electron beam is small compared to the pole piece radius, R, then a sufficiently narrow band of energies propagates through the magnet as if through an equivalent sector magnet with swept angle θ, where θ is determined from equation 3.2.

For the purposes of propagation through a sector magnet, the state of a ray can be specified using two separate vectors:

$$\mathbf{h} = \begin{pmatrix} x \\ x' \\ \delta \end{pmatrix} \quad \mathbf{v} = \begin{pmatrix} y \\ y' \end{pmatrix} \tag{3.3}$$

where the prime indicates differentiation with respect to z. The z-coordinate represents arc length along the central trajectory. The x-coordinate represents

distance from the central trajectory along a vector in the plane of the bend. The y-coordinate represents distance from the central trajectory along a vector normal to the plane of the bend. The coordinate δ is the relative momentum variation $\Delta p/p$ where p is the momentum of the ray defining the central (normally incident) trajectory. The designations "h" and "v" correspond to horizontal and vertical respectively. The separation of the state vector into these two parts reflects the expectation that the horizontal and vertical states of the beam will evolve independently, and that the momentum of a ray will affect only its horizontal evolution.

With the state of an arbitrary ray described in vector form, the propagation of that ray through a system of sector magnets and drift spaces can be represented by a sequence of matrix multiplications. The matrices corresponding to a drift space are:

$$D_h(z) = \begin{pmatrix} 1 & z & 0 \\ 0 & 1 & 0 \\ 0 & 0 & 1 \end{pmatrix} \quad D_v(z) = \begin{pmatrix} 1 & z \\ 0 & 1 \end{pmatrix} \tag{3.4}$$

and the matrices for a sector magnet are

$$S_h(\theta) = \begin{pmatrix} \cos\theta & r\sin\theta & r(1-\cos\theta) \\ -r^{-1}\sin\theta & \cos\theta & \sin\theta \\ 0 & 0 & 1 \end{pmatrix} \quad S_v(\theta) = \begin{pmatrix} 1 & r\theta \\ 0 & 1 \end{pmatrix} \tag{3.5}$$

By cascading these matrices the transformation of a ray starting at the plasma and propagating through the magnet to a detector can be easily represented:

$$\mathbf{h} = D_h(i)S_h(\theta)D_h(o)\mathbf{h}_0 \tag{3.6}$$

$$\mathbf{v} = D_v(i)S_v(\theta)D_v(o)\mathbf{v}_0 \tag{3.7}$$

Here, the subscript "0" indicates the state of the ray at the source, o is the distance from the plasma to the entrance of the magnet, and i is the distance from the exit of the magnet to the detector.

Vertical Focusing and the Fringing Field

The effects of the magnet's fringing field are significant and cannot be neglected. In the first place, the physical extent of the field region is invariably larger than the physical extent of the pole pieces. If the gap width between the two pole pieces is g, then the fringing field can be accounted for by replacing the radius R with the "effective radius" $R_{\text{eff}} = R + 0.62g$ in all equations.

The fringing field also has the potential for vertical focusing. When a beam enters a sector magnet at an angle of incidence α, the transfer matrices must be multiplied by the following thin lens matrices:

$$L_h(\alpha) = \begin{pmatrix} 1 & 0 & 0 \\ \tan\alpha/r & 1 & 0 \\ 0 & 0 & 1 \end{pmatrix} \quad L_v(\alpha) = \begin{pmatrix} 1 & 0 \\ -\tan(\alpha-\psi)/r & 1 \end{pmatrix} \tag{3.8}$$

The angle ψ is an extended fringing field correction given by [15]

$$\psi = K_1 \frac{g}{r}\left[\frac{1+\sin^2\alpha}{\cos\alpha}\right]\left[1 - K_1 K_2 \frac{g}{r}\tan\alpha\right] \tag{3.9}$$

where K_1 and K_2 are constants normally taking the values 0.45 and 2.8 respectively. The matrices for the whole system are then

$$\mathcal{H} = D_h(i)L_h(\alpha_2)S_h(\theta)L_h(\alpha_1)D_h(o) \tag{3.10}$$

$$\mathcal{V} = D_v(i)L_v(\alpha_2)S_v(\theta)L_v(\alpha_1)D_v(o) \tag{3.11}$$

where α_1 is the entrance angle relative to the pole face normal and α_2 is the exit angle relative to the pole face normal.

Imaging and Focusing

In order for the Browne and Buechner magnet to function as a true spectrometer it is important that an image point be found for each energy. That is, assuming the rays originate from a point source, all rays of the same energy must converge at some point unique to that energy. This will be the case if the matrix element $\mathcal{H}_{12}$ vanishes for some value of i. Solving the equation $\mathcal{H}_{12} = 0$ for i results in

$$i = \frac{(1 + \tan\theta \tan\alpha)o + r\tan\theta}{(\tan\theta - \tan\alpha)o/r - 1} \tag{3.12}$$

where α is the angle of incidence. The exit angle with respect to the pole face normal is taken to be zero, as was the case in the experiment.

Vertically, imaging is not important since the ray energy does not correlate with the vertical direction.

Dispersion and Resolving Power

The advantage of the Browne and Buechner design is its ability to resolve a broad range of energies. The resolving power of the magnet in combination with some detector is defined as the inverse of the relative momentum spread incident on the detector. To determine this quantity, consider the horizontal position of a ray at the detector:

$$x = \mathcal{H}_{11}x + \mathcal{H}_{12}x' + \mathcal{H}_{13}\delta \tag{3.13}$$

Assuming the detector is at an image point, and assuming the source is very small, this reduces to

$$x = D\Delta p/p \tag{3.14}$$

where $D = \mathcal{H}_{13}$ has been defined as the dispersion. Replacing x by the size of the detector aperture gives the resolving power:

$$\text{R.P.} = \frac{D}{\Delta x} \tag{3.15}$$

Solving for the matrix element $\mathcal{H}_{13}$ gives

$$D = r(1 - \cos\theta) + i\sin\theta \tag{3.16}$$

This equation can be misleading in that if the image distance i becomes large, a high resolving power might be indicated even for small angles. In practice, however, there are experimental constraints limiting the distance between the detectors and the magnet.

3.1.2 Electron Spectrometer Design

Figure 3.3 shows a mechanical drawing of the actual pole pieces used in the experiment. As shown, only the part of the circle that will actually be used to bend the particles is kept. This minimizes the electrical power needed to produce a given magnetic field. Also, the entrance side of the pole pieces are cut flat so that by rotating the pole pieces vertical focusing can be achieved while not disturbing the basic Browne and Buechner geometry.

The pole pieces are energized using an electromagnet with a "C" shaped iron yoke. The magnetic field was measured *in situ* as a function of current. The

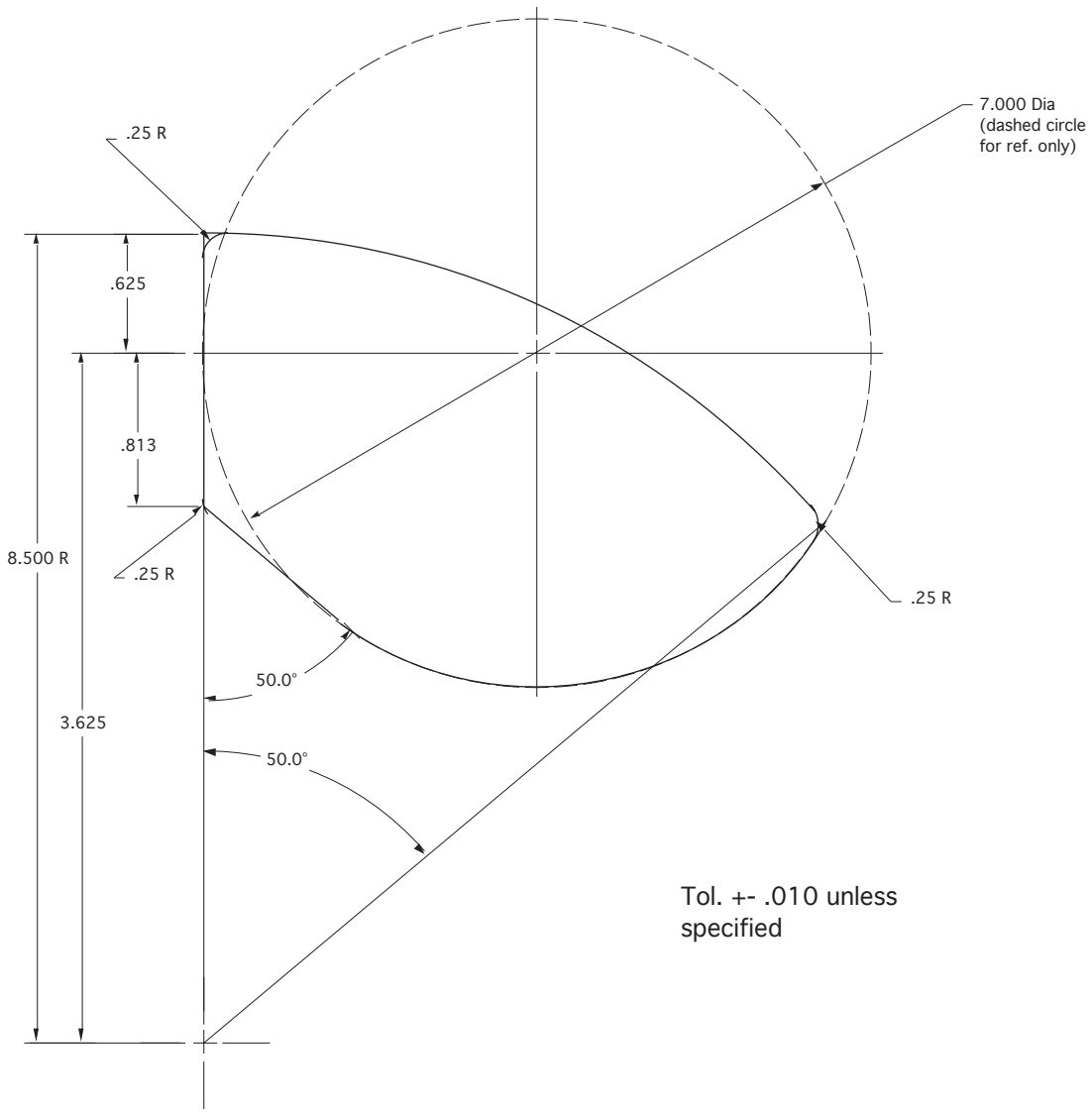

Figure 3.3: Mechanical Drawing of the Pole Pieces

results are shown in figure 3.4 for a 1 cm gap width. The curve drawn through the data points is a sixth order polynomial fit with coefficients

$$C_i = \{0.08, 0.92, 0.10, -0.013, 5.3 \times 10^{-4}, -10^{-5}, 7.2 \times 10^{-8}\} \tag{3.17}$$

At the highest field shown, the energy corresponding to an exit angle of 60° is about 100 MeV. As will be shown below, exit angles less than 60° lead to impractical image distances.

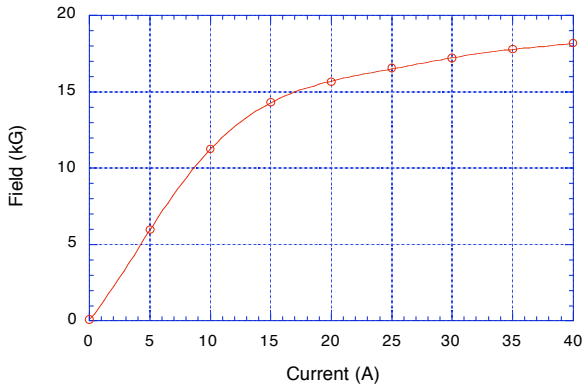

Figure 3.4: Magnetic Field with 1 cm Gap

The optical properties of the magnet can be checked against theory in two ways. First, the actual fringing field of the magnet can be compared with the curve used in deriving the theory. A measurement of the fringing field is shown in figure 3.5. The shape is extremely close to the one commonly used in deriving the ray matrices for a sector magnet [14]. Another more direct test was performed at UCLA, where a well characterized source of 2 MeV electrons was available. Using fluorescent screens and CCD cameras, the images formed by the magnet were found to be in excellent agreement with the predictions of ray tracing.

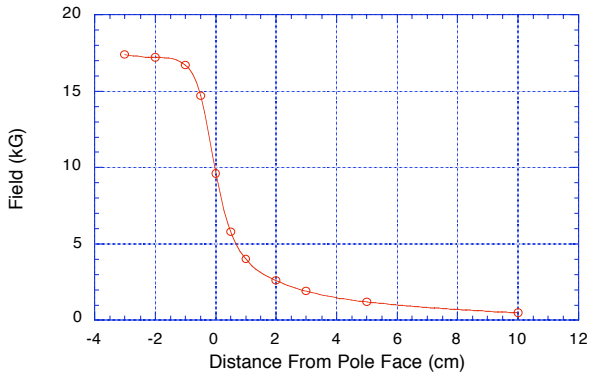

Figure 3.5: Fringing Field with 1 cm Gap

Finally, we consider the imaging properties of the particular pole pieces shown in figure 3.3 given their position relative to the source in the actual experiment. In the experiment, the pole pieces were positioned approximately one meter from the source. The rotation angle was 10°. A lead collimator was used to limit the angular acceptance of the magnet to about f/60.

Figure 3.6 shows two graphs. The first shows the resolving power as a function of angle. The fact that the resolving power is high for a wide range of angles is what makes the Browne and Buechner design attractive. The second plot shows the image distance as a function of angle. We see that the image distance becomes impractical for angles less than about 60°. Shown in figure 3.7 is a polar plot of the image distance. We see that the locus of all image points lies on a straight line. This line defines the "image plane" of the spectrometer.

Vertical focusing was not of critical importance in the experiment since the acceptance cone of the magnet was not much larger than the acceptance cone of

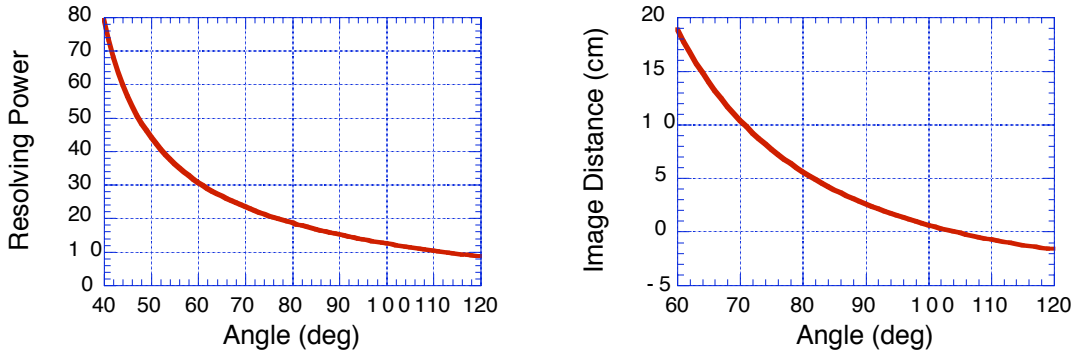

Figure 3.6: Image distance and resolving power for a 1 cm gap. The image distance is the distance from the exit pole face to the image point.

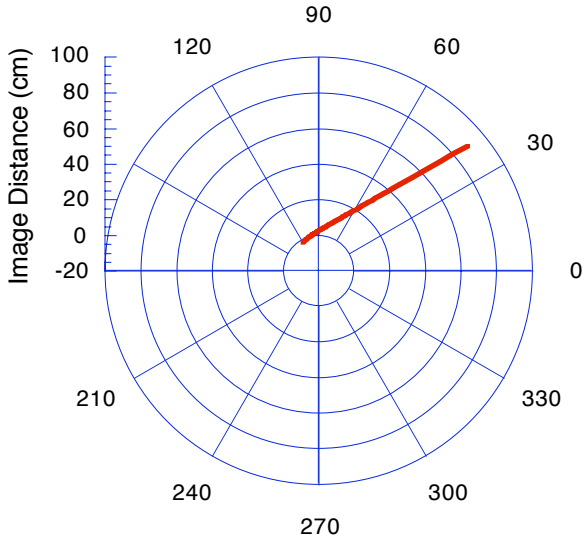

Figure 3.7: Image distance for a 1 cm gap on a polar plot, showing that the surface containing the image of every energy is a plane.

the detectors. In addition, it is expected that the highest energy particles will enter the magnet nearly on-axis. Nevertheless, a modest 10° pole face rotation was applied in order to nearly collimate most of the trajectories. Figure 3.8 shows a plot of the ratio of $y'_{\rm out}/y'_{\rm in}$ as a function of exit angle.

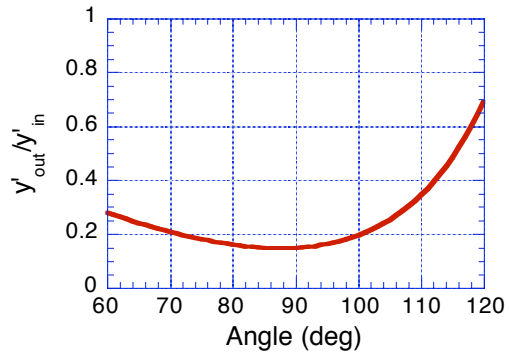

Figure 3.8: Vertical Focusing for a 1 cm gap and pole face rotation of 10°

3.1.3 Detection Apparatus

The detection apparatus consists of the magnet, a vacuum box, and several silicon surface-barrier detectors (SSBD) placed in the image plane of the magnet. Also, on some shots fluorescent screens and film were used to count electrons. Figure 3.9 shows a scale picture of the vacuum box and pole pieces.

The vacuum box is needed only when the electron energy is so low that angular

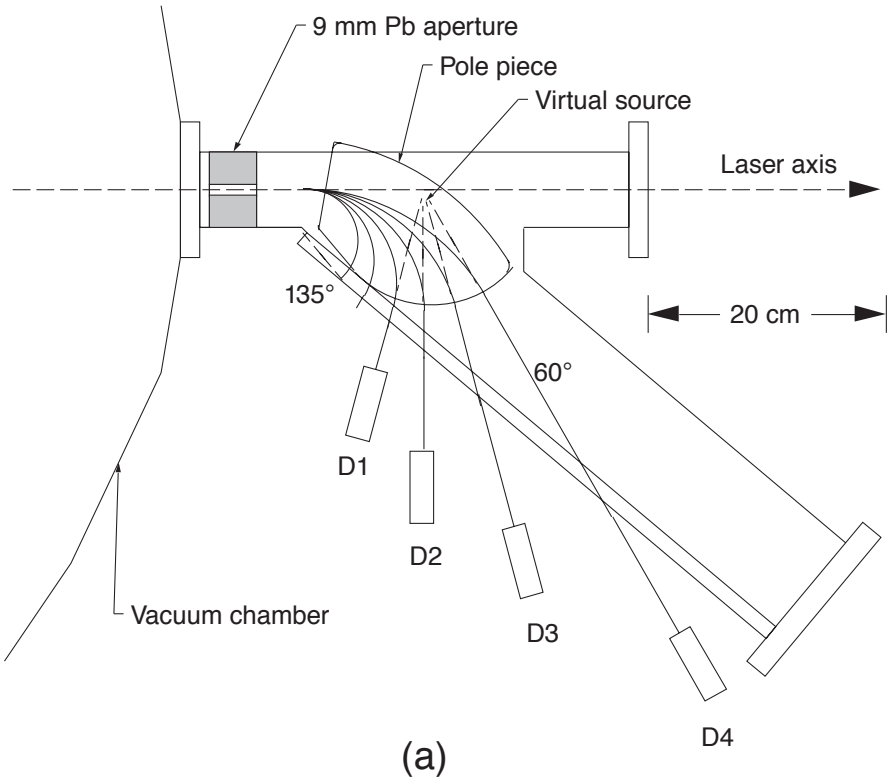

Figure 3.9: Detection apparatus. The pole pieces are brought into contact with the vacuum box from the outside, which results in a gap width of 2 cm. The exit window of the magnet is composed of O(100) μm thick mylar, and lies approximately in the image plane of the magnet.

scattering in the air would affect the resolving power of the magnet. The root-mean-square (rms) scattering angle for electrons can be determined from[1] [16]

$$\langle\theta\rangle_{\text{rms}} = \frac{21MeV}{p\beta}\sqrt{\frac{\rho z}{X}} \tag{3.18}$$

where ρ is the mass density of the material, p is the particle momentum in MeV/c, X is the radiation length of the material, and z is the thickness of the material. In air, this becomes

$$\langle\theta\rangle_{\text{rms}} = \frac{0.16}{p\beta}\sqrt{z} \tag{3.19}$$

where p is again in MeV/c and z is in centimeters. The maximum tolerable scattering angle occurs when the spot size of initially on-axis electrons reaches the size of the detector aperture at the detector. That is,

$$\theta_m = \frac{\Delta x}{\sqrt{z}} = 0.08 \tag{3.20}$$

Here, Δx is the aperture size and z is the pathlength in air, which was taken to be 100 cm. This implies that for energies above 20 MeV, the vacuum box is not needed.

Surface Barrier Detectors

An SSBD is essentially an n-type silicon substrate with a layer of oxidation and two metal contacts. The oxidation layer forms a "surface barrier" which causes the device to behave like a diode. When the SSBD is reverse biased, a depletion region forms adjacent to the silicon-oxide junction. When radiation passes

[1] In this equation, β is to be regarded as having units of velocity despite being a normalized quantity.

through the depletion region, electron-hole pairs are created through ionization. These free charges are accelerated by the electric field in the depletion region and are subsequently collected at the electrodes. If each radiation particle creates the same amount of free charge in the detector, then the detector produces a current proportional to the number of particles incident upon the detector. For beta rays in silicon with $\gamma > 3$, this is indeed the case since the ionization cross section is then roughly independent of energy. Also, the range in silicon of such energetic beta rays easily exceeds the 1 mm thickness of the detectors used in our experiment.

Since the SSBD's are sensitive to any type of radiation, measures must be taken to insure that the radiation of interest dominates the signal. The detectors were therefore inserted into open ended lead containers with a copper filter facing the virtual electron source in the center of the magnet. This arrangement is depicted in figure 3.10. The thickness of the copper was chosen to be as great as possible given a maximum acceptable scattering angle of 10° for beta rays with the expected energy. This thickness can be calculated using equation 3.18. For copper, this becomes

$$z[\text{cm}] = 2 \times 10^{-4} p^2 \tag{3.21}$$

The lead shielding varied during the course of the experiment. The thickness of the lead varied between 3 and 6 mm.

Once the charge Q is generated in the SSBD, it must be converted into a signal readable by a scope. A simple solution is to collect the charge, Q, on a capacitor, C, and read out the voltage $V = Q/C$ on the scope. The circuit used in the experiment is shown in figure 3.11. The charge sensitive preamp collects

Figure 3.10: SSBD shielding. The electron source is on the right.

the charges generated in the SSBD onto a capacitor with value

$$C = C_{\text{in}} + C_{\text{cable}} \tag{3.22}$$

where C_{in} is the input capacitance of the preamp and C_{cable} is the capacitance of the coaxial cable used to transmit the signal. The voltage on the capacitor is held for a period of time R_2C_1 which is chosen to be much longer than the duration of the electromagnetic pulse (EMP) generated by the laser plasma interaction. This allows the desired signal to be easily separated from the EMP noise which invariably appears on the scope.

Fluorescer/Film Detector

When the electron flux was high enough, film was used to obtain spatial images of the electrons in the image plane of the magnet. This corresponds to obtaining a continuous spectrum. The film was sandwiched between two fluorescent screens which were in turn placed into a black plastic cassette sealed with black tape.

The film was 35 mm Ilford HP5 Plus, ISO 400 and the fluorescer was 3M "Trimax". The film was developed for 5 minutes in D19 developer.

The thickness of the black cassette was 0.5 mm, which is sufficient to absorb

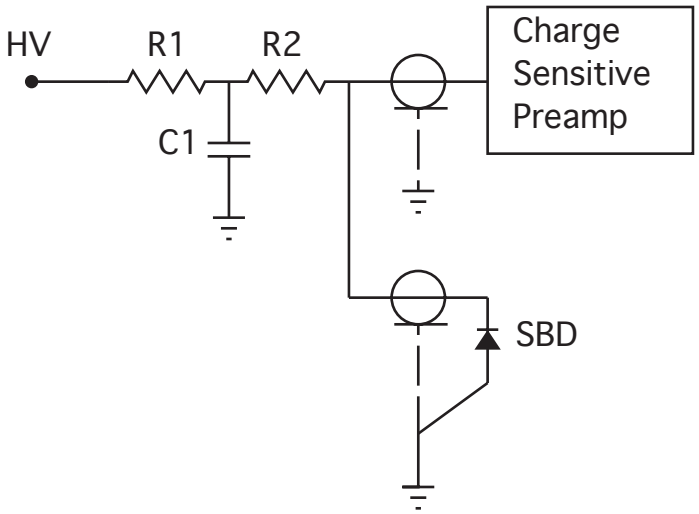

Figure 3.11: Detection Circuit. The SSBD is reverse biased through two large resistors R1 and R2. The current generated by incident radiation is collected by the input capacitance of the charge sensitive preamp. The charge sensitive preamp was either EG&G model 113 or 142A. High voltage was supplied by a NIM module.

stray light generated by the experiment, but also thin enough to transmit electrons in the energy range of interest (10-30 MeV). Thus, it was possible to obtain simultaneous data using both the fluorescer and the SSBD's.

Dynamic Range of the Detection System

In this experiment, to count electrons over a broad range of energies required several orders of magnitude of dynamic range due to the fact that the electron spectrum was exponentially decaying. The dynamic range of a particular SSBD in a particular electronic configuration is at best two orders of magnitude. The dynamic range of a set of differing SSBD's in different electronic configurations can be much higher. First of all, the detector thickness, which is directly proportional to sensitivity, can be varied over one order of magnitude. Second, the preamplifier input capacitance can be varied. The preamp model 113 includes a dial on the front panel for this purpose. After the cable capacitance is included, this allows for an additional order of magnitude of dynamic range. Finally, the bias voltage can be varied. The bias voltage controls the thickness of the depletion region, which in effect is the thickness of the detector. However, the waveform associated with a partially depleted detector is not ideal. During these experiments, therefore, the bias voltage was always set to its maximum value.

The dynamic range of the fluorescer/film combination is large due to the fact that neutral-density (ND) filters can be placed between the fluorescer and the film. The maximum sensitivity, however, is not as great as that of the SSBD's.

Stray Particles

A problem which is sometimes raised is that if the vacuum box is not in place, it might be possible for low energy particles to find their way into any given detector by performing a random walk from the vacuum chamber to the detector. Such particles could diffuse their way either across or around the magnetic field. We show here that this eventuality is extremely unlikely.

First, we estimate the number of electrons in the entire plasma. If the radius of the plasma cylinder is equal to the spot size of the laser (20 μm), and the length of the cylinder is equal to the length of the gas jet, then for a 10^{19} cm^{-3} plasma there are 10^{14} electrons.

Next, we estimate the probability that a 100 keV electron placed at the window of the vacuum chamber will be detected by an SSBD. The mean free path of a 100 keV electron in air is about 10 cm, while the range (distance travelled before absorption) is about 100 cm. Since the high energy SSBD's are about 100 cm from the window, the probability of a particle passing through a given SSBD is the ratio of the SSBD volume to the volume of a sphere with radius 100 cm. This comes to about 5×10^{-8}. However, even if a particle enters the SSBD volume it still must penetrate the lead shielding and the copper filter. The range of a 100 keV electron in copper is at most 50 μm. The thinnest filter ever used on the high energy channels was 1 mm. The probability of penetrating the copper is therefore about 10^{-9}. Since the probability of penetrating the lead is even more remote, the total probability for detection is about 10^{-18}.

Now, suppose every plasma electron was placed at the window of the vacuum chamber and given 100 keV. Assuming a neutralizing charge was somewhere

nearby, the number of electrons detected by a given SSBD would be at most $10^{14} \times 10^{-18} = 10^{-4}$. In other words, one would have to wait about 10,000 shots before even a single spurious electron could find its way to an SSBD. In reality, of course, the situation is even better since only a small fraction of the plasma electrons ever even escape the vacuum chamber.

3.1.4 Detector Characterization

SSBD Calibration

It is possible to obtain reasonable estimates of the charge generated in an SSBD using a simple theoretical model, but we choose instead to simply calibrate each detector using a known radiation source. The calibration attempts to determine the voltage generated on a scope for each electron incident on a particular detector given various electronic configurations such as the one shown in figure 3.11.

The radiation source used for the calibration was the 2 MeV electron linac at UCLA with the temperature of the filament in the gun turned down. Normally, this would be far from an ideal source for calibration purposes because of tuning drifts due to thermal fluctuations in the size of the RF cavity. An online method was therefore needed to measure the very small electron flux incident on the detector each shot. This was accomplished using a fluorescer/CCD camera combination. The setup is illustrated in figure 3.12. As indicated in the figure, a fluorescent screen with a hole the size of the detector aperture is placed in front of the SSBD. When the linac is fired, a simultaneous measurement of counts on the CCD camera and SSBD signal can be made. If the sensitivity of the fluorescer in terms of counts per electron is known, and if the electron spot size is much

greater than the size of the hole, then the number of electrons incident on the detector can be determined from the pixel values near the hole.

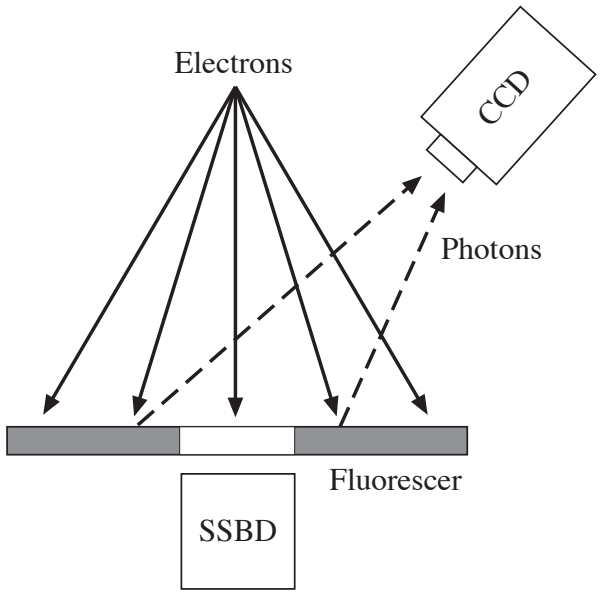

Figure 3.12: Schematic of the setup used to calibrate SSBD's. The 12-bit CCD camera was thermoelectrically cooled and could easily resolve photon signals due to electron fluences as low as 10^3 particles per mm^2.

The sensitivity of the fluorescer was determined using a current monitor—essentially, a magnetic pickup loop. The current monitor can only measure currents which are much too large for the SSBD's. The fluorescer bridges the gap between the two sensitivities with nearly unlimited dynamic range following from the fact that ND filters can be placed in front of the camera. Using the current monitor, the maximum current deliverable by the linac was measured to be about 30 mA. Streak images of Cherenkov emission pinpointed the electron pulse-length to be about 1.5 ns. The maximum charge deliverable by the linac is therefore about 50 pC. By associating this number with the maximum number

of counts measured on the CCD camera, counts per electron was determined for the particular optical setup used during the calibration measurements.

Fluorescer/Film Calibration

The nonlinearity of film makes converting the film images into quantitative data nontrivial. The density at each point on the film was determined by taping the film up to a lightbox and reading the image onto a computer using a CCD camera. The density was converted to exposure using a calibrated density step-wedge.

3.2 Optical Diagnostics

Optical diagnostics provide an independent measure of various plasma wave characteristis. Figure 3.13 shows the k-matching geometry for the Thomson scattering diagnostic. In the actual experiment, a 1 cm diameter .53 μm probe beam containing about 5 mJ of energy in a 20 ps long pulse was propagated into the plasma at an angle of 104° with respect to the infra-red pump beam. Generally, a probe beam scattering off longitudinal modes in a plasma acquires a frequency shift such that

$$\omega_s = \omega_g + \omega_p \tag{3.23}$$

where ω_g is the frequency of the incident probe beam, ω_p is the plasma frequency, and ω_s is the frequency of the scattered wave. The probe beam will scatter most strongly in the direction given by the k-matching condition

$$\mathbf{k}_s = \mathbf{k}_g + \mathbf{k}_p \tag{3.24}$$

Since the plasma is rare, the electromagnetic waves will propagate at about the speed of light ($c = 1$):

$$|\mathbf{k}_s| = \omega_s \tag{3.25}$$

$$|\mathbf{k}_g| = \omega_g \tag{3.26}$$

Combining the above equations leads to

$$k_x^2 + k_y^2 + 2\omega_0(k_x \sin\theta + k_y \cos\theta) = 2\omega_0\omega_p + \omega_p^2 \tag{3.27}$$

where k_x and k_y are respectively the axial and transverse components of $\mathbf{k}_p$, and θ is the angle of incidence of the probe beam with respect to the x-axis. In a laser accelerator experiment, it is expected that the largest amplitude modes in the plasma will have $k_x \approx \omega_p$. Supposing further that the angle of incidence is zero, one obtains

$$k_y = -\omega_0 + \omega_0\sqrt{1 + 2\frac{\omega_p}{\omega_0}} \tag{3.28}$$

and for the angle between $\mathbf{k}_s$ and $\mathbf{k}_g$

$$\phi = \cos^{-1}\left(\frac{\omega_0 + k_y}{\sqrt{\omega_p^2 + (\omega_0 + k_y)^2}}\right) \tag{3.29}$$

This comes to about 3.5° for a plasma density of 1.5×10^{19}.

A subtlety in the Thomson scattering geometry emerges when one considers the fact that normally $\omega_p/\omega_0 \ll 1$. In this case, a binomial expansion leads to

$$k_y = \omega_p = k_x \tag{3.30}$$

Thus, we arrive at the often misleading result that the scattered light is generated by modes propagating at a 45° angle with respect to the main laser axis with phase velocity $c/\sqrt{2}$. There is nothing false about this conclusion, but it is also true that

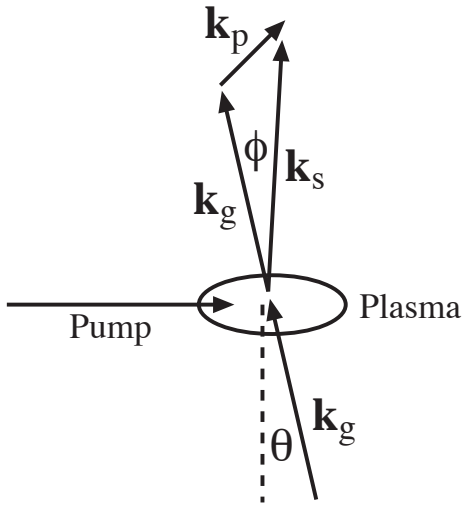

Figure 3.13: Thomson scattering geometry. The x-direction is left-right while the y-direction is up-down.

any real plasma wave will have a *continuous spectrum* of wavenumbers *in every dimension*. The presence of the component $k_y = \omega_p$ is simply a reflection of the fact that the plasma wave has a finite radial extent. Indeed, in the experiments reported here the laser spot size was on the order of a plasma wavelength. It is expected therefore that the plasma waves driven in the experiment will contain significant energy in the region of k-space visible to the Thomson scattering diagnostic.

The usefulness of collective Thomson scattering follows from the fact that the scattered power can be related to the amplitude of the plasma wave [17, 18]. In these experiments, the goal of the Thomson scattering diagnostic was to determine for a given shot the plasma wave amplitude as a function of frequency and the axial coordinate, x. The setup used to achieve this is illustrated schematically in figure 3.14. A beam block absorbs the unscattered probe light, while a

single lens is used to focus the scattered light and thus image the plasma wave amplitude onto the slit of a spectrometer. The spectrometer preserves the spatial image in the x-direction while dispersing energies in the y-direction. At the output plane, a map of $P(x, \lambda)$ appears, where P is the time integrated scattered power. The scattered power is proportional to ϵ^2. The gated image intensifier is useful both for increasing the raw signal and for eliminating long time-scale stray light.

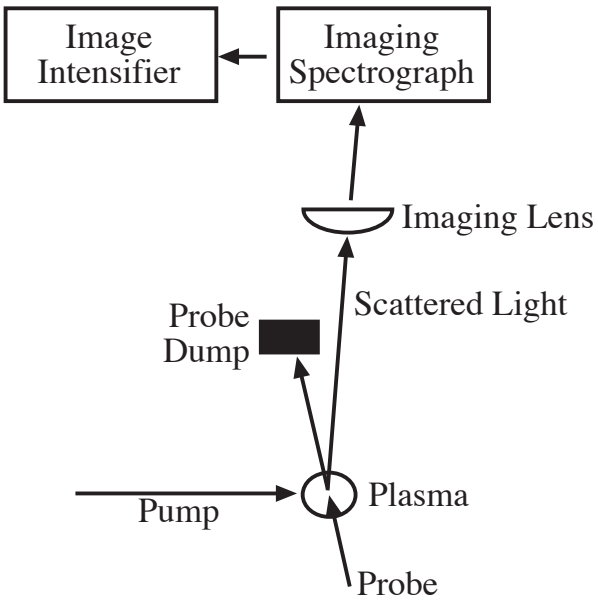

Figure 3.14: Thomson scattering setup. An image of the scattered light is formed on the input slit of the spectrometer. The frequency resolved image is transmitted to a one ns gated image intensifier. The intensified image was captured by a CCD camera and read into a computer. The spatial resolution along the slit was ≈ 150 μm while the spectral resolution was ≈ 64 $\mathring{A}$.

Chapter 4

Experimental Results and Analysis

The results reported here span three visits to RAL by the UCLA group and include contributions from numerous workers. The reader is referred to the papers generated by this body of work [19, 20, 21, 22, 23, 24, and others].

4.1 Preamble on Simulations

Before proceeding to the actual experimental results, we describe a computer simulation which will be constantly employed as an aid in understanding the data. The code is called PEGASUS [25]. It is a fully explicit, electromagnetic, relativistic particle-in-cell (PIC) code which uses a 2D cartesian grid set in motion at the speed of light. In the simulations discussed here, we typically have a 1 μm, 600 fs (FWHM) diffraction limited pulse with a peak vacuum intensity of 5×10^{18} W/cm^2 and a 20 μm diameter spot size. This pulse is propagated through a 1-2 mm slab of 1-3 $\times$ 10^{19} cm^{-3} plasma. The plasma begins at $x = 0$. The ions are modeled as a fixed uniform neutralizing background.

4.2 Forward Scattering Data

Two forward scattered spectra are shown in figure 4.1. The figure illustrates the typical result that at higher densities ($> 10^{19}$ cm^{-3}), each spectral feature broadens considerably [19]. This is a signature of wavebreaking since the broadening can be associated with the loss of coherenence of the plasma wave. In addition, the number of high energy electrons (> 10 MeV) detected increased dramatically as the density was raised above 10^{19} cm^{-3}. This also indicates wavebreaking, which is defined as the point where the main body of the electron distribution function is self-trapped.

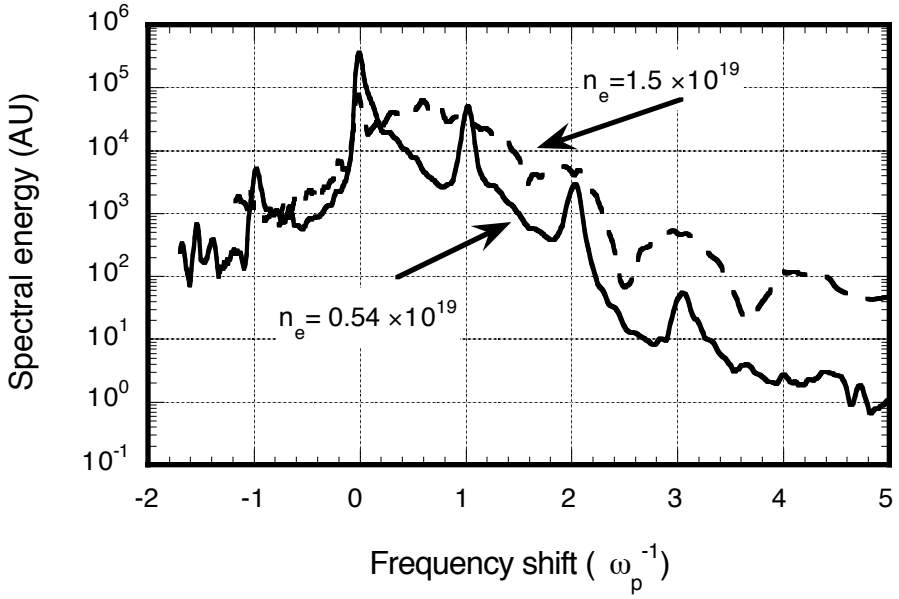

Figure 4.1: Spectrum of the transmitted laser light at two pressures. The frequency scale is normalized to ω_p so the sideband frequencies have integer values for both densities.

4.3 Electron Data

When wavebreaking occurs, it is expected that large numbers of plasma electrons will be trapped and accelerated to highly relativistic energies. Electrons with sufficient energy will escape the plasma in the form an electron beam which can be detected and energy-analyzed using the methods discussed previously.

4.3.1 Electron Shadows

In an environment where radiation of all kinds is present, the first step is to conclusively demonstrate that the type of radiation one seeks can be separated from the type one does not seek. At RAL, it was conclusively shown that a beam of charged particles indeed emerges from the plasma in the forward direction. The possibility that the signal was due to photons was decisively excluded.

As discussed previously, electrons propagating through the electron spectrometer in the expected way appear to emanate from a virtual source at the center of the circular pole pieces. If this is so, then opaque objects placed in the spectrometer's output plane should cast shadows which lie on a line drawn through the virtual source and the object. This proposition was tested using chunks of lead as the opaque objects and the fluorescer/film detector described previously to observe the shadows. The results are shown in figure 4.2. The shadow positions were found to be consistent with a highly localized radiation source at the center of the spectrometer. Only high energy charged particles emerging from the plasma could lead to the presence of this source.

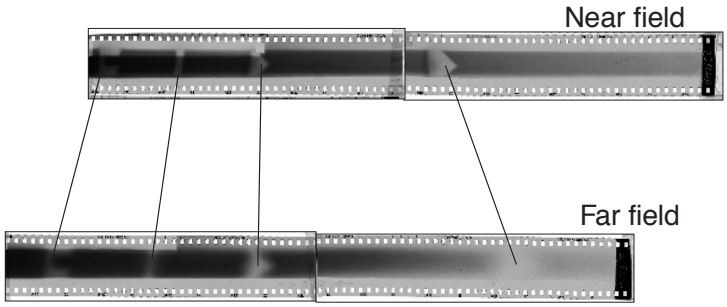

Figure 4.2: Two images of accelerated electrons taken on two similar laser shots with the film / fluorescer cassette located in two different planes: Near field, against the exit flange of the spectrometer; and Far field, 5 cm away fromand parallel tothe exit flange. Four lead objects were placed against the vacuum window, about 1 cm in front of the near field position. The measurement shows the directional nature of the electrons and the fact that they appear to emanate from a "virtual source."

4.3.2 Electron Spectra

At low energies (10-30 MeV), the electron flux is sufficient to use the fluorescer/film detector in conjunction with the SSBD's. The results from such a measurement are shown in figure 4.3. The vertical axis of the plot displays electrons per MeV, which is calculated using the formula

$$\frac{\text{electrons}}{\text{MeV}} = \frac{VD}{\eta E \Delta x} \tag{4.1}$$

where V is the raw signal (mV), D is the dispersion of the magnet (cm), η is the detector sensitivity (electrons per mV), E is the electron energy (MeV), and Δx is the size of the detector aperture (cm). The SSBD sensitivity and film exposure were determined as described previously. The absolute sensitivity of the film is not known, so the curve was scaled to match the SSBD data. The relative

agreement between the two detectors, however, is not arbitrary and appears to be satisfactory.

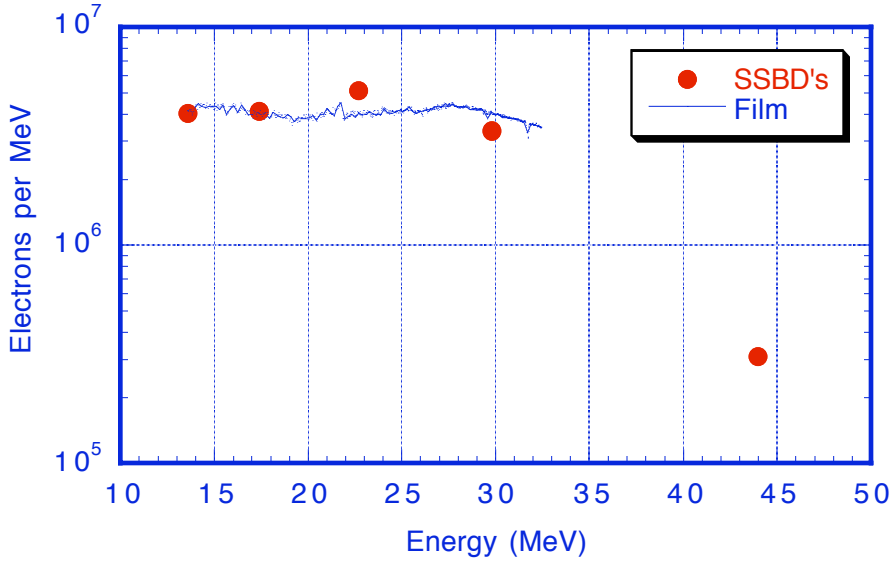

Figure 4.3: Electron spectra obtained by the SSBD detectors (points) and by the fluorescer/film detector (curve) for the same shot. The film data was scaled vertically only to overlap the SSBD data.

The data shown in figure 4.3 is typical of all electron spectra taken in the same energy range. The predominant feature is a "knee" in the spectrum at around 30 MeV where the spectrum changes from being constant to being exponentially decaying. Simulation results suggest that this feature is due mainly to the finite collection angle of the spectrometer. This is illustrated in figure 4.4 which shows a PEGASUS calculation of the correlation between propagation angle and kinetic energy after 1 mm of propagation. The propagation angle is defined as

$$\theta = \frac{\sqrt{p_y^2 + p_z^2}}{p_x} \tag{4.2}$$

where x is the axial coordinate. Evidently, the increased collection efficiency at higher energies makes up for the lack of particles up until 30 or 40 MeV. Beyond that point, the propagation angle is not a strong function of energy, so the experimental spectrum begins to drop off as expected.

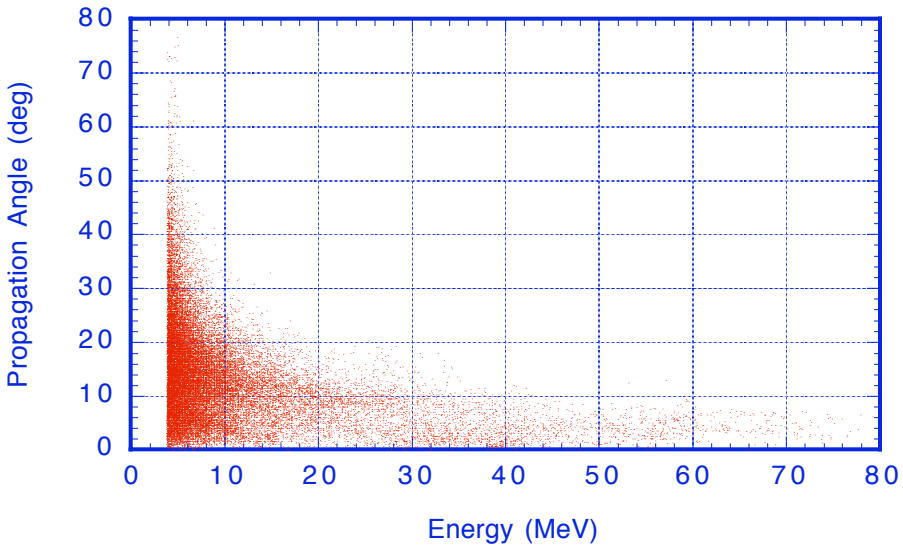

Figure 4.4: Electron hits in the plane of energy and off-axis-angle for electrons above 4 MeV as computed by PEGASUS. The data was taken after the laser had propagated 1 mm into the plasma. The experiment excluded particles outside a 1° full angle cone.

A more direct illustration of the effect of the finite collection angle is shown in figure 4.5. Here the simulated spectrum is shown for both full collection (f/0) and for a collection cone similar to the one used in the experiment (f/50). We see that even for the highest energies, a collection angle of f/50 greatly reduces the number of particles available for detection. Also plotted in figure 4.5 are two experimental spectra. The data is plotted in terms of "superparticles" per MeV.

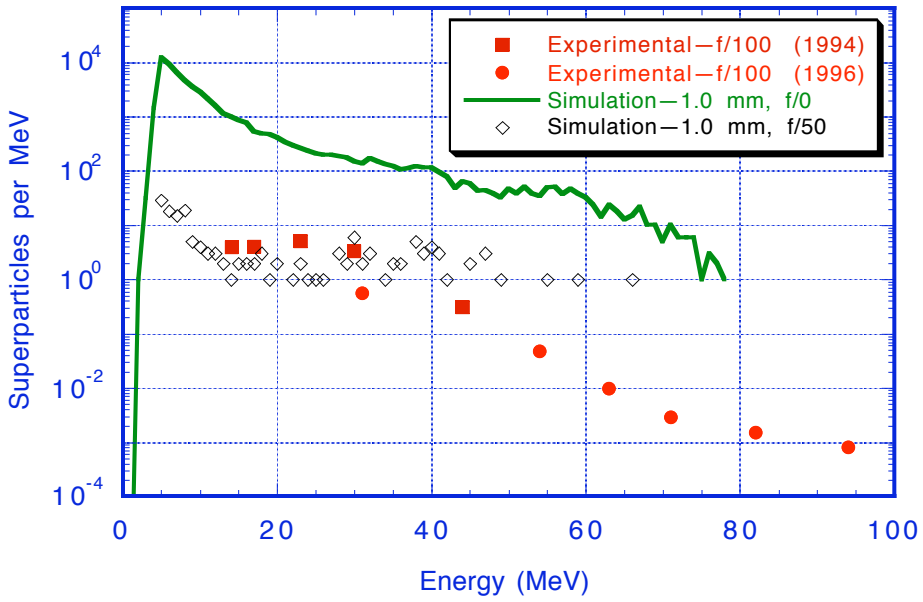

Figure 4.5: Comparison of experimental and simulated electron spectra. The experimental data is taken from two distinct laser shots so that a broad spectrum can be shown. The line is the simulated spectrum of all particles regardless of trajectory—i.e., in an f/0 focal cone. A superparticle is a simulation quantum equivalent to 10^6 electrons.

A "superparticle" is a simulation quantum which in this case carries the charge of 10^6 electrons. Since the simulation can only measure integral numbers of superparticles, the simulation data becomes noisy when the number of superparticles approaches unity. When the number of superparticles is much less than unity, the simulation data should become intermittent. Taking these facts into account the agreement between simulation and experiment shown in figure 4.5 is quite striking.

Three of the highest energy spectra obtained in these experiments are shown in figure 4.6. Each spectrum was taken at a different backing pressure. The effective electron density ($n_{\text{eff}} = n/\gamma$, where γ is the relativistic Lorentz factor of an electron quivering in the laser field) as a function of backing pressure was experimentally determined to be

$$n_{\text{eff}} \approx (p - 7) \times 10^{18} \tag{4.3}$$

where p is the backing pressure in bars and n_{eff} is given in units of cm^{-3}. This relation was obtained by measuring the frequency shift in the forward scattered spectrum and equating it to the relativistic plasma frequency. The same result was also obtained by observing the frequency shift in the Thomson scattered probe beam. Using this relation, we see that the 21 bar spectrum corresponds to a density of 1.4×10^{19} cm^{-3} and the 27 bar spectrum corresponds to a density of 2×10^{19} cm^{-3}. As will be discussed below, these numbers imply that electron energies well beyond the dephasing limit of linear theory were observed in this experiment.

To affirm the validity of the highest energy data, a discussion of noise is necessary. The signal to noise ratio associated with figure 4.6 varies from 100 for the

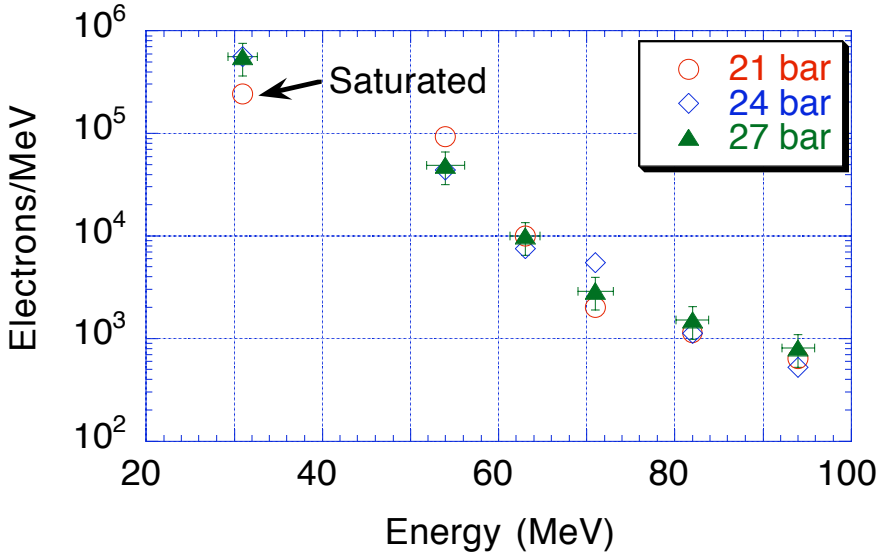

Figure 4.6: High energy electron spectra at three backing pressures. The horizontal error bars indicate the range of energies incident on each detector as well as taking into account possible positioning errors. The vertical error bars reflect the uncertainty in detector sensitivity. The signal to noise ratio is independent of this error.

lowest energy (31 MeV) to 2 or 3 for the highest energy (94 MeV). The noise is believed to be due to x-rays generated in the plasma, or x-rays generated by collisions between the electron beam and metallic hardware. The noise levels were determined by setting the magnetic field to zero during several shots and recording the apparent signal on each channel. The maximum such signal obtained for a given channel was then considered to be the noise level for that channel.

4.4 Plasma Wave Images

The laser power for a typical shot in these experiments (20 TW) exceeded the critical power for relativistic self focusing (P_c) by a factor of 20-24. High laser intensities could therefore persist over distances much greater than the Rayleigh length, $z_R = \pi w_0^2/\lambda$. Here, w_0 is the rms spot size of the laser beam at best focus and λ is the laser wavelength. By imaging the plasma waves excited by the laser, their amplitude and spatial extent can be determined. This allows an estimate of laser intensity vs. position to be made, which provides a quantitative measure of the effectiveness of the self-focusing process. In addition, such images can be used to determine the maximum energy gain for the self-trapped electrons. This number can then be compared with the measured electron spectrum for the same shot.

Figure 4.7 shows the Thomson scattering image for a shot on which anomalously high energy electrons (88 MeV) were observed, but which did not exhibit evidence of self-focusing. As shown in the figure, the wave amplitude exceeds one third its maximum value over 0.6 mm which is approximately one Rayleigh range. Evidently, self-focusing did not occur to a very great extent even though the laser

power was far above the critical power, $P_{\rm cr}$. It was found during the experiment that the length over which a plasma wave is excited depends critically on where in the gas the laser is focused. This may have to do with ionization induced refraction in the "corona" associated with an ambiguous gas-vacuum boundary.

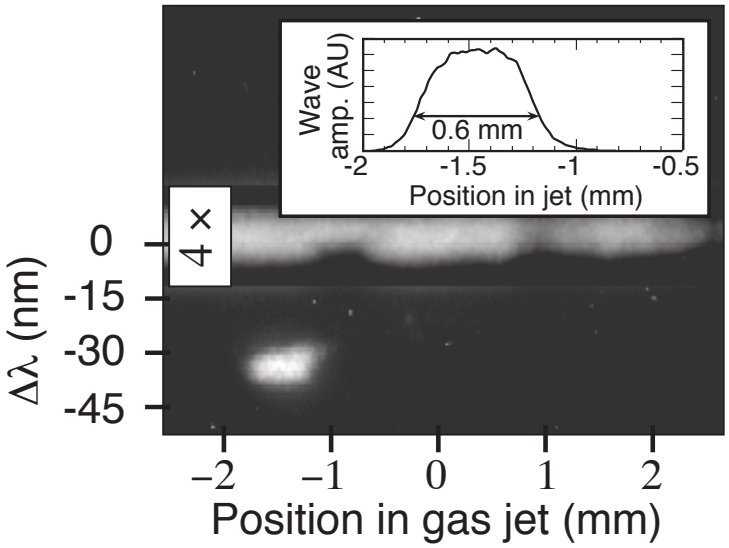

Figure 4.7: Thomson scattered spectrum vs. distance along the gas jet indicating the spatial extent of the relativistic plasma wave. Position zero is the center of the 4 mm diameter gas jet. The laser propagates from left to right and is focused at -2.0 mm. The stray light at $\Delta\lambda = 0$ has been attenuated by a factor of 4. The gas jet backing pressure was 21 bar and the laser energy on target was 23 J. Wave amplitude vs. position is shown in the inset.

Figure 4.7 can also be used to estimate the dephasing limit for this shot. The frequency shift implies an effective electron density of 1.4×10^{19} cm^{-3} which gives $\gamma_{ph} = 8.5$ and a dephasing distance of $L \approx 0.32$ mm. Also, the observed uniformity of the frequency shift indicates that within the 50 $\mathring{A}$ resolution of the detection system the plasma density is uniform throughout the length of the plasma wave. It is difficult to obtain an absolute estimate of the amplitude of

the plasma wave from the scattered power because of large uncertainties in estimating the transverse dimension and duration of the plasma wave. However, on some shots the second harmonic of the plasma wave is also seen in the Thomson scattered spectrum. Based on harmonic ratios [26], the amplitude of the waves observed on these shots can be determined and then related to the number of counts on the CCD. Using this measurement as a calibration, the peak amplitude of the wave from figure 4.7 can be shown to be between 20 and 60 percent. Using the most liberal estimate of the wave amplitude ($\epsilon = 0.6$), the dephasing limit comes to 55 MeV. On the other hand, integrating the amplitude of the accelerating electric field over the entire length of the plasma wave gives an energy gain of 120 MeV. This is the energy a particle would gain if somehow the dephasing process could be eliminated. As will be discussed below, the detection of 88 MeV electrons on this very shot indicates that to some extent this may indeed happen.

Figure 4.8 shows a plasma wave image where self-focusing is clearly in evidence. Here we see that plasma waves are excited throughout the entire length of the gas jet, which covers a distance of more than ten Rayleigh lengths. The frequency change in the central region is accounted for by the gas jet's inherent neutral density profile. The amplitude of the plasma wave at $z = 1.7$ mm is estimated using the methods described previously as 20-60%. The intensity needed to drive this plasma wave can be estimated using the 3D wake-field formulism [2]

$$\frac{n}{n_0} \approx \frac{a^2/2}{(1+a^2/2)^{1/2}} \left[1 + \frac{8}{k_p^2 w^2}\left(1 - \frac{2r^2}{w^2}\right)\right] \exp\left[\frac{-2r^2}{w^2}\right] \tag{4.4}$$

where a is the peak normalized vector potential associated with the laser, and w is the spot size. The normalized vector potential is related to the laser intensity

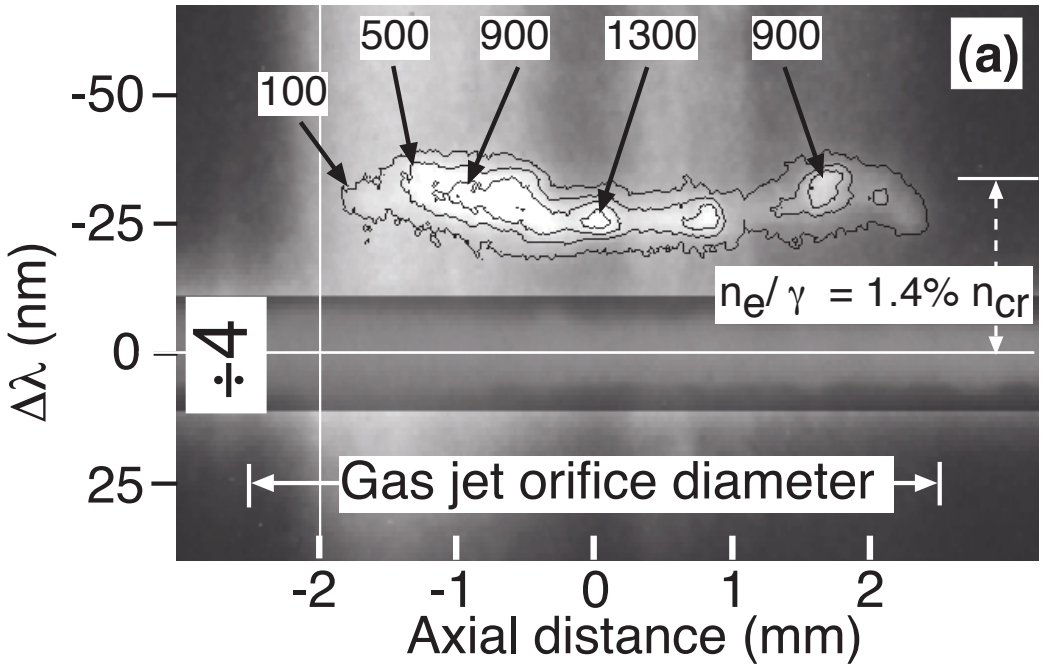

Figure 4.8: Thomson scattered spectrum vs. distance along the gas jet. The gas jet backing pressure was 20 bar and the laser energy on target was 24 J.

by

$$a \approx 8.6 \times 10^{-10} \lambda[\mu\text{m}] \sqrt{I[\text{W/cm}^2]} \tag{4.5}$$

Inserting this into the wake-field formulism gives a relationship between the intensity, spot size, and plasma wave amplitude. Evaluating this relationship on axis ($r = 0$), we plot the channeled intensity vs. the unknown spot size in figure 4.9 for a plasma wave amplitude of 50%. Also shown is the laser power required given a particular intensity and spot size. The laser power is most likely constrained to the range $1 < P < 20$ TW since 1 TW is the critical power for relativistic self-focusing and 20 TW is the incident power. Examining figure 4.9 reveals that the channeled intensity throughout this range exceeds 10^{18} W/cm^2, whereas the intensity after 12 Rayleigh lengths of vacuum propagation would have been less than 10^{16} W/cm^2.

The electron spectrum measured on the shot with self-focusing did not indicate that self-focusing is amenable to the production of high energy electrons. The shot associated with the short plasma wave of figure 4.7 produced more electrons at all energies than the shot associated with the long plasma wave of figure 4.8. Generally, there was no clear correlation between self-focusing and electron production. At high energies, this is not surprising since figure 4.8 indicates that the self-focusing process results in the production of several *distinct* plasma waves which cannot be expected to be coherent with respect to one another. At low energies, this may not be so important. Indeed, other workers [27] have observed a correlation between self-focusing and electron production in the energy range 1-2 MeV.

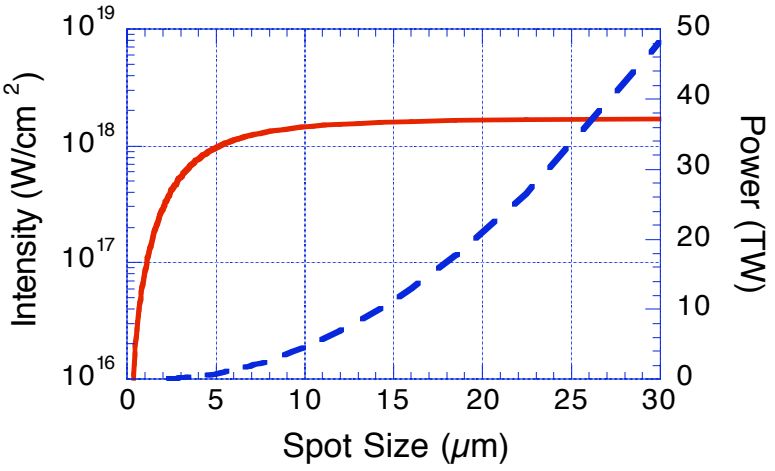

Figure 4.9: Channeled intensity after 12 Rayleigh lengths assuming a wake-field type driver and a plasma wave amplitude of 50%. The dashed line is the laser power implied by the given intensity and spot size, which is not likely to exceed the incident power of 20 TW.

4.5 Acceleration Beyond the Dephasing Limit

As mentioned above, the highest energy electrons observed in the experiment exceeded the dephasing limit of linear theory. According to the linear, but two dimensional, cold plasma theory, the maximum energy [1] of an electron trapped by the potential of a relativistic plasma wave having an amplitude $e\phi = \epsilon mc^2$ is given in the limit $\epsilon\gamma_{ph} > 1$ by

$$W \approx 2\gamma_{ph}(1 + \epsilon\gamma_{ph})mc^2 \tag{4.6}$$

where $\epsilon = \phi/\phi_{max} = n_1/n$ is the normalized potential or density perturbation associated with the wave and γ_{ph} is the Lorentz factor corresponding to the phase velocity v_{ph} of the wave. γ_{ph} is approximately ω/ω_p where ω is the laser frequency and ω_p is the plasma frequency. It is generally assumed that $v_{ph} = v_g$, where $v_g = c(1 - \omega_p^2/\omega^2)^{1/2}$ is the linear group velocity of light in the plasma. Here we have only considered acceleration of the electron while it is in the focusing phase of the radial electric field since test particle calculations in ideal plasma waves have shown that electrons injected into defocusing regions are deflected out of the wave as they are accelerated.[9] The dephasing distance is obtained by simply calculating the distance it takes a particle moving at c to move ahead of the wave moving at v_{ph}, by 1/4 of the plasma wavelength, $\lambda_p/4$. This gives a dephasing distance, $L = \pi\gamma_{ph}^2/k_p$ where $k_p = \omega_p/c$.

The above estimates for W and L are only valid for small ϵ and constant v_{ph} plasma waves. Indeed, self-consistent particle-in-cell (PIC) simulations of plasma beat wave and laser wake field accelerators [8] (where extremely coherent plasma

waves ($\epsilon < 0.5$) were excited) show that the externally injected particles gain energy principally in the focusing and accelerating phase of the wave and that the above linear scaling relationships are excellent predictors of both the dephasing length and the energy gained by the particles. However, for extremely nonlinear plasma waves there are many mechanisms including frequency shifts[28], relativistic effects[2, 29, 30], pulse shape and time evolution of the driver[25], incoherent plasma wave dynamics[31] and self-generated focusing fields[32] that can lead to energy gains greater or less than the linear dephasing limit.

The experimental spectra of figure 4.6 reveal that the linear dephasing limit can indeed be exceeded. Based on both Thomson scattering data and simulation results, the amplitude of the plasma wave during these shots was limited to about $\epsilon = 0.6$. Also given by Thomson scattering is the "effective density" as a function of the axial coordinate. The effective density is given by

$$n_{\text{eff}} = \frac{n}{\gamma} \tag{4.7}$$

where γ is the average Lorentz factor of the particles making up a fluid element. Figure 4.7 gives the typical result that the effective density is nearly constant throughout the length of the plasma wave. Based on this information, the dephasing length for the lowest pressure shot ($n/\gamma = 1.4 \times 10^{19}$ cm^{-3}) should have been $L \approx 0.32$ mm and the maximum energy should have been 55 MeV. Hence, the observed maximum energy of 94 MeV is nearly double the dephasing limit. Furthermore, for the highest density shot (2×10^{19} cm^{-3}) the spectrum extends beyond 74 MeV which is the energy an electron would have even if it were to survive the full $\lambda_p/2$ accelerating phase of the plasma wave. There are in essence two

possible explanations for the observed acceleration. First, variations in the amplitude or phasing of the plasma wave could exist if they occured on a spatial scale much smaller than the resolution of the Thomson scattering diagnostic, which is approximately 150 μm, or 10-20 plasma wavelengths. Second, the presence of the laser fields could modify the particle dynamics in some way which enhances energy gain. As will be discussed below, simulation results strongly suggest that local nonlinear modifications to the plasma wave phasing are responsible for the enhanced acceleration.

Once again, we call upon PEGASUS to clarify the experimental observations. The simulation propagates a 1 μm, 600 fs (FWHM) diffraction limited pulse with a peak vacuum intensity of 5×10^{18} W/cm^2 and a 20 μm diameter spot size through a 1 mm slab of 1.4×10^{19} cm^{-3} plasma. The plasma begins at x = 0 mm. The ions are modeled as a fixed uniform neutralizing background. In the experiment, the pulse length is actually 1 ps (and the inverse of the ion plasma period is 2.5 ps so ion motion could be important at the back of the pulse) and the plasma is formed by self-ionization which leads to a fully ionized plasma over several spot sizes. The results from this code[25, 8] have been shown to be in agreement with other observables from this experiment, such as the number of Stokes and anti-Stokes satellites, and the fractional laser light transmitted from an experiment by C. Coverdale et al.[19]

As discussed elsewhere,[25] the laser pulse undergoes a complex spatial-temporal evolution of Raman scattering (back/side/forward), and self-focusing/filamentation. The front of the pulse etches away from Raman sidescatter leading to a deformed laser pulse envelope. This deformation generates a wake which seeds Raman

forward scattering. The phase velocity of the wake as computed from $v_{ph} = v_g$ corresponds for our simulation parameters to $\gamma_{ph}^2 = 70$. However, the simulation results show that the phase velocity of the first few wavelengths of the wake initially correspond to $\gamma_{ph}^2 = 50$. In other words, $v_{ph} \neq v_g$. We believe this discrepancy to be real, probably due to the reduction in phase velocity of the wake caused by the etching away of the front of the laser pulse[29]. Based on the value $\gamma_{ph}^2 = 50$ one would expect the energy gain of particles (once trapped) to cease because of dephasing after 0.22 mm. However, we will see that once wavebreaking occurs γ_{ph} can increase in localized regions of the laser pulse so that acceleration can occur over lengths greater than expected within certain accelerating buckets.

For this simulation, the accelerating plasma wave breaks after the leading edge of the pulse has propagated approximately 0.4 mm into the plasma slab. At this point the maximum normalized amplitude of the accelerating field is quite close to $\epsilon = 1$. Once wavebreaking occurs and a significant number of electrons are self-trapped the wave amplitude is reduced to $0.25 < \epsilon < 0.65$ because of beam loading. In other words the trapped electrons are accelerated at an average ϵ of less than 1. This is illustrated in figure 4.10(a) where we plot the normalized accelerating field on axis, E_x, and the normalized longitudinal momentum, P_x, of electrons above 4 MeV vs. $(x - ct)$ for the plasma wave buckets containing the most energetic trapped particles. The front of the laser pulse is at $(x - ct) = 0$, while x is held fixed at 1 mm. Although not shown here, prior to wavebreaking, only a few particles are trapped in these buckets, and their energies are limited to about 5 MeV. As can be seen in figure 4.10(a) the electrons are accelerated up to 80 MeV while E_x is much less than 1 for all the buckets. The peak electron

energies are therefore beyond the linear dephasing estimate of $2\epsilon\gamma_{ph}^2 mc^2$, which even for an ϵ of .65 and γ_{ph}^2 of 50 gives $W = 42$ MeV. Furthermore, it is clear that the plasma wave has lost its coherence (i.e., its wavelength is not constant) and that some particles are still at peak accelerating regions while others are at peak decelerating regions. This illustrates that once wavebreaking occurs the plasma wave's phase velocity is not given by the simple theory.

We have observed in this and several other simulations that beam loading has a profound effect on both the coherence of the plasma wave and on the instantaneous phase velocity of the buckets in which the electrons are trapped[8]. We have seen that within the laser pulse envelope, particles trapped in the later buckets are the ones that gain the highest energies even though the wave amplitude is neither the largest nor the most sinusoidal there. As the particles trapped in the earlier buckets gain energy, the wake produced by them similarly accelerates. The total electric field is the superposition of the original wave field and the wake field induced by the trapped particles. This total field consequently not only becomes incoherent because of the large energy spread of the trapped particles in the earlier buckets, but the effective phase velocity of this field increases. This appears to cause some particles in the later buckets to gain energies higher than the linear dephasing limit.

Simulations with γ_{ph} between 7 and 9 produced very similar electron spectra at the highest energies, as did the experiment. A possible reason for this could be that at high density, although γ_{ph} is smaller, more electrons are trapped and accelerated more rapidly causing the effective phase velocity of the beam loaded wave (later buckets) to become greater than it is at lower density.

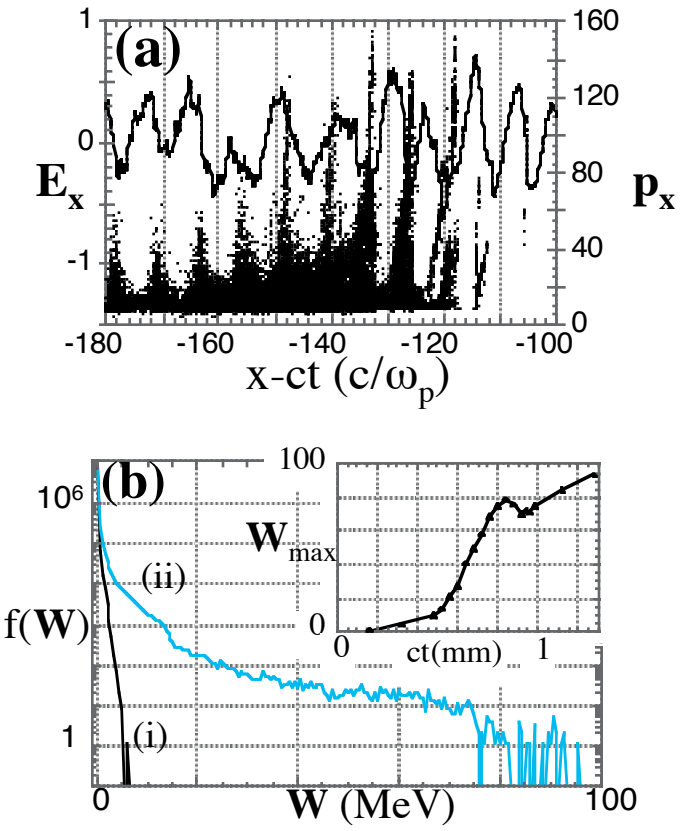

Figure 4.10: (a) The normalized electric field E_x (lines) in units of $mc\omega_p/e$ and the normalized electron longitudinal momentum P_x (dots) in units of mc vs. distance from the leading edge of the laser pulse $(x - ct)$ in units of c/ω_p fixing x at 1 mm into the plasma. (b) Maximum electron energy $W_{\max}$ in MeV vs. ct (inset) and the electron distribution functions at $ct = 0.4$ mm (i) and 1.3 mm (ii).

To further illustrate that some of the trapped particles have gone beyond the simple dephasing estimate, we plot the energy of the most energetic electrons vs. ct in figure 4.10(b) inset. We see that in an average sense the electrons with maximum energy at any given ct are accelerated at a nearly constant rate from $ct \approx 0.5$ mm to 0.85 mm. If simple dephasing were occuring then the rate would not be constant and, in fact, particles would begin to lose energy beyond the dephasing length of 0.22 mm. Over this distance the average E_x is 0.65 which corresponds to a gradient of ≈ 2.4 GeV/cm. Note further that after 0.85 mm the peak electron energy dips but then begins to increase further to a peak value of ≈ 95 MeV demonstrating the turbulent nature of acceleration. Since the plasma slab is only 1 mm thick, electron energy gain beyond $ct = 1$ mm is due to accelerating buckets in the back of the laser pulse since the front of the pulse has exited the plasma. Following wavebreaking, which occurs at $ct = 0.4$ mm, most of this energy gain occurs in ≈ 0.6 mm. This is consistent with the measurment of the spatial profile of the plasma wave shown in figure 4.7 inset.

4.6 Multiple Bunch Beamloading

In the last section, it was shown that wavebreaking leads to turbulent, localized modulations in the phase of the accelerating field. It was inferred that these modulations can be explained in terms of beamloading, and further, that they lead to acceleration beyond the dephasing limit. To demonstrate this more directly, we develop a simple one-dimensional numerical model which regards the phase modulation as the result of beamloading by discrete electron bunches. Beamloading is the generation of a wake behind each bunch which interferes with the

accelerating field such that energy is conserved.

Consider a set of highly localized electron bunches with positions $\{x_i\}$, charges $\{q_i\}$, and velocities $\{v_i\}$. The wake due to each bunch is well known to be [2]

$$E_i(x) = -4\pi q_i H(x_i - x) \cos k_i (x_i - x) \tag{4.8}$$

where $k_i = \omega_p / v_i$, and H is defined by

$$H(x) = \begin{cases} 1 & x > 0 \\ 1/2 & x = 0 \\ 0 & x < 0 \end{cases} \tag{4.9}$$

The stipulation $H(0) = 1/2$ is needed to accurately model the self-force on each bunch. This can be seen by considering a finite bunch and letting its size become arbitrarily small. The field due to the whole system is the superposition of all the wake-fields with the main accelerating field:

$$E(x) = E_0 \cos k_p (x - v_\phi t) + \sum_i E_i(x) H\left(\frac{v_i}{c} - \frac{1}{4}\right) \tag{4.10}$$

Here, v_ϕ is the phase velocity of the accelerating field and $k_p = \omega_p / v_\phi$. The factor H eliminates any wakes caused by non-relativistic or backward-moving bunches. These wakes must be neglected since their wavelengths are too small to resolve efficiently. The system of equations is closed using $v = \dot{x}$ along with the equation of motion for each bunch

$$\partial_t (\gamma_i m v_i) = -eE(x_i) \tag{4.11}$$

Here, e and m are the electronic charge and mass, and γ_i is the Lorentz factor associated with v_i.

Table 4.1: Parameters for Run 1

Quantity	Value
Time Step	0.01
Steps	$300,000$
Field Amplitude	$E_0/E_{\max} = 0.7$
Field Lorentz Factor	$\gamma_\phi = 8.5$
Bunches	none
Test Particle Start Point	$k_p x = -27.9494$
Test Particle Charge	$q = 0$
Test Particle Lorentz Factor	$\gamma = 8.5$

By integrating the above set of equations on a computer, one can find by trial and error a case such that for modest parameters ($4\pi q \approx 0.1E_0$, $E_0 \approx 0.5E_{\max}$) acceleration beyond the dephasing limit is achieved. To illustrate this, we consider three cases in order of increasing complexity. For the first case, called "run 1", we simply consider a test particle in a sinusoidal accelerating field, phased such that the maximum possible energy gain is attained. The parameters for this run are given in table 4.1. In the second case, called "run 2", we consider a test particle trailing a charged bunch modeled without the self force. The bunch charge and the accelerating field are chosen so that the peak amplitude of the total accelerating field equals the peak amplitude from run 1. In the last case, called "run 3", we consider the same situation as in run 2 except that several charged bunches are placed in close proximity to one another. Also, in run 3 the self-force is included. The exact parameters for runs 2 and 3 are indicated in tables 4.2 and 4.3.

The momentum histories for the test particle in each of the three runs are shown in figure 4.11. In the case of run 1, we see that as expected the maximum

Table 4.2: Parameters for Run 2

Quantity	Value
Time Step	0.01
Steps	$300,000$
Field Amplitude	$E_0/E_{\max} = 0.35$
Field Lorentz Factor	$\gamma_\phi = 8.5$
Bunches	1
Bunch Start Point	$k_p x = -12.192$
Bunch Charge	$4\pi q = -.35$
Bunch Lorentz Factor	$\gamma = 100$
Test Particle Start Point	$k_p x = -27.9494$
Test Particle Charge	$q = 0$
Test Particle Lorentz Factor	$\gamma = 8.5$

Table 4.3: Parameters for Run 3

Quantity	Value
Time Step	0.01
Steps	$300,000$
Field Amplitude	$E_0/E_{\max} = 0.35$
Field Lorentz Factor	$\gamma_\phi = 8.5$
Bunches	$i = \{0, 2, ..., 9\}$
Bunch Start Point	$k_p x_i = -12.1915 - 0.0001i$
Bunch Charge	$4\pi q_i = -.035$
Bunch Lorentz Factor	$\gamma_i = 100 + 5i$
Test Particle Start Point	$k_p x = -27.9494$
Test Particle Charge	$q = 0$
Test Particle Lorentz Factor	$\gamma = 8.5$

energy of the particle is limited by dephasing. In the case of run 2, however, we see that the dephasing limit is easily surpassed, and indeed, the particle never stops gaining energy. The reason for this is made clear by considering snapshots of the electric field along with the particle positions, as illustrated in figure 4.12. As the test particle eventually approaches a decelerating region the two wakes destructively interfere dropping the wake amplitude to exactly zero. When the bunch driver moves further ahead of the original wake, the total wake amplitude begins to increase, but the phase of the total wake shifts by π so that the test particle is now in a region of accelerating phase. This phase locking will last until the particle dephases from the bunch driver.

In the case of run 3, figure 4.11 shows that the test particle again surpasses the dephasing limit, but the particle does begin to lose energy after a certain point. The electric field snapshots and particle positions for this case are shown in figure 4.13. We see that the situation is similar to that of run 2, except that the inclusion of self-forces and the effects of multiple bunches lead to a less ideal accelerating structure.

4.7 Conclusions

It has been demonstrated experimentally that when wavebreaking occurs, the maximum energy gain in a self-modulated laser accelerator is not limited by the simple dephasing estimates of linear theory. Electron spectra and collective Thomson scattering data have been obtained simultaneously, allowing comparison of the electron energies with key properties of the accelerating structure. Particle simulations suggest that multiple-bunch beam loading is largely responsible for

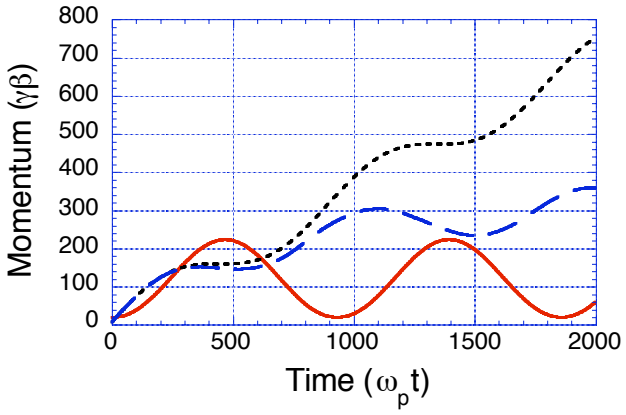

Figure 4.11: Momentum history for runs 1, 2 and 3. The solid line is the orbit for a test particle which achieves maximum energy gain in the accelerating field alone. The dotted line is the orbit for a test particle trailing a charged bunch with no self-force. The dashed line is the orbit for a test particle trailing several charged bunches with the self-force modeled correctly. The dephasing limit is exceeded by a factor of approximately 3/2.

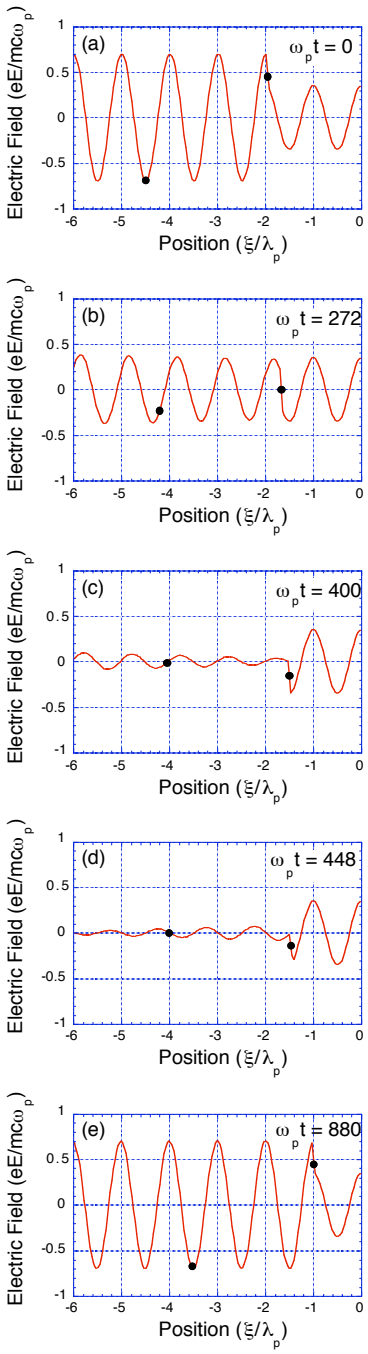

Figure 4.12: Idealized evolution of the electric field. Bunch positions are indicated by dots. (a) A charged bunch starts at $\xi \approx -2\lambda_p$ and a test particle starts at $\xi \approx -4.5\lambda_p$. (c) The wave amplitude is reduced as the test particle slips into the decelerating phase. (d) The particle moves back into the accelerating phase very quickly. (e) The amplitude then increases again.

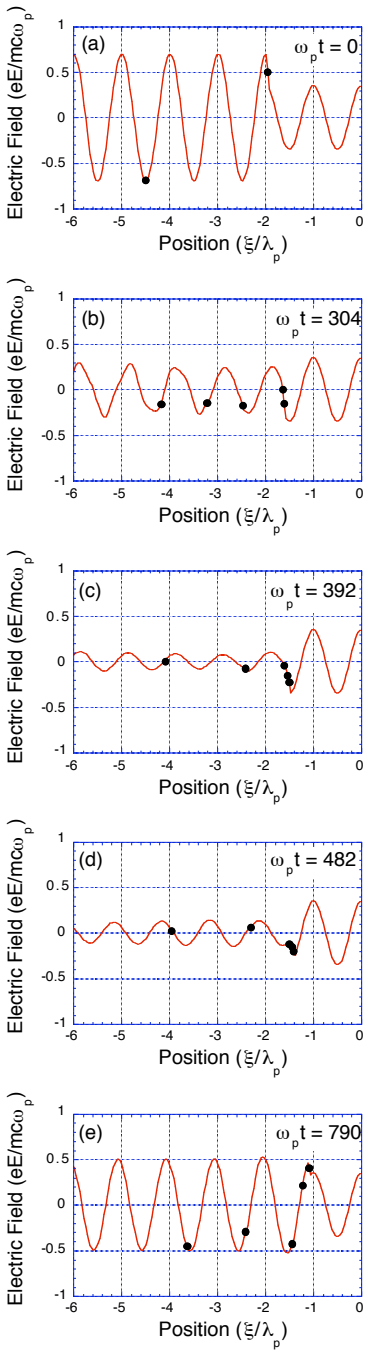

Figure 4.13: Evolution of the electric field with self-forces. (a) Several bunches start at distinct positions near $\xi \approx -2\lambda_p$. The test particle is at $\xi \approx -4.5\lambda_p$. (b-e) The test particle is accelerated in a manner similar to that of the idealized case, but not quite as favorable.

the local phase modifications which result in enhanced acceleration. In addition, self-focusing of the laser has been quantitatively demonstrated by observing the plasma waves driven in the resulting laser-channel. No clear correlation was observed between self-guiding and electron production in the energy range 30-100 MeV.

Part II

Electromagnetically Induced Transparency in Plasma

Chapter 5

Introduction and Basic Relations

5.1 Introduction

Electromagnetically induced transparency (EIT) is a process whereby the interaction between intense radiation and a medium causes the medium to become transparent to a range of frequencies which would normally be reflected or absorbed. This process was demonstrated experimentally in strontium vapor by Boller *et al* in 1991 [33]. Recently, it was proposed by S.E. Harris that a similar process might occur in plasma [3].

In an ordinary dielectric medium, light waves are affected by the dipole moment they induce on the atoms in the medium. If the light wave drives the atom below its resonant frequency, the phase of the scattered wave is such that constructive interference occurs in the forward direction. If the light wave drives the atom above its resonant frequency, the phase of the scattered wave is such that destructive interference occurs in the forward direction. Because of this, radiation with frequency just above the resonant frequency fails to penetrate the medium. For frequencies much higher than the resonant frequency radiation is

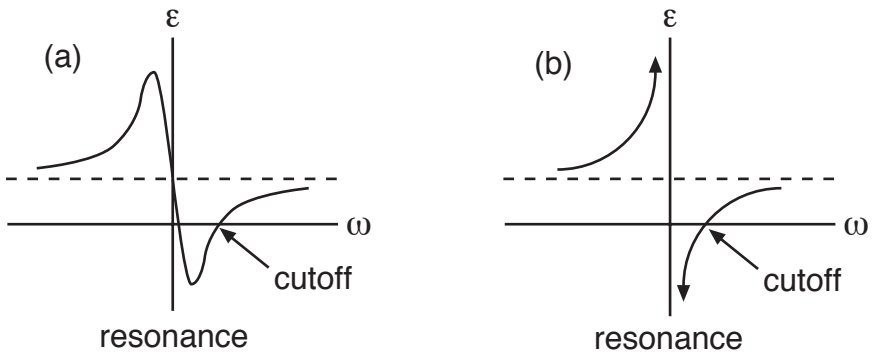

Figure 5.1: Dispersion in an ordinary medium (a) with damping (b) without damping. The dotted horizontal line marks where $\epsilon = 1$. The solid horizontal line corresponds to $\epsilon = 0$. The refractive index is $\epsilon^{1/2}$ which is imaginary between the resonant frequency and the cutoff.

again transmitted since the interaction with the atom is then weak. Thus, in the case where absorption is neglected, there is a stopband bounded below by the resonant frequency and bounded above by the cutoff frequency. This is illustrated in figure 5.1(b) which shows the dispersion curve for a lossless atomic medium in the vicinity of a resonance. The situation may not be as simple when the atomic dipoles are driven nonlinearly due to the presence of intense radiation. In this case, the dipole moment may acquire frequency components not contained in the incident radiation. If one of these frequencies lies in the stopband predicted by linear theory, radiation at that frequency could be transmitted depending on the phasing of the nonlinear oscillation.

In a plasma, the resonant frequency is zero while the cutoff frequency is the plasma frequency. The dispersion curve is the same as the one shown in figure 5.1(b) except that the left half of the plot is not applicable. For small amplitude electromagnetic waves in one dimension, the electron current is a linear

function of the applied field. For large amplitude electromagnetic waves, there are two sources of nonlinearity. First, when the relativistic mass increase of the electrons becomes significant, the electron current is smaller than it would be otherwise since the momentum rather than the velocity is proportional to the applied field. This reduces the amplitude of the scattered wave and makes propagation easier. Second, the magnetic field associated with the radiation causes longitudinal particle motions which result in a density perturbation. Currents driven in the density perturbation will have frequency components not contained in the driving field. If these frequencies lie in the stopband, anomalous transparency might occur.

In this dissertation, we investigate EIT in a plasma. In the original work of Harris, two electromagnetic waves were considered. An intense wave, the "pump", with frequency above the cutoff was propagated simultaneously with a weaker wave, the "Stokes", with frequency below the cutoff. The beating of the two waves drove a density perturbation which led to nonlinear currents allowing the Stokes wave to propagate. Here, we extend the analysis to include a third wave, the "anti-Stokes", at a frequency higher than that of the pump. We also consider relativistic effects, the stability of the plasma, and most importantly, the effect of boundaries. It is found that in a bounded system, induced transparency cannot occur in the strict sense. However, it is possible to *generate* propagating waves in a stopband. Computer simulations are used throughout to support the analysis.

5.2 Normalized Units

Normalized units are used throughout the following analysis. In particular, velocity is normalized to the speed of light, density is normalized to the plasma density, charge is normalized to the electronic charge, and mass is normalized to the electronic mass. It follows that if the plasma frequency in ordinary units is ω_p, then the unit of time is ω_p^{-1} and the unit of distance is c/ω_p. Also, with the vector potential normalized to mc/e (with respect to mks units), the electromagnetic field equations are

$$(\Delta - \partial_{tt})\mathbf{A} = -j + \nabla(\nabla \cdot \mathbf{A} + \partial_t \phi) \tag{5.1}$$

$$\Delta\phi + \partial_t(\nabla \cdot \mathbf{A}) = -\rho \tag{5.2}$$

where $\mathbf{A}$ is the vector potential, ϕ is the scalar potential, j is the current density and ρ is the charge density. Here, no particular gauge has been committed to. The relativistic equation of motion for a fluid element is

$$\partial_t \mathbf{p} = \nabla\phi + \partial_t \mathbf{A} - \mathbf{v} \times \nabla \times \mathbf{A} - (\mathbf{v} \cdot \nabla)\mathbf{p} \tag{5.3}$$

where $\mathbf{p}$ is the electron momentum and $\mathbf{v}$ is the velocity.

5.3 Starting Equations

5.3.1 Inhomogeneous Plasma

Consider a cold unmagnetized plasma wherein all quantites vary only in the x-direction. Let the electron density be described by

$$n = n_0(x) + n_1(x, t) \tag{5.4}$$

where n_0 is constant in time and is neutralized by a background of immobile ions. Consider further linearly polarized electromagnetic waves described by a vector potential $\mathbf{A} = A_x(x,t)\hat{\mathbf{x}} + A_y(x,t)\hat{\mathbf{y}}$ where $\hat{\mathbf{x}}$ and $\hat{\mathbf{y}}$ are the unit vectors.[1] We seek a pair of coupled equations involving only A_y and the density perturbation n_1. We begin with the wave equation for A_y:

$$(\partial_{xx} - \partial_{tt})A_y = -j_y = nv_y - \mathcal{J}(x,t) = \frac{np_y}{\gamma} - \mathcal{J}(x,t) \tag{5.5}$$

where $\mathcal{J}$ is an externally driven current, v_y is the velocity of a fluid element, and np_y is the corresponding momentum density. Since y is a cyclic coordinate, $p_y = A_y$ by conservation of canonical momentum. Also,

$$\frac{1}{\gamma} = (1+p^2)^{-1/2} = 1 - \frac{A_y^2}{2} + O(A_y^4) \tag{5.6}$$

provided $p_x = O(p_y^2)$. Substituting these results into the wave equation gives

$$(\partial_{xx} - \partial_{tt})A_y = (n_0 + n_1)\left(1 - \frac{A_y^2}{2}\right)A_y - \mathcal{J}(x,t) + O(A_y^4) \tag{5.7}$$

We now take $n_1 = O(A_y)$. This requires that the term $A_y^3 n_1/2$ be absorbed into the $O(A_y^4)$ terms. With the assumption that $A_y \ll 1$ the equation for A_y is then:

$$(\partial_{xx} - \partial_{tt} - n_0)A_y = \left(n_1 - n_0\frac{A_y^2}{2}\right)A_y - \mathcal{J}(x,t) \tag{5.8}$$

The equation for n_1 comes from the continuity equation:

$$-\partial_t n_1 = \partial_x\left[(n_0 + n_1)v_x\right] \tag{5.9}$$

[1]The x-component will not be needed in the forthcoming analysis, but could be present depending on the gauge.

Suppose for the moment that $n_1 v_x = O(A_y^4)$. Then differentiating with respect to time gives

$$-\partial_{tt} n_1 = \partial_x n_0 \partial_t v_x + n_0 \partial_{xt} v_x + O(A_y^4) \tag{5.10}$$

The axial velocity v_x can be eliminated using the momentum equation along with the differential form of Gauss' law. The momentum equation is

$$\partial_t p_x = -E_x - v_y \partial_x A_y - v_x \partial_x p_x \tag{5.11}$$

where E_x is the axial electric field. This expands to

$$\partial_t \left[v_x \left(1 + \frac{A_y^2}{2} \right) \right] = -E_x - \left(1 - \frac{A_y^2}{2} \right) \left(A_y \partial_x A_y - p_x \partial_x p_x \right) + O(A_y^4) \tag{5.12}$$

The convective term and all the relativistic terms are fourth order and must be collected with the fourth order terms left over from the expansion of the relativistic Lorentz factor. We note that this results in the elimination of the relativistic frequency shift of the plasma wave. The resulting equation is

$$\partial_t v_x = -E_x - \partial_x \left(\frac{A_y^2}{2} \right) + O(A_y^4) \tag{5.13}$$

The electric field E_x can be expressed in terms of n_1 via the Maxwell equation $\partial_x E_x = -n_1$. This leads to

$$\partial_t v_x = \int n_1 dx - \partial_x \left(\frac{A_y^2}{2} \right) \tag{5.14}$$

and

$$\partial_{xt} v_x = n_1 - \partial_{xx} \left(\frac{A_y^2}{2} \right) \tag{5.15}$$

We see that $n_1 = O(A_y)$ is inconsistent with the previous requirement $v_x = O(A_y^2)$. Instead, we must have $n_1 = O(A_y^2)$ which leads to $n_1 v_x = O(A_y^4)$ as was

supposed in writing equation 5.10. Finally, inserting the expressions for $\partial_t v_x$ and $\partial_{xt} v_x$ into equation 5.10 gives

$$-(\partial_{tt} + n_0)n_1 = \partial_x n_0 \left(\int n_1 dx - \partial_x \frac{A_y^2}{2} \right) - n_0 \partial_{xx} \frac{A_y^2}{2} \tag{5.16}$$

Equations 5.8 and 5.16 are the starting equations for an inhomogeneous plasma.

5.3.2 Homogeneous Plasma

In the case of a homogeneous plasma $n_0 = 1$ and the equation for A_y becomes

$$(\partial_{xx} - \partial_{tt} - 1)A_y = \left(n_1 - \frac{A_y^2}{2} \right) A_y - \mathcal{J}(x,t) \tag{5.17}$$

while the equation for n_1 becomes

$$-(\partial_{tt} + 1)n_1 = -\partial_{xx} \frac{A_y^2}{2} \tag{5.18}$$

In frequency space, the density perturbation can be expressed explicitly in terms of the vector potential:

$$\hat{n}_1 = \frac{k^2}{4\pi(\omega^2 - 1)} (\hat{A}_y * \hat{A}_y) \tag{5.19}$$

where the circumflex denotes a Fourier transformed quantity and the asterisk denotes convolution. Then the vector potential in frequency space can be found from the single integral equation

$$(\omega^2 - k^2 - 1)\hat{A}_y = \left[\left(\frac{k^2}{\omega^2 - 1} - 1 \right) (\hat{A}_y * \hat{A}_y) \right] * \frac{\hat{A}_y}{8\pi^2} - \hat{\mathcal{J}}(\omega, k) \tag{5.20}$$

5.4 Normal Modes and Causality

Equation 5.20 is useful if it approximates the response of a plasma to some physically realizable source of radiation. The source must therefore satisfy the

requirement of causality. In particular, the prescribed current $\mathcal{J}$ must satisfy $\mathcal{J}(x,t) = 0$ for $t < 0$ but must be nonzero somewhere. Nevertheless, in this chapter we solve for the normal modes of the plasma which are found by setting $\mathcal{J} = 0$ at all times. We comment, therefore, on the relationship between the normal modes of the plasma and the response of the plasma to an external source.

It is convenient to rewrite equation 5.20 as follows:

$$\hat{L}(\omega,k)\hat{A} = \hat{N}(\hat{A}) - \hat{\mathcal{J}}(\omega,k) \tag{5.21}$$

where

$$\hat{L}(\omega,k) = \omega^2 - k^2 - 1 \tag{5.22}$$

and $\hat{N}$ is a nonlinear operator defined by

$$\hat{N}(\hat{A}) = \left[\left(\frac{k^2}{\omega^2-1} - 1\right)(\hat{A} * \hat{A})\right] * \frac{\hat{A}}{8\pi^2} \tag{5.23}$$

which returns the nonlinear part of the current density. Note that we have dropped the y subscript on $\hat{A}$. If the nonlinear term is neglected then $\hat{A} = -\hat{\mathcal{J}}/\hat{L}$ and the response of the plasma to an arbitrary source is simply

$$A(x,t) = -G(x,t) * \mathcal{J}(x,t) \tag{5.24}$$

where

$$\hat{G}(\omega,k) = \frac{1}{\hat{L}(\omega,k)} \tag{5.25}$$

In other words, $\hat{L}$ is the reciprocal of the frequency space representation of the Green's function for a linear plasma.

In the linear case, the Green's function is closely related to the normal modes of the system which are found from

$$\hat{L}\hat{A} = 0 \tag{5.26}$$

The general solution is

$$\hat{A} = A_0\delta(\omega + \omega_0, k - k_0) + A_0^*\delta(\omega - \omega_0, k + k_0) \tag{5.27}$$

where A_0 is a constant and ω_0 and k_0 satisfy the dispersion relation

$$\hat{L}(\omega_0, k_0) = 0 \tag{5.28}$$

The poles of the Green's function are therefore the zeroes of the dispersion function.

When the nonlinear term is included the situation is much more complicated. Consider the action of the operator $\hat{N}$ on a series of delta functions. First, we introduce the shorthand notation

$$\Delta_i = A_i\delta(\omega + \omega_i, k - k_i) + A_i^*\delta(\omega - \omega_i, k + k_i) \tag{5.29}$$

which is just the frequency space representation of

$$\frac{A_i}{2\pi}e^{i(\omega_i t - k_i x)} + cc \tag{5.30}$$

Sum or difference frequencies can be represented in the following compact way:

$$\Delta_{i+j} = A_iA_j\delta(\omega + \omega_i + \omega_j, k - k_i - k_j) + A_i^*A_j^*\delta(\omega - \omega_i - \omega_j, k + k_i + k_j) \tag{5.31}$$

$$\Delta_{i-j} = A_iA_j^*\delta(\omega + \omega_i - \omega_j, k - k_i + k_j) + A_i^*A_j\delta(\omega - \omega_i + \omega_j, k + k_i - k_j) \tag{5.32}$$

which is useful since

$$\Delta_i * \Delta_j = \Delta_{i+j} + \Delta_{i-j} \tag{5.33}$$

Now let

$$\hat{A} = \sum_{i=0}^{n} \pi\Delta_i \tag{5.34}$$

Inserting this into the expression for $\hat{N}(\hat{A})$ one finds that

$$\hat{N}(\hat{A}) = \frac{\pi}{8}\sum_{i=0}^{n}\sum_{j=0}^{n}\sum_{k=0}^{n} P_{i+j}(\Delta_{i+j+k} + \Delta_{i+j-k}) + P_{i-j}(\Delta_{i-j+k} + \Delta_{i-j-k}) \quad (5.35)$$

where

$$P_{i\pm j} = \frac{(k_i \pm k_j)^2}{(\omega_i \pm \omega_j)^2 - 1} - 1 \quad (5.36)$$

The second term of $P_{i\pm j}$ is the relativistic correction. The nonrelativistic part of $P_{i\pm j}\Delta_{i\pm j\pm k}$ represents the scattering of the wave at ω_k off the density perturbation driven by the waves at ω_i and ω_j. This generates a wave at $\omega_i \pm \omega_j \pm \omega_k$. In other words, the presence of any set of frequencies implies the presence of all possible sums or differences of any three of those frequencies. This implies that for any frequency supposed present, all its odd harmonics must be present as well. Hence, an infinite number of frequencies are required to strictly satisfy $\hat{L}\hat{A} = \hat{N}(\hat{A})$. Approximations must be used to truncate the series.

5.5 Three Wave Solution

The infinite series of delta functions needed to solve $\hat{L}\hat{A} = \hat{N}(\hat{A})$ can be truncated by noting that P_{i-j} is large when $\omega_i - \omega_j \approx 1$. Consider the vector potential

$$\hat{A} = \pi\Delta_0 + \pi\Delta_1 + \pi\Delta_2 \quad (5.37)$$

where $\omega_1 = \omega_0 - \Delta\omega$, $k_1 = k_0 - \Delta k$, $\omega_2 = \omega_0 + \Delta\omega$, and $k_2 = k_0 + \Delta k$. The first term is called the "pump" wave, the second is called the "Stokes" wave, and the third is called the "anti-Stokes" wave. If $\Delta\omega \approx 1$ then only terms with coefficients P_{0-1}, P_{0-2}, P_{1-0}, or P_{2-0} need be retained. Furthermore, supposing that $A_0 \gg A_1$ and $A_0 \gg A_2$ one may take only the first term in the summation

over k in equation 5.35. With these approximations, one has

$$\hat{L}\hat{A} = \frac{\pi}{4}\left\{P_{1-0}[\Delta_{1-0+0} + \Delta_{1-0-0}] + P_{2-0}[\Delta_{2-0+0} + \Delta_{2-0-0}]\right\} \tag{5.38}$$

Equating the coefficients of each δ-function results in three equations:

$$\hat{L}(\omega_0, k_0)A_0 = 0 \tag{5.39}$$

$$\hat{L}(\omega_1, k_1)A_- = \frac{|A_0|^2}{4}(P_{1-0}A_- + P_{2-0}A_+) \tag{5.40}$$

$$\hat{L}(\omega_2, k_2)A_+ = \frac{|A_0|^2}{4}(P_{1-0}A_+ + P_{2-0}A_-) \tag{5.41}$$

where $A_- = A_1$ and $A_+ = A_2^*$. The dispersion relation for the pump wave follows immediately from equation 5.39:

$$k_0^2 = \omega_0^2 - 1 \tag{5.42}$$

Equations 5.40 and 5.41 relate the sideband amplitudes. Taking A_0 to be real and rewriting these in matrix form gives

$$\begin{pmatrix} D_- - A_0^2P/4 & -A_0^2P/4 \\ -A_0^2P/4 & D_+ - A_0^2P/4 \end{pmatrix} \begin{pmatrix} A_- \\ A_+ \end{pmatrix} = 0 \tag{5.43}$$

where

$$D_\pm = (\Delta\omega^2 - \Delta k^2) \pm 2(\Delta\omega\omega_0 - \Delta k k_0) \tag{5.44}$$

and

$$P = \frac{\Delta k^2}{\Delta\omega^2 - 1} - 1 \tag{5.45}$$

The dispersion relation between $\Delta\omega$ and Δk is found by setting the determinant to zero. This leads to

$$\left(\frac{1}{D_+} + \frac{1}{D_-}\right) P\frac{A_0^2}{4} = 1 \tag{5.46}$$

where terms of order A_0^4 were dropped since the original equations were only accurate to order A_0^3. Note that dropping the relativistic correction to P results in the classic Raman dispersion relation [34, 35].

The fact that the determinant of the system describing the sidebands is zero indicates that one of the sideband amplitudes can be chosen arbitrarily. The other can then be found from either equation 5.40 or 5.41 which give the ratio between the two:

$$\frac{A_-}{A_+} = \frac{A_0^2 P/4}{D_- - A_0^2 P/4} = \frac{D_+ - A_0^2 P/4}{A_0^2 P/4} \tag{5.47}$$

Since A_0 can be chosen arbitrarily as well, the scaling $A_0 \gg A_1$ and $A_0 \gg A_2$ can indeed be prescribed.

5.6 Two Wave Solution

It might be that at certain points on the dispersion curve $A_+ \ll A_-$. Then one obtains the equations:

$$\hat{L}(\omega_0, k_0) A_0 = 0 \tag{5.48}$$

and

$$\hat{L}(\omega_0 - \Delta\omega, k_0 - \Delta k) A_- = \frac{A_0^2}{4} P A_- \tag{5.49}$$

Dropping the relativistic correction to P results in

$$4(\Delta\omega^2 - 1) D_- = \Delta k^2 A_0^2 \tag{5.50}$$

Since this is quadratic in Δk an explicit expression for Δk can be obtained:

$$\Delta k = \frac{k_0 \pm \sqrt{k_0^2 + (\Delta\omega^2 - 2\omega_0 \Delta\omega) f(A_0, \Delta\omega)}}{f(A_0, \Delta\omega)} \tag{5.51}$$

where

$$f(A_0, \Delta\omega) = \frac{\Delta\omega^2 - (1 - A_0^2/4)}{\Delta\omega^2 - 1} \tag{5.52}$$

The function f accounts for nonlinear effects. It departs significantly from unity only near the resonance at $\Delta\omega = 1$.

5.7 Harris Solution

If equation 5.50 is expanded in the parameter $\delta\omega$ where $\Delta\omega = 1 + \delta\omega$, the dispersion relation derived in the paper by Harris can be recovered. Inserting $1 + \delta\omega$ into equation 5.50 and dropping all terms of order $\delta\omega^2$ or higher results in

$$2\delta\omega(1 - \Delta k^2 - 2\omega_0 + 2\Delta k k_0) = \Delta k^2 \frac{A_0^2}{4} \tag{5.53}$$

It is important to note that a dispersion relation linear in ω forces ω to be real if k is real. Therefore any instabilities in the system will automatically be missed by such an approximation.

5.8 Multiple Resonance Solution

The dispersion relations presented above are valid only assuming $\Delta\omega \approx 1$. When this is not the case one must consider couplings into the density perturbation at frequencies other than $\Delta\omega$. Consider again the vector potential

$$\hat{A} = \pi\Delta_0 + \pi\Delta_1 + \pi\Delta_2 \tag{5.54}$$

Inserting this into equation 5.19 and dropping terms quadratic in the sideband amplitudes reveals the density perturbation to consist of the frequencies $\Delta\omega$, $2\omega_0$,

$2\omega_0 - \Delta\omega$, and $2\omega_0 + \Delta\omega$. If any of these approach unity in the frequency range of interest they will couple strongly into the solution for the fields.

Table 5.1 provides information on all the terms of $\hat{N}(\hat{A})$ which are linear in the sideband amplitudes. Referring to the table headings, $(\pi/8)P_{ij}A_{ijk}$ is the coefficient of a delta function at the frequency ω_{ijk}. For each such entry there is also a delta function at the frequency $-\omega_{ijk}$ with coefficient $(\pi/8)P_{ij}A^*_{ijk}$. Note also that not all the permutations of $P_{i\pm j}$ are listed since one may use $P_{i\pm j}\Delta_{i\pm j} = P_{j\pm i}\Delta_{j\pm i}$ to quickly deduce the necessary information. The entry ω_{ij} is the frequency of the density perturbation and the entry k identifies the wave with which it interacts. This information is useful for purposes of interpretation. Note that the terms corresponding to P_{0-0} contain the relativistic correction only. They do not imply there is a density perturbation at zero frequency.

The nonlinear terms involving frequencies at $3\omega_0$ and $3\omega_0 \pm \Delta\omega$ present a problem in that they imply the presence of frequencies not originally supposed present in $\hat{A}$. If these frequencies were taken into account, they would couple back into the frequencies ω_0, ω_1, and ω_2. We must suppose, therefore, that this coupling is negligible.

Making use of table 5.1, one can quickly collect the terms at each frequency ω_0, ω_1, and ω_2 and equate them with the appropriate terms from the expression $\hat{L}\hat{A}$. This leads to the following equations relating the three wave amplitudes:

$$L_0 = \frac{A_0^2}{4}\left(P_{0-0} + \frac{P_{0+0}}{2}\right) \tag{5.55}$$

$$L_-A_- = \frac{A_0^2}{4}\left[A_-(P_{0-0} + P_{0+1} + P_{0-1}) + A_+\left(\frac{P_{0+0}}{2} + P_{0-2}\right)\right] \tag{5.56}$$

$$L_+A_+ = \frac{A_0^2}{4}\left[A_+(P_{0-0} + P_{0+2} + P_{0-2}) + A_-\left(\frac{P_{0+0}}{2} + P_{0-1}\right)\right] \tag{5.57}$$

Table 5.1: Couplings Involving Three Waves

P_{ij}	ω_{ij}	k	ω_{ijk}	A_{ijk}
P_{0-0}	0	$+0$	ω_0	A_0^3
P_{0-0}	0	-0	$-\omega_0$	A_0^3
P_{0-0}	0	$+1$	$\omega_0 - \Delta\omega$	$A_0^2 A_1$
P_{0-0}	0	-1	$-\omega_0 + \Delta\omega$	$A_0^2 A_1^*$
P_{0-0}	0	$+2$	$\omega_0 + \Delta\omega$	$A_0^2 A_2$
P_{0-0}	0	-2	$-\omega_0 - \Delta\omega$	$A_0^2 A_2^*$
P_{0+0}	$2\omega_0$	$+0$	$3\omega_0$	A_0^3
P_{0+0}	$2\omega_0$	-0	ω_0	A_0^3
P_{0+0}	$2\omega_0$	$+1$	$3\omega_0 - \Delta\omega$	$A_0^2 A_1$
P_{0+0}	$2\omega_0$	-1	$\omega_0 + \Delta\omega$	$A_0^2 A_1^*$
P_{0+0}	$2\omega_0$	$+2$	$3\omega_0 + \Delta\omega$	$A_0^2 A_2$
P_{0+0}	$2\omega_0$	-2	$\omega_0 - \Delta\omega$	$A_0^2 A_2^*$
P_{0+1}	$2\omega_0 - \Delta\omega$	$+0$	$3\omega_0 - \Delta\omega$	$A_0^2 A_1$
P_{0+1}	$2\omega_0 - \Delta\omega$	-0	$\omega_0 - \Delta\omega$	$A_0^2 A_1$
P_{0+2}	$2\omega_0 + \Delta\omega$	$+0$	$3\omega_0 + \Delta\omega$	$A_0^2 A_2$
P_{0+2}	$2\omega_0 + \Delta\omega$	-0	$\omega_0 + \Delta\omega$	$A_0^2 A_2$
P_{0-1}	$\Delta\omega$	$+0$	$\omega_0 + \Delta\omega$	$A_0^2 A_1^*$
P_{0-1}	$\Delta\omega$	-0	$-\omega_0 + \Delta\omega$	$A_0^2 A_1^*$
P_{0-2}	$-\Delta\omega$	$+0$	$\omega_0 - \Delta\omega$	$A_0^2 A_2^*$
P_{0-2}	$-\Delta\omega$	-0	$-\omega_0 - \Delta\omega$	$A_0^2 A_2^*$

where $L_0 = \hat{L}(\omega_0, k_0)$, $L_- = \hat{L}(\omega_1, k_1)$, and $L_+ = \hat{L}(\omega_2, k_2)$. The first equation is the dispersion relation for the pump wave, which can solved explicitly for k_0:

$$k_0^2 = \frac{\omega_0^2 - 1 + 3A_0^2/8}{1 - A_0^2/(2 - 8\omega_0^2)} \tag{5.58}$$

The equations for the sidebands can be written in matrix form:

$$\begin{pmatrix} L_- - A_0^2 M_-/4 & -A_0^2 M/4 \\ -A_0^2 M/4 & L_+ - A_0^2 M_+/4 \end{pmatrix} \begin{pmatrix} A_- \\ A_+ \end{pmatrix} = 0 \tag{5.59}$$

where

$$M_\pm = \frac{\Delta k^2}{\Delta\omega^2 - 1} + \frac{(2k_0 \pm \Delta k)^2}{(2\omega_0 \pm \Delta\omega)^2 - 1} - 3 \tag{5.60}$$

$$M = \frac{\Delta k^2}{\Delta\omega^2 - 1} + \frac{2k_0^2}{4\omega_0^2 - 1} - \frac{3}{2} \tag{5.61}$$

The dispersion relation is found by setting the determinant to zero and dropping terms fourth order in A_0:

$$\left(\frac{M_+}{L_+} + \frac{M_-}{L_-}\right)\frac{A_0^2}{4} = 1 \tag{5.62}$$

The ratio of the sideband amplitudes is

$$\frac{A_-}{A_+} = \frac{A_0^2 M/4}{L_- - A_0^2 M_-/4} = \frac{L_+ - A_0^2 M_+/4}{A_0^2 M/4} \tag{5.63}$$

5.9 Solution At Resonance

Consider the case where $\Delta\omega \to 1$. The dispersion relation in either the single or multiple resonance case becomes

$$(\omega_0^2 - k_0^2 - \Delta k^2)\Delta k^2 = 0 \tag{5.64}$$

which implies

$$\Delta k = \left\{ \pm 0, \pm \sqrt{\omega_0^2 - k_0^2} \right\} \tag{5.65}$$

Also, the ratio of the sideband amplitudes becomes

$$\frac{A_+}{A_-} = -1 \tag{5.66}$$

So that the two wave solution is never valid in this limit.

Note also that Equation 5.19 implies that the amplitude of the density perturbation at $\Delta\omega$ diverges in this limit if Δk is nonzero.

Chapter 6

Unbounded Plasma

6.1 Transparency

From the point of view of classical electrodynamics, the transparency or opacity of a medium is related to the magnitude and phasing of the currents driven within it by electromagnetic waves. In one dimension, electromagnetic radiation is described by the wave equation

$$(\partial_{xx} - \partial_{tt})A = -j \tag{6.1}$$

where A is some transverse component of the vector potential and j is the corresponding component of current density. By rewriting the wave equation in frequency space and requiring real wavenumbers, one obtains the inequality

$$\omega^2 > -\frac{\hat{j}}{\hat{A}} \tag{6.2}$$

where the circumflex denotes a Fourier-transformed quantity. Transforming the non-relativistic current density

$$j = -(1+n)A \tag{6.3}$$

and inserting the result into equation 6.2 gives

$$\omega^2 > 1 + \frac{\hat{n} * \hat{A}}{2\pi \hat{A}} \tag{6.4}$$

where the asterisk denotes convolution. This becomes an algebraic relation when the vector potential and density perturbation can be represented as

$$A = \frac{1}{2} \sum_i A_i e^{i(\omega_i t - k_i x)} + cc \tag{6.5}$$

and

$$n = \frac{1}{2} \sum_i n_i e^{i(\Delta\omega_i t - \Delta k_i x)} + cc \tag{6.6}$$

Then, the propagation condition for a particular mode with frequency ω_- and wavenumber k_- is

$$\omega_-^2 > 1 + \frac{1}{2} \sum_{(i,j) \in S} \frac{n_i^* A_j}{A_-} \tag{6.7}$$

where A_- is the amplitude of the mode with frequency ω_-, and S refers to the set of unordered pairs (i, j) which satisfy the conditions $\Delta\omega_i = \omega_j - \omega_-$ and $\Delta k_i = k_j - k_-$. In other words, the pump waves A_j drive currents in the plasma waves n_i at the frequency ω_-. If the phasing between the various waves is chosen correctly, the sum in equation (6.7) could be negative. In this case the inequality is satisfied for a range of frequencies with $\omega_- < 1$ and anomalous transparency occurs for those frequencies. If the sum is positive, the inequality is *not* satisfied for a range of frequencies with $\omega_- > 1$ and anomalous opacity occurs for those frequencies.

It is important to note that from the point of view of EIT, what is desired is that the wave with frequency ω_- should propagate regardless of its own intensity. It is evident from the inequality 6.7 that this will only be the case if each of

the density perturbations n_i contain a factor A_-. In other words, the density perturbation must be driven by the anomalously propagating mode.

6.1.1 Two Wave Transparency

The two wave solution of equation 5.20 contains nonlinearities which enable waves to propagate which would normally be cutoff. The dispersion relation 5.50 can be rewritten

$$k_-^2 = \omega_-^2 - 1 + \frac{j(A_0, \Delta\omega, \Delta k)}{A_-} \tag{6.8}$$

where $\omega_- = \omega_0 - \Delta\omega$ is the Stokes frequency, $k_- = k_0 - \Delta k$ is the Stokes wavenumber, and

$$j(A_0, \Delta\omega, \Delta k) = -\frac{A_0^2 A_-}{4} \frac{\Delta k^2}{\Delta\omega^2 - 1} \tag{6.9}$$

is the amplitude of the nonlinear current *at* the Stokes frequency. The transparency condition is then

$$\omega_-^2 > 1 - \frac{j(A_0, \Delta\omega, \Delta k)}{A_-} \tag{6.10}$$

Equation 6.9 suggests that the nonlinear current will be large where $\Delta\omega \approx 1$, and will change sign where $\Delta\omega = 1$. This suggests that anomalous transparency will occur for frequencies in an interval bounded on one side by $\Delta\omega = 1$. Anomalous transparency might also occur for frequencies bounded above by $\omega_- = 1$ since in the neighborhood of the natural cutoff frequency even a small nonlinear current might be enough to allow the Stokes wave to propagate.

Consider the region near $\Delta\omega = 1$. Expanding the expression 5.51 in terms of a small parameter $\delta\omega$ where $\Delta\omega = 1 + \delta\omega$ gives

$$\Delta k = \frac{8\delta\omega}{A_0^2} k_0 \pm \sqrt{\frac{8\delta\omega}{A_0^2}(1 - 2\omega_0)} \tag{6.11}$$

Assuming $\omega_0 > 1$, this implies that Δk is real when $\Delta\omega < 1$. In other words, the Stokes wave will propagate when the plasma wave is driven at a frequency slightly below resonance.

Now consider the region near $\omega_- = 1$. Expanding 5.51 in terms of a small parameter $\delta\omega$ where $\omega_- = 1 - \delta\omega$ gives

$$\Delta k = k_0 \pm \sqrt{\frac{A_0^2}{4}\frac{\omega_0^2 - 1}{\omega_0(2-\omega_0)} - 2\delta\omega} \tag{6.12}$$

The Stokes wave will propagate when

$$\delta\omega < \frac{A_0^2}{8}\frac{\omega_0^2 - 1}{\omega_0(2-\omega_0)} \tag{6.13}$$

Anomalous transparency corresponds to the case where $\delta\omega$ is positive. In this case, the inequality could only be satisfied if

$$1 < \omega_0 < 2 \tag{6.14}$$

In other words, if the pump wave frequency is between the plasma frequency and its second harmonic, a region of anomalous transparency will occur for Stokes frequencies just below the plasma frequency.

In figure 6.1 we plot the two branches of the dispersion relation for the Stokes wave in the case where $\omega_0 = 1.75$, and $A_0 = 0.3$. As predicted, transparency is induced for frequencies such that $\Delta\omega$ is just under one, or for frequencies such that the Stokes frequency is just under one. The width of the stopband between these two regions is inversely related to the pump intensity.

Plotted in figure 6.2 is the dispersion relation due to Harris [3]. This differs from the dispersion relation plotted in figure 6.1 because of the linear approximation used.

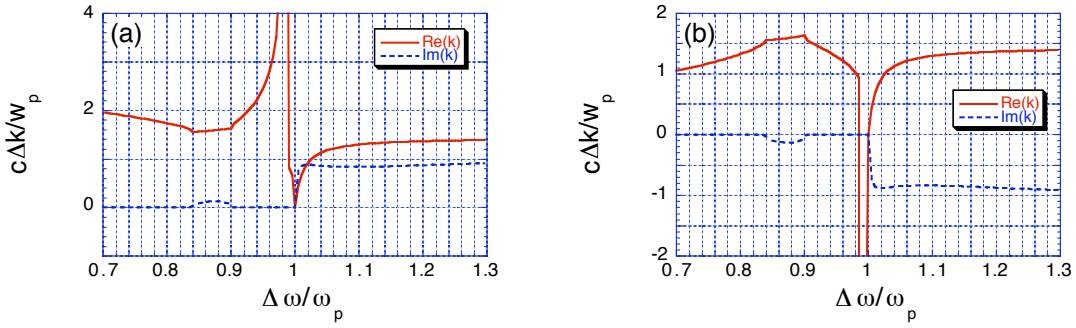

Figure 6.1: Two wave dispersion relation with $A_0 = 0.3$ and $\omega_0 = 1.75$ (a) Positive Branch (b) Negative Branch

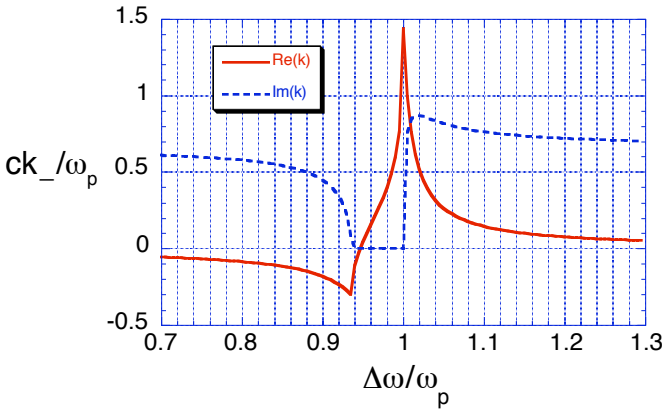

Figure 6.2: Dispersion relation of S.E. Harris

It is a general feature of a harmonic oscillator that when driven slower than the resonant frequency the oscillation is in phase with the driver while when driven faster than the resonant frequency the oscillation is π out of phase with the driver. This is the physical basis of two wave transparency. The harmonic oscillator is the plasma wave and the driver is the ponderomotive force applied at the frequency $\Delta\omega$ by the pump wave and the Stokes wave. When $\Delta\omega$ is less than unity, the plasma wave is in phase with the driver and the nonlinear current is in phase with the vector potential thus reducing the net current and lowering the cutoff frequency.

Note that the nonlinear current at the Stokes frequency is *not* driven by the Stokes wave. It is driven by the pump wave acting *within* the density perturbation. In other words, the tempting thought that a density perturbation driven by any means whatsoever will render the plasma transparent is wrong. The pump wave is required.

An expression for the pump intensity required to make the Stokes wave propagate given a particular ω_0 and $\Delta\omega$ can be derived by requiring the discriminant of equation 5.51 to be positive. This results in

$$A_0^2 > 4(\Delta\omega^2 - 1)\left(\frac{1-\omega_-^2}{\omega_-^2 - \omega_0^2}\right) \tag{6.15}$$

which is valid provided $\Delta\omega^2 < 1$ and $\omega_0^2 > \omega_-^2$. If either condition is violated the inequality must be reversed. This implies that in such cases the nonlinearity *raises* the cutoff frequency. Since it was assumed previously that A_0 is real, a requirement that A_0^2 be less than a negative number means that transparency is not possible. Figure 6.3 shows contours of the minimum A_0 required to make the Stokes wave propagate versus $\Delta\omega$ and ω_0. The conditions $\Delta\omega^2 < 1$ and $\omega_0^2 > \omega_-^2$

are met throughout the domain of the graph.

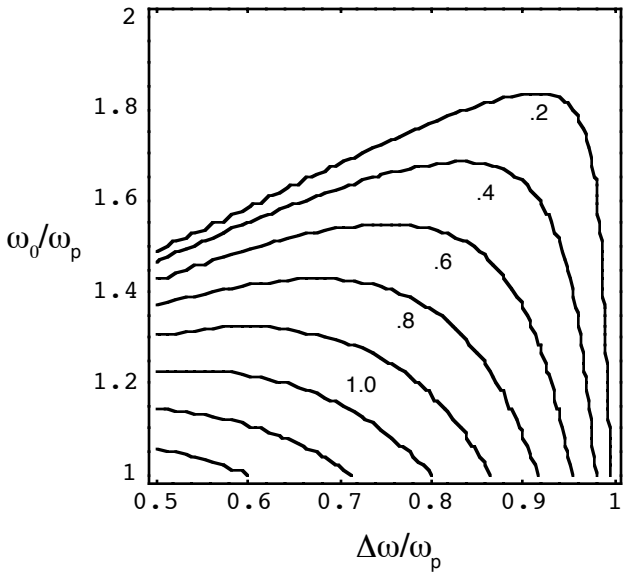

Figure 6.3: Contours of minimum A_0

6.1.2 Three Wave Transparency

The description of the two wave effect in the last section is valid only if the three wave dispersion relation implies $A_+ \ll A_-$ over the frequency range of interest. We verify this by evaluating the non-relativistic version of the dispersion relation 5.46 using a numerical root solver and computing the ratio A_+/A_- at each point on the dispersion curve. The results are plotted in figure 6.4 which shows the dispersion relation along with the natural logarithm of the anti-Stokes to Stokes ratio. Note that the three wave dispersion relation has four solutions whereas the two wave dispersion relation had only two.

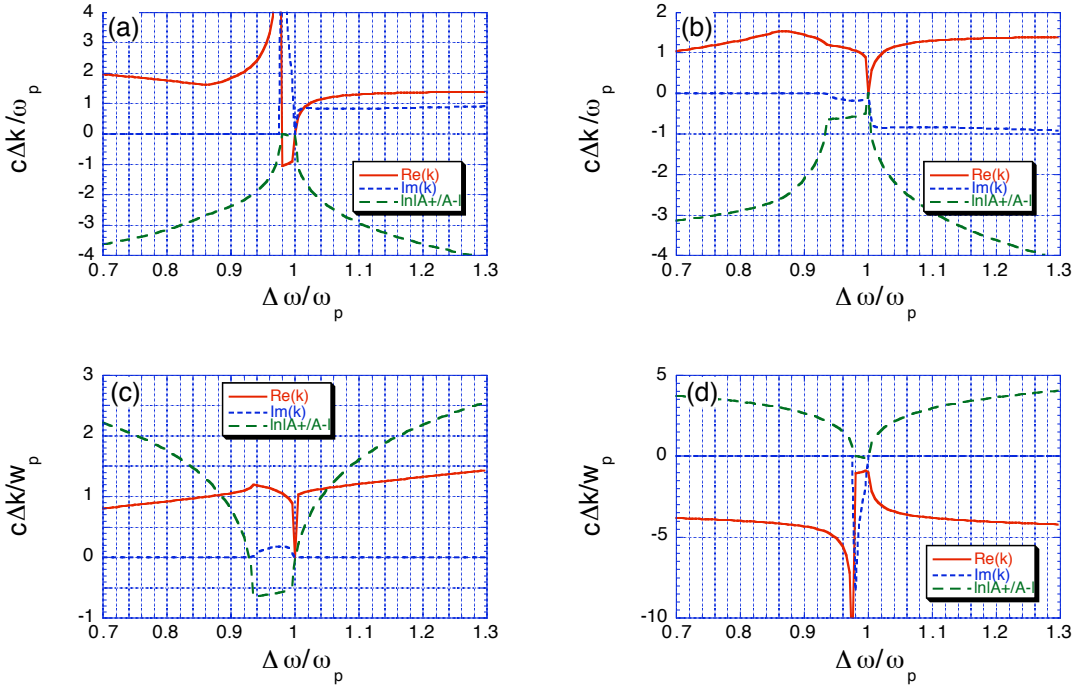

Figure 6.4: Non-relativistic three wave dispersion relation with $A_0 = 0.3$ and $\omega_0 = 1.75$ (a,b) Stokes dominated branches (c,d) anti-Stokes dominated branches

The dispersion curves shown in figure 6.4(a) and 6.4(b) have the desired feature that $A_+ \ll A_-$ except near the resonance at $\Delta\omega = 1$. Thus, the curves look similar to the corresponding two wave solutions except near the resonance where an additional stopband appears just below $\Delta\omega = 1$. Also, the small stopbands which appeared in the region $\Delta\omega < 1$ in the two wave case do not appear in the three wave case. This is not a large effect. A small increase in pump intensity would have made these stopbands disappear from the two wave dispersion relation also. Conversely, a small decrease in pump intensity would make them appear in the three wave dispersion relation.

The dispersion curves shown in figure 6.4(c) and 6.4(d) are dominated by anti-Stokes. They are distinguished from the Stokes-dominated curves in that anomolous transparency occurs on both sides of the resonance. The density perturbation therefore has the same phase with respect to A_0 and A_- on both sides of the resonance. This is possible because the phase of A_+/A_- differs by π from one side of the resonance to the other. Thus, the shift in the phase of n caused by changing the frequency of the driver is cancelled by the shift caused by changing the phase of the driver.

6.1.3 Relativistic Effects

In some cases it might be necessary to consider the relativistic correction to the current density, or the effects of the density perturbations at $2\omega_0$, $2\omega_0 + \Delta\omega$, and $2\omega_0 - \Delta\omega$. These considerations are accounted for by the relativistic multi-resonance dispersion relation 5.62, which is plotted in figure 6.5 for the parameters considered above. For the most part, the relativistic curves look the same as

the non-relativistic curves. The biggest effect is the change in the anti-Stokes amplitude in figure 6.5(c).

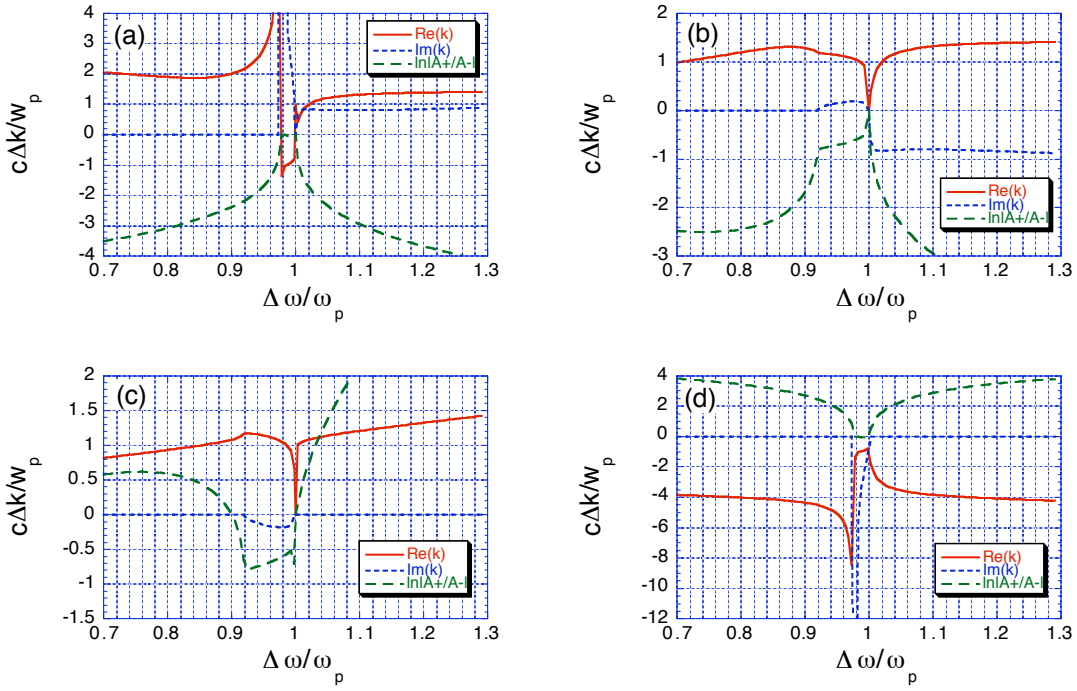

Figure 6.5: Relativistic multi-resonance dispersion relation with $A_0 = 0.3$ and $\omega_0 = 1.75$ (a,b) Stokes dominated branches (c,d) anti-Stokes dominated branches

Naturally, for some other set of parameters relativistic effects might be more important. An example of this is discussed below in the section on single wave transparency.

6.1.4 Simulation of Transparency

Since the dispersion relations of chapter 5 are approximate, it is useful to verify the conclusions drawn from them via computer simulation. For this purpose we use a one-dimensional, fully electromagnetic, fully relativistic particle-in-cell (PIC) code. The code, called "EZPIC", was written by the author and is fully documented [36]. It is based on the well-tested algorithm of WAVE [37] and has been benchmarked against that code.

Fundamentally, a PIC code solves an initial value problem on a finite interval. By contrast, a dispersion relation is a description of a system infinite both in space and time. Spatially, this dilemma can be resolved by noting that whenever $k_0/\Delta k$ is a rational number, all quantities are periodic in x. In this case, the infinite system can be modelled by applying periodic boundary conditions to a finite simulation box of length

$$L = \frac{2\pi n}{k_0} \tag{6.16}$$

where

$$\frac{k_0}{\Delta k} = \frac{n}{m} \tag{6.17}$$

and n and m are integers. Temporally, the dilemma cannot be resolved as easily since once n and m are chosen, the ratio $\omega_0/\Delta\omega$ is determined. It is unlikely that this ratio will be close to any rational number such that one period of the time series predicted by the dispersion relation can be simulated quickly. Even if this could be done, simulations contain inherent noise and damping effects which inevitably lead to aperiodic outcomes. We therefore attempt only to reproduce a fraction of the temporal period predicted by the dispersion relation. This is done by initializing the simulation fields and particle states to be consistent with the

dispersion relation, allowing the system to evolve, and comparing the outcome with the analytical prediction.

The initial conditions used for the simulation are described by table 6.1. The vector potential is given by

$$A_y = \frac{A_0}{2}e^{i\psi_0} + \frac{A_-}{2}e^{i\psi_-} + \frac{A_+}{2}e^{i\psi_+} + cc \tag{6.18}$$

where $\psi_0 = \omega_0 t - k_0 x$, $\psi_- = (\omega_0 - \Delta\omega)t - (k_0 - \Delta k)x$, and $\psi_+ = (\omega_0 + \Delta\omega)t - (k_0 + \Delta k)x$. The parameters A_0, A_-, and ω_0 are prescribed. The anti-Stokes amplitude A_+ is then obtained from 5.63. The wavenumber k_0 is obtained from the relativistic pump wave dispersion relation 5.58. The wavenumber Δk is chosen such that $k_0/\Delta k = 3/2$. The frequency $\Delta\omega$ is then obtained from the multi-resonance dispersion relation 5.62. The initial density perturbation is obtained from equation 5.19 which gives

$$n_1 = \frac{n}{2}e^{i\psi} + \frac{n_0}{2}e^{i2\psi_0} + \frac{n_-}{2}e^{i(\psi_0+\psi_-)} + \frac{n_+}{2}e^{i(\psi_0+\psi_+)} + cc \tag{6.19}$$

where $\psi = \Delta\omega t - \Delta k x$ and

$$n_0 = \frac{k_0^2}{4\omega_0^2 - 1}A_0^2 \tag{6.20}$$

$$n = \frac{\Delta k^2}{2(\Delta\omega^2 - 1)}A_0(A_- + A_+) \tag{6.21}$$

$$n_- = \frac{(2k_0 - \Delta k)^2}{2[(\Delta\omega - 2\omega_0)^2 - 1]}A_0 A_- \tag{6.22}$$

$$n_+ = \frac{(2k_0 + \Delta k)^2}{2[(\Delta\omega + 2\omega_0)^2 - 1]}A_0 A_+ \tag{6.23}$$

The density perturbation determines not only the initial particle positions, but also the initial particle momenta. From the continuity equation, the axial velocity

Table 6.1: Initial Conditions

Quantity	Value
A_0	0.2
A_-	0.02
A_+	0.0028
n	-0.18
n_0	0.0074
n_-	0.00037
n_+	0.00019
ω_0	1.75
k_0	1.44
$\Delta\omega$	0.97
Δk	2.16
v_{th}	0.1

of a fluid element is

$$v_x = \frac{\omega_0}{k_0} n_0 e^{i2\psi_0} + \frac{\Delta\omega}{\Delta k} n e^{i\psi} + \frac{\Delta\omega + 2\omega_0}{\Delta k + 2k_0} n_+ e^{i(\psi_0+\psi_+)} + \frac{\Delta\omega - 2\omega_0}{\Delta k - 2k_0} n_- e^{i(\psi_0+\psi_-)} \quad (6.24)$$

Also known is the transverse momentum:

$$p_y = A_y \quad (6.25)$$

The axial momentum can be expressed in terms of v_x and p_y via the relativistic relation $\mathbf{p} = \gamma\mathbf{v}$:

$$p_x^2 = \left(1 - v_x^2 - \frac{1 - v_x^2}{1 + p_y^2} p_y^2\right)^{-1} v_x^2 \quad (6.26)$$

The momentum of a particle is the fluid momentum plus the thermal velocity, v_{th}. The thermal velocity cannot be zero in a PIC code because of the grid instability. In fact, v_{th} must be large enough so that a typical particle traverses a grid cell within one plasma period.

Table 6.2: Simulation Parameters

Quantity	Value
Time Step	0.0561
Steps	1024
Cell Size	0.0682
Cells	128
Particles per Cell	500
Ion Mass	∞

Table 6.2 details the parameters characterizing computational aspects of the simulation. The time step is chosen so that an integral number of periods of the pump wave are executed during the simulation. The cell size is chosen so that exactly one spatial period of the infinite system fits in the simulation box. The number of particles per cell is large to minimize noise. The ions are modelled as a fixed, uniform background of neutralizing charge.

To compare the simulation results with the analytical results it is most convenient to examine $\hat{A}_y(\omega, k)$. This is obtained by performing a fast-fourier transform (FFT) of $A_y(x, t)$ which is computed naturally by the simulation. The result is shown in figure 6.6. As expected, the spectrum contains three discrete features corresponding to the pump wave, the Stokes wave, and the anti-Stokes wave. The Stokes wave lies within the stopband predicted by linear theory, but as predicted, propagates nevertheless. An unexpected feature appears at the Stokes wavenumber but at a frequency of about 1.2. Also, the fact that the simulation time is not an integral multiple of $2\pi/\Delta\omega$ causes the FFT to produce more bandwidth than is really present.

Figure 6.7 shows the density perturbation as computed during the simulation.

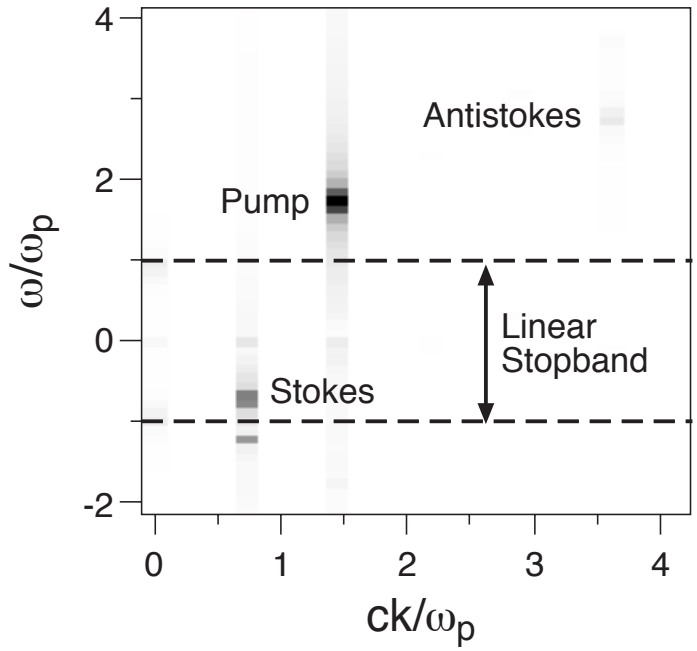

Figure 6.6: Intensity plot of $\hat{A}_y(\omega, k)$ as computed via PIC simulation. Dark areas correspond to large amplitudes.

The density perturbation is of interest since the analysis required $n_1 = O(A_y^2)$ whereas for the simulation $n_1 = O(A_y)$. Figure 6.7(b) reveals that n_1 contains significant amounts of second harmonic. Here we see a clear example of an effect not accounted for by the analysis.

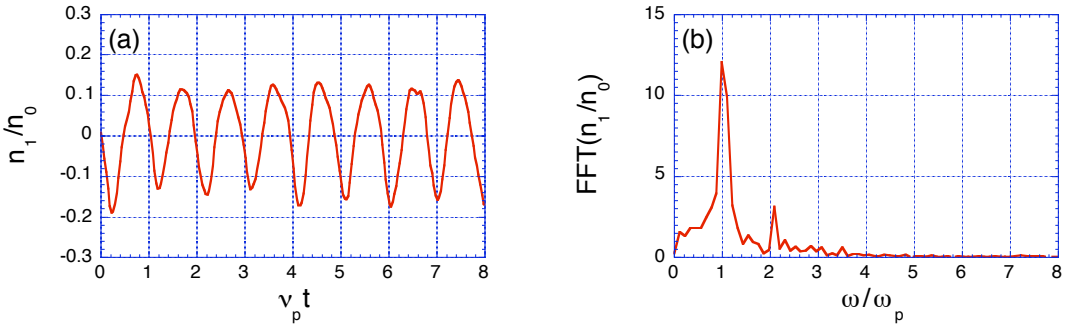

Figure 6.7: Density Perturbation as computed via PIC simulation near the center of the box (a) density time series (b) FFT of the density time series

6.1.5 Single Wave Transparency

If the frequency of the pump wave is $\omega_0 \approx 1/2$, the pump wave alone will strongly couple to the density perturbation at $2\omega_0$. This leads to a nonlinear current at ω_0 given by

$$\frac{A_0^2}{8}\left(\frac{4k_0^2}{4\omega_0^2 - 1} - \frac{3}{2}\right) \tag{6.27}$$

This current could be large if $\omega_0 \approx 1/2$ and if properly phased could render the plasma transparent.

The transparency condition can be expressed explicitly in terms of ω_0 and A_0 using the dispersion relation 5.58:

$$\frac{\omega_0^2 - 1 + 3A_0^2/8}{1 - A_0^2/(2 - 8\omega_0^2)} > 0 \tag{6.28}$$

Suppose $\omega_0 < 1/2$. Then the denominator is negative provided

$$\omega_0^2 > \frac{1}{4} - \frac{A_0^2}{8} \tag{6.29}$$

The numerator is negative also if

$$\omega_0^2 < 1 - \frac{3}{8}A_0^2 \tag{6.30}$$

This is guaranteed immediately since $\omega_0 < 1/2$ and $A_0 < 1$. It follows that there is a passband defined by

$$\sqrt{\frac{1}{4} - \frac{A_0^2}{8}} < \omega_0 < \frac{1}{2} \tag{6.31}$$

which becomes

$$\frac{1}{2} - \frac{A_0^2}{8} < \omega_0 < \frac{1}{2} \tag{6.32}$$

provided A_0 is small. Note that the passband disappears only when $A_0 = 0$. Also, dropping the relativistic term $3A_0^2/8$ from the dispersion relation does not affect the width of the passband unless $A_0 > \sqrt{2}$.

If $\omega_0 > 1/2$ the denominator is positive and transparency occurs when

$$\omega_0^2 > 1 - \frac{3}{8}A_0^2 \tag{6.33}$$

This is a purely relativistic effect. The usual cutoff frequency of one is reduced by about $3A_0^2/16$ due to the fact that some of the laser energy goes into increasing the mass of the particles rather than increasing their velocity.

In the case of single wave transparency at $\omega_0 \approx 1/2$, it is important to consider the size of the density perturbation since the differential equations describing the plasma were only valid if $n_1 = O(A_0^2)$. This is not a problem in the multiple frequency case since the amplitude of the density perturbation at $\Delta\omega$ is linearly related to the sideband amplitudes whose magnitude is arbitrary. In the single frequency case, however, the density perturbation at $2\omega_0$ is near resonance and does not depend linearly on A_0. Let n_0 be the amplitude of the density perturbation at $2\omega_0$. Since there is only the pump wave,

$$n_1 = \frac{n_0}{2} e^{i(2\omega_0 t - 2k_0 x)} + cc \tag{6.34}$$

Using equation 5.19 along with the dispersion relation,

$$n_0 = A_0^2 \frac{\omega_0^2 - 1 + 3A_0^2/8}{4\omega_0^2 - 1 + A_0^2/2} \tag{6.35}$$

Now let $\omega_0 = 1/2 - \delta\omega$. Then

$$n_0 \approx A_0^2 \frac{3A_0^2/8 - 3/4 - \delta\omega}{A_0^2/2 - 4\delta\omega} \tag{6.36}$$

when $\delta\omega \ll 1$. At the low frequency end of the passband $n_0 \to -\infty$ as $\delta\omega \to A_0^2/8$. At the high frequency end of the passband $\delta\omega = 0$ and $n_0 \approx -3/2$ neglecting the relativistic term. If the relativistic term and $\delta\omega$ are small compared with $3/4$, it is clear that n_0 changes monotonically within the interval $0 < \delta\omega < A_0^2/8$ and is therefore never less than $3/2$ in magnitude. Single frequency transparency at $\omega_0 = 1/2$ is therefore likely to be more complex than the analysis presented here suggests. The analysis of the relativistic effect at $\omega_0 \approx 1$, however, suffers from no fundamental difficulty and the description given here is probably accurate.

Figure 6.8(a) shows the single wave dispersion relation for the case $A_0 = .75$. The large value of A_0 is needed to exaggerate the transparency effect so that the

passbands at $\omega_0 = 1/2$ and $\omega_0 = 1$ are visible on the same plot. The passbands occur where the curve is positive.

Figure 6.8(b) shows the amplitude of the density perturbation near the passband at $\omega_0 = 1/2$ for the case $A_0 = 0.3$. As predicted, the density is prohibitively large throughout the passband, which extends from $\omega_0 \approx .489$ to $\omega_0 = 1/2$.

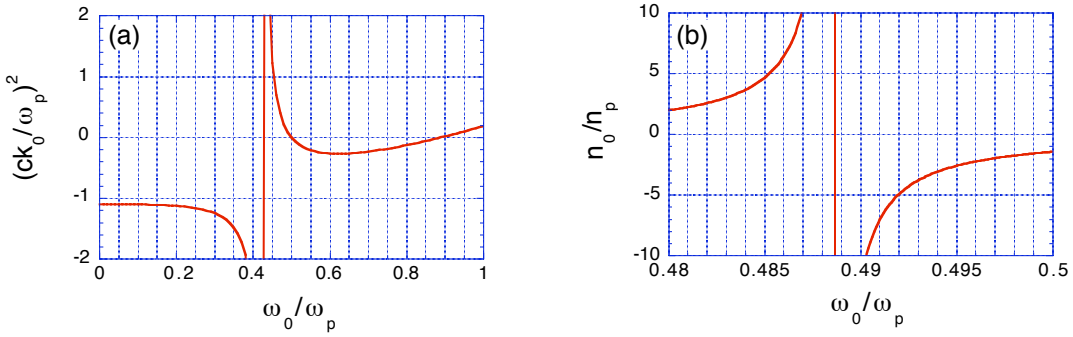

Figure 6.8: Single wave transparency (a) dispersion relation with $A_0 = 0.75$ (b) Density perturbation at $2\omega_0$ with $A_0 = 0.3$

6.2 Stability

In a plasma the Raman instability is the decay of a pump wave with frequency ω_0 into a plasma wave with frequency $\Delta\omega$ and a Stokes wave with frequency $\omega_0 - \Delta\omega$. The ponderomotive force applied by the two electromagnetic waves drives the density perturbation while the density perturbation converts electromagnetic energy with frequency ω_0 into electromagnetic energy with frequency $\omega_0 - \Delta\omega$. It has traditionally been thought that this process cannot occur if $\omega_0 < 2\omega_p$ since

then the two electromagnetic waves would not resonate with the plasma unless the Stokes wave was evanescent. In section 6.1, however, it was shown that in such cases the presence of the density perturbation can modify the opacity of the plasma such that the Stokes wave is able to propagate. The Raman instability might therefore occur even when $\omega_0 < 2\omega_p$.

The analyses of section 6.1 reveal nothing about the stability of the systems considered there. The existence of normal modes with real frequencies and imaginary wavenumbers of either sign demonstrates neither stability nor instability [38]. On the other hand, the existence of normal modes with real wavenumbers and imaginary frequencies of the correct sign does demonstrate that a system is unstable. The dispersion relations of chapter 5 must therefore be re-examined in this context.

6.2.1 Two Wave Instability

Consider again the two-wave dispersion relation 5.50. An explicit solution for $\Delta\omega$ can only be obtained if a second order approximation is made. Let $\Delta\omega = 1 + \delta\omega$. Inserting this into equation 5.50 and dropping terms of order $\delta\omega^3$ and higher results in

$$\Delta\omega = 1 + \frac{-B \pm \sqrt{B^2 - 4AC}}{2A} \tag{6.37}$$

where

$$A = (\omega_0 - 3)^2 - (\Delta k - k_0)^2 - 5 \tag{6.38}$$

$$B = 2[(\omega_0 - 1)^2 - (\Delta k - k_0)^2 - 1] \tag{6.39}$$

$$C = -\Delta k^2 \frac{A_0^2}{4} \tag{6.40}$$

Instability occurs if the discriminant $B^2 - 4AC$ is negative. Assuming A is negative, this occurs when

$$\frac{[(\omega_0 - 1)^2 - (\Delta k - k_0)^2 - 1]^2}{5 + (\Delta k - k_0)^2 - (\omega_0 - 3)^2} < \Delta k^2 \frac{A_0^2}{4} \tag{6.41}$$

If $\Delta k - k_0$ is large it is clear that the inequality can never be satisfied in the case $\omega_0 < 2$. Consider therefore the case where $\Delta k - k_0$ vanishes. Then if $\omega_0 = 2$ instability occurs for any value of A_0 since the numerator vanishes. As ω_0 decreases from this value the pump intensity required for instability increases. A simple expression for the growth rate can be found by taking $\Delta k = k_0$ and $\omega_0 = 2 - \delta\omega$. Inserting these into the expression for the growth rate

$$\gamma \equiv \left| \frac{\sqrt{B^2 - 4AC}}{2A} \right| \tag{6.42}$$

and dropping terms of order $\delta\omega^3$ and higher results in

$$\gamma = \frac{k_0 A_0}{4} \left| 1 + \frac{\delta\omega}{4} - \frac{2\delta\omega^2}{k_0^2 A_0^2} \right| \tag{6.43}$$

If $\delta\omega = O(A_0)$ and $k_0 = O(1)$ the second term is negligible compared with the other two. In this case, the growth rate is

$$\gamma = \frac{k_0 A_0}{4} \left| 1 - \frac{2(\omega_0 - 2)^2}{k_0^2 A_0^2} \right| \tag{6.44}$$

We see that the growth rate increases with A_0 and decreases as ω_0 departs from two.

The four branches of the full dispersion relation 5.50 are plotted in figure 6.9 for $\omega_0 = 1.75$ ($\Rightarrow k_0 \approx 1.44$) and $A_0 = 0.35$. The usual value of $A_0 = 0.3$ is insufficient in this case to cause instability.

Figure 6.9(a) shows the two branches of the dispersion relation for which $\Delta\omega$ is complex. As predicted, the instability occurs where $\Delta k \approx k_0$. The instability

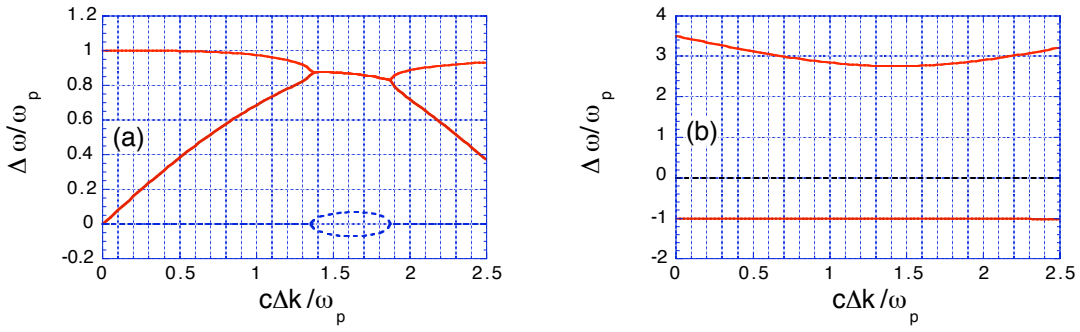

Figure 6.9: Two wave dispersion relation with $A_0 = 0.35$ and $\omega_0 = 1.75$ (a) the two complex branches (solid lines represent the real part while dotted lines represent the imaginary part) (b) the two purely real branches

therefore generates a Stokes wave with a very long wavelength since $k_- = k_0 - \Delta k$. Furthermore, the instability generates a Stokes wave which propagates in both directions since the band of unstable wavenumbers crosses the origin.

Figure 6.9(b) shows the two branches of the dispersion relation for which $\Delta\omega$ is real. The branch with positive $\Delta\omega$ is the one for which the two electromagnetic waves are nearly decoupled.

6.2.2 Three Wave Instability

The conclusions drawn from the two wave dispersion relation must be verified by finding branches of the three wave dispersion relation for which $A_+ << A_-$. Two such branches are shown in figure 6.10. The curves look nearly identicle to figure 6.9(a) near the region of instability. Hence, the two wave analysis is valid.

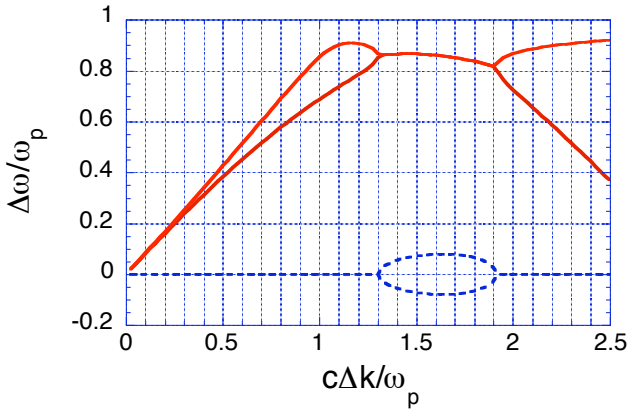

Figure 6.10: Non-relativistic three wave dispersion relation with $A_0 = 0.35$ and $\omega_0 = 1.75$. Solid lines represent the real part while dotted lines represent the imaginary part. There are four purely real branches not shown.

6.2.3 Multi-Resonance Analysis

Analysis of the relativistic multi-resonance dispersion relation reveals that when $k_0 \approx \Delta k$ an instability occurs not only for $\Delta\omega \approx 1$ but also for $2\omega_0 - \Delta\omega \approx 1$. This is due to the longitudinal electron oscillation induced by the second harmonic of the pump wave and the Stokes wave. Figure 6.11 shows the two branches dominated by this process along with the two branches corresponding to the single resonance case ($\Delta\omega \approx 1$). The unstable mode with $\Delta k \approx 0$ corresponds to the relativistic modulational instability [39, 40].

6.2.4 Simulation of Instability

The analysis of stability can be verified using PIC simulations in a manner similar to the way the analysis of transparency was verified. Once again, by using

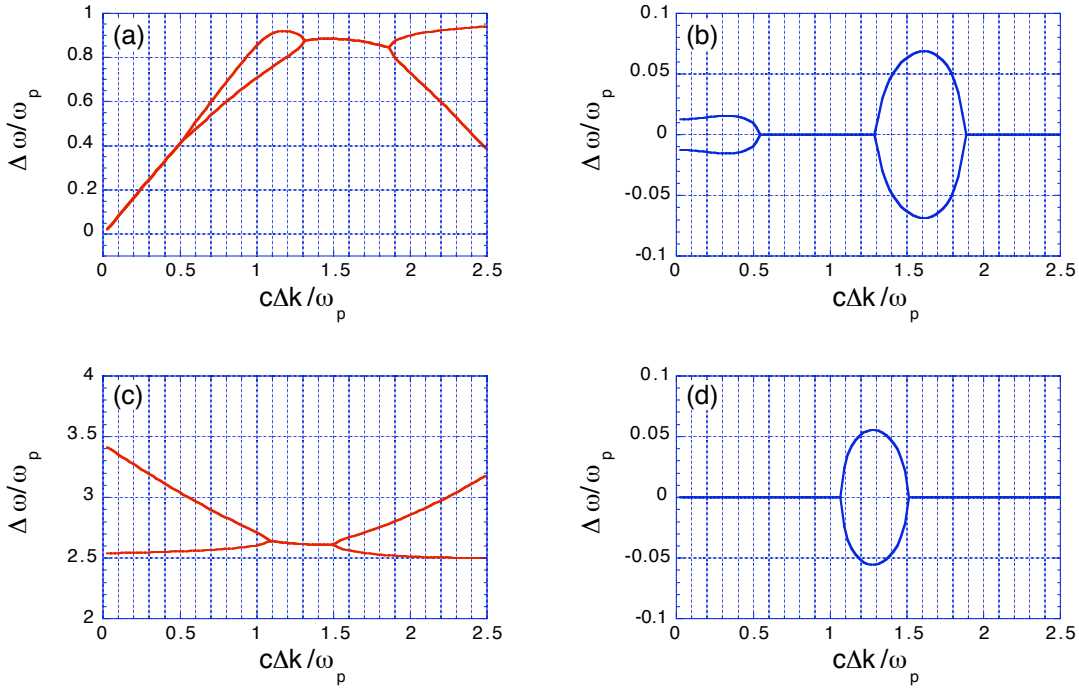

Figure 6.11: Relativistic multi-resonance three wave dispersion relation with $A_0 = 0.3$ and $\omega_0 = 1.75$ (a) real part of branches affected by the resonance at $\Delta\omega = 1$ (b) imaginary part of branches affected by the resonance at $\Delta\omega = 1$ (c) real part of branches affected by the resonance at $2\omega_0 - \Delta\omega = 1$ (d) imaginary part of branches affected by the resonance at $2\omega_0 - \Delta\omega = 1$. There are six purely real branches not shown.

Table 6.3: Initial Conditions

Quantity	Value
A_0	0.4
A_-	0.01
A_+	$0.0002 - 0.001i$
n	$-0.009 + 0.01i$
n_0	0.03
n_-	$0.0007 - 0.00008i$
n_+	$0.00005 - 0.0002i$
ω_0	1.75
k_0	1.45
$\Delta\omega$	$0.89 - 0.12i$
Δk	1.45
v_{th}	0.1

periodic boundary conditions and initial conditions consistent with the multi-resonance dispersion relation a portion of the analytically predicted space-time field structure can be reproduced. Unlike the simulation of transparency, a simulation of instability can be consistent with the dispersion relation only for a short period of time while the density perturbation remains small. As the density perturbation grows, higher order nonlinear effects take over and irreversible processes are likely to dominate.

The initial conditions for the simulation of instability are shown in table 6.3. The large value of A_0 is needed to overcome kinetic effects which tend to reduce the growth rate. The initial value of A_- is chosen such that the density perturbation starts out very small. We choose to model the case where $k_0 = \Delta k$. The relativistic multi-resonance dispersion relation then predicts a growth rate of $\gamma = 0.12\omega_p$.

Table 6.4: Simulation Parameters

Quantity	Value
Time Step	0.1
Steps	512
Cell Size	0.1352
Cells	32
Particles per Cell	1000
Ion Mass	∞

Table 6.4 details the computational aspects of the simulation. As before, the spatial parameters are chosen such that one period of the infinite system described by the dispersion relation fits in the simulation box. The time step is not critical in this case since pinpoint frequency resolution is not needed. The large number of particles is needed to reduce noise so that an accurate estimate of the growth rate can be made.

Figure 6.12 shows the results of the simulation. Figure 6.12(a) shows the vector potential associated with the Stokes wave. This is obtained by performing an FFT of the whole vector potential vs. time, filtering out the pump frequency, and performing an inverse FFT on the result. The data is taken at a position in the simulation box such that the vector potential is at a crest at $t = 0$. Also shown in the figure is the analytically predicted envelope given by $A(t) = A(0)e^{\gamma t}$ where A is the vector potential after filtering out the pump and γ is the analytically predicted growth rate. For small signals the simulation agrees with the dispersion relation. Note also that the period of the Stokes wave is greater than the plasma period.

Figure 6.12(b) shows the density perturbation vs. time. Superimposed on the

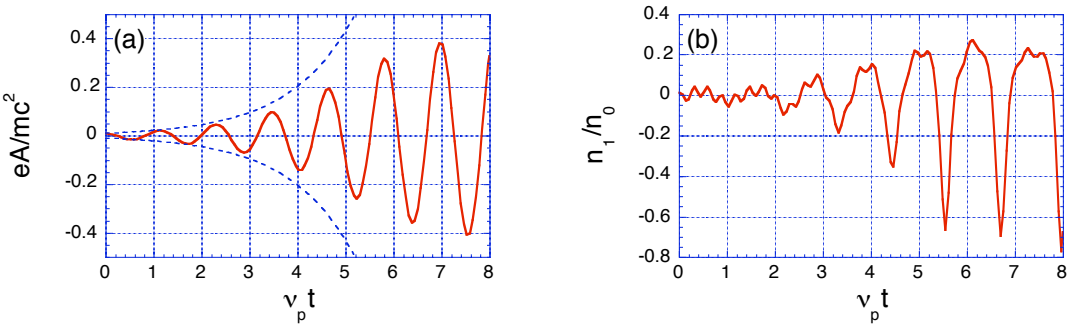

Figure 6.12: PIC simulation of instability (a) vector potential vs. time after filtering out the pump wave. The dotted lines are the analytically predicted envelope. We define $\nu_p = \omega_p/2\pi$. (b) density perturbation vs. time

wave at frequency $\Delta\omega$ is the wave driven by the large pump at $2\omega_0$. Only the wave at $\Delta\omega$ grows, however. As the amplitude approaches unity, wave steepening is clearly observed. Correspondingly, the instability begins to saturate.

Chapter 7

Bounded Plasma

Any experiment involving electromagnetically induced transparency in a plasma must be described in terms of the transmission of an electromagnetic pulse through a finite slab of plasma. The simplest such description would be an equation of the form

$$A_T(\omega) = H(\omega)A_I(\omega) \tag{7.1}$$

where A_T is the spectrum of the transmitted pulse, A_I is the spectrum of the incident pulse, and H is a transfer function with the property

$$H(\omega_-) = \begin{cases} 1 & \text{if pump present} \\ 0 & \text{if pump absent} \end{cases} \tag{7.2}$$

where ω_- is some frequency below the usual cutoff frequency and the "pump" refers to one or more intense waves with frequencies above the cutoff frequency. It is not necessarily true that the transfer function will have this property whenever the dispersion relation gives

$$\begin{aligned} \Im\{k(\omega_-)\} &= 0 \quad \text{if pump present} \\ \Im\{k(\omega_-)\} &\neq 0 \quad \text{if pump absent} \end{aligned} \tag{7.3}$$

To see why the transfer function does not necessarily correspond to the dispersion relation, consider a pulse containing a Stokes wave, a pump wave, and an anti-Stokes wave injected into a finite plasma. If the amplitudes and frequencies of the three waves are chosen based on a Stokes-dominated branch of the dispersion relation, then it is primarily the beating between the Stokes wave and the pump wave which drives the density perturbation. However, a properly phased density perturbation of sufficient amplitude is required before the Stokes wave can enter the plasma. In other words, there can be no density perturbation without the Stokes wave and there can be no Stokes wave without the density perturbation. In this case, therefore, $H = 0$ regardless of the pump intensity. We will discuss this in more detail later. On the other hand, if the injected pulse is designed based on one of the anti-Stokes dominated branches of the dispersion relation, it is the beating between the anti-Stokes and the pump that drives the density perturbation. Since the pump wave and the anti-Stokes wave require no density perturbation to propagate, they penetrate the plasma immediately, the density perturbation grows, and currents at the Stokes frequency are generated. As will be seen below, these currents generate radiation at the Stokes frequency which can interfere with the injected Stokes wave such that transmission is *apparently* achieved.

The instability of the plasma also contributes to the failure of the transfer function to correspond to the dispersion relation. There are two reasons. First, if an intense pump wave propagates through a non-quiescent plasma, it will generate a Stokes wave at the frequency corresponding to the maximum growth rate of the instability due to the presence of unstable frequencies in the noise spectrum.

Second, the presence of any wave in a finite system will encourage the instability since the spectrum of such a wave is likely to overlap the unstable spectrum.

Before attempting a boundary value analysis, we verify the preceding assertions using EZPIC. To model a finite plasma, boundary conditions are chosen to be consistent with the requirement that no plasma exists outside the simulation box. The boundary conditions do allow for an externally driven current outside the simulation box which can be used to inject waves into the box. Waves injected at the left boundary are described by a vector potential

$$A(x=0,t) = A(0,0) f\left(\frac{t}{t_0}\right) e^{-(t-\tau)^2/\Delta t^2} \sin(\omega t) \tag{7.4}$$

where $f(\xi) = 10\xi^3 - 15\xi^4 + 6\xi^5$. The function f has certain numerically favorable properties. It rises monotonically from zero to one in the interval $0 < \xi < 1$. Boundary conditions and the injection of waves are discussed in detail in the EZPIC documentation.

7.1 Anti-Stokes Dominated Simulations

For the first simulation, which we call "run 1", the incident pulse is designed based on the branch of the three wave dispersion relation shown in figure 6.5(c). This is the anti-Stokes-dominated branch for which all three waves are copropagating. Table 7.1 enumerates the parameters A, ω, Δt, t_0, and τ for the three waves to be injected. The Stokes wave is continuous, while the pump and the anti-Stokes are pulsed. Note also that the anti-Stokes is phased opposite to the pump and the Stokes since we operate above resonance. If induced transparency takes place, a wave at the Stokes frequency modulated by the envelope of the pump

Table 7.1: Injection Parameters for Run 1

Quantity	Pump	Anti-Stokes	Stokes
$A(0,0)$	0.3	-0.1	0.017
ω	1.75	2.85	0.65
Δt	100	100	∞
t_0	50	50	10
τ	200	200	0

Table 7.2: Simulation Parameters for Run 1

Quantity	Value
Time Step	0.1
Steps	4096
Cell Size	0.2
Cells	256
Particles per Cell	500
Ion Mass	∞
Plasma Region	Cells 50-206
Thermal Speed	0.1

should emerge from the plasma. Table 7.2 details the computational aspects of the simulation. Note that a small vacuum region is included on either side of the plasma.

Figure 7.1 shows the main results of the simulation. Figure 7.1(a) shows the pump electric field leaving the right boundary. Figure 7.1(b) shows the spectrum of all waves leaving the right boundary. Figures 7.1(c) and 7.1(d) show the Stokes electric field leaving the right and left boundaries respectively. The decomposition of the electric field into right and left propagating components is discussed in the EZPIC documentation. The pump wave and the Stokes wave are isolated

by applying an appropriate FFT filter. The figure shows that the transmission coefficient for the Stokes wave is roughly proportional to the pump amplitude. The pump *appears* to act as a "soft switch" for radiation at the Stokes frequency.

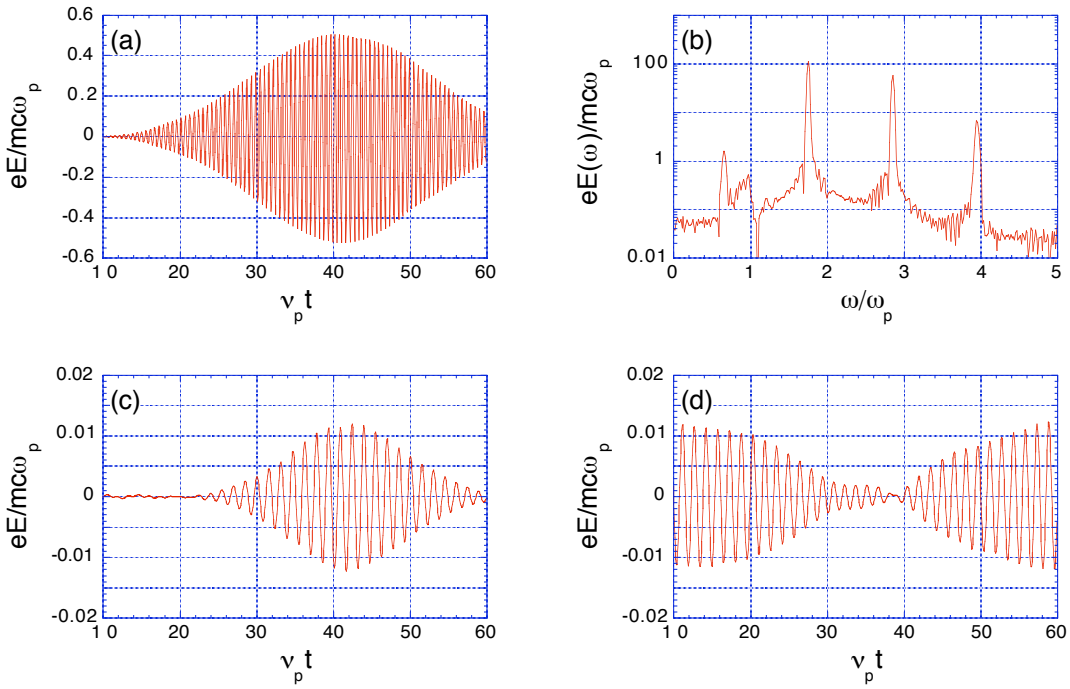

Figure 7.1: Anti-Stokes dominated EIT (a) transmission of pump (b) transmitted spectrum (c) transmission of Stokes (d) reflection of Stokes

Figure 7.1(b) also reveals instability. In addition to the three frequencies that were injected, two new frequencies are clearly generated. The feature at $\omega \approx 1$ is the unstable mode predicted by the dispersion relation. The feature at $\omega \approx 4$ results from the fact that the injected anti-Stokes wave is itself quite intense.

The pump and the anti-Stokes wave therefore constitute a "beatwave" with the ability to cascade into an infinite number of Stokes and anti-Stokes satellites. This realization foreshadows a result to be addressed shortly; namely, that the transmitted spectrum is independent of the injected Stokes wave.

It is useful to plot $A_y(x,t)$ after selecting a particular wave by using an FFT filter. Figure 7.2(a) shows the pump wave, which propagates through the plasma with little trouble. Figure 7.2(b) shows the injected Stokes wave, which is reflected until the pump wave reaches sufficient amplitude. Note the change in phase velocity in the plasma region. Figure 7.2(c) shows the unstable Stokes wave. The phase velocity is nearly infinite. The group velocity is apparently small since very little energy escapes the plasma. The maximum amplitude of the unstable wave is about 0.035.

As mentioned, it might be possible to understand the presence of the Stokes frequency in the transmitted spectrum in terms of cascading. Cascading is the generation of a comb of Stokes and anti-Stokes satellites when a resonant two-frequency "beatwave" is propagated in a plasma. Traditionally, one might have thought that cascading into Stokes frequencies cannot extend below the plasma frequency. However, given the results presented in this dissertation it is clear that such conclusions must be reconsidered. To determine the importance of cascading, run 1 is repeated without injecting the Stokes wave. The results are shown in Figure 7.3. We see that the forward Stokes wave is nearly indentical to the "transmitted" Stokes wave shown in figure 7.1. Furthermore, a mirror image of the forward Stokes wave is generated in the backward direction. By contrast, the anti-Stokes satellite at $4\omega_p$ propagates only in the forward direction because of

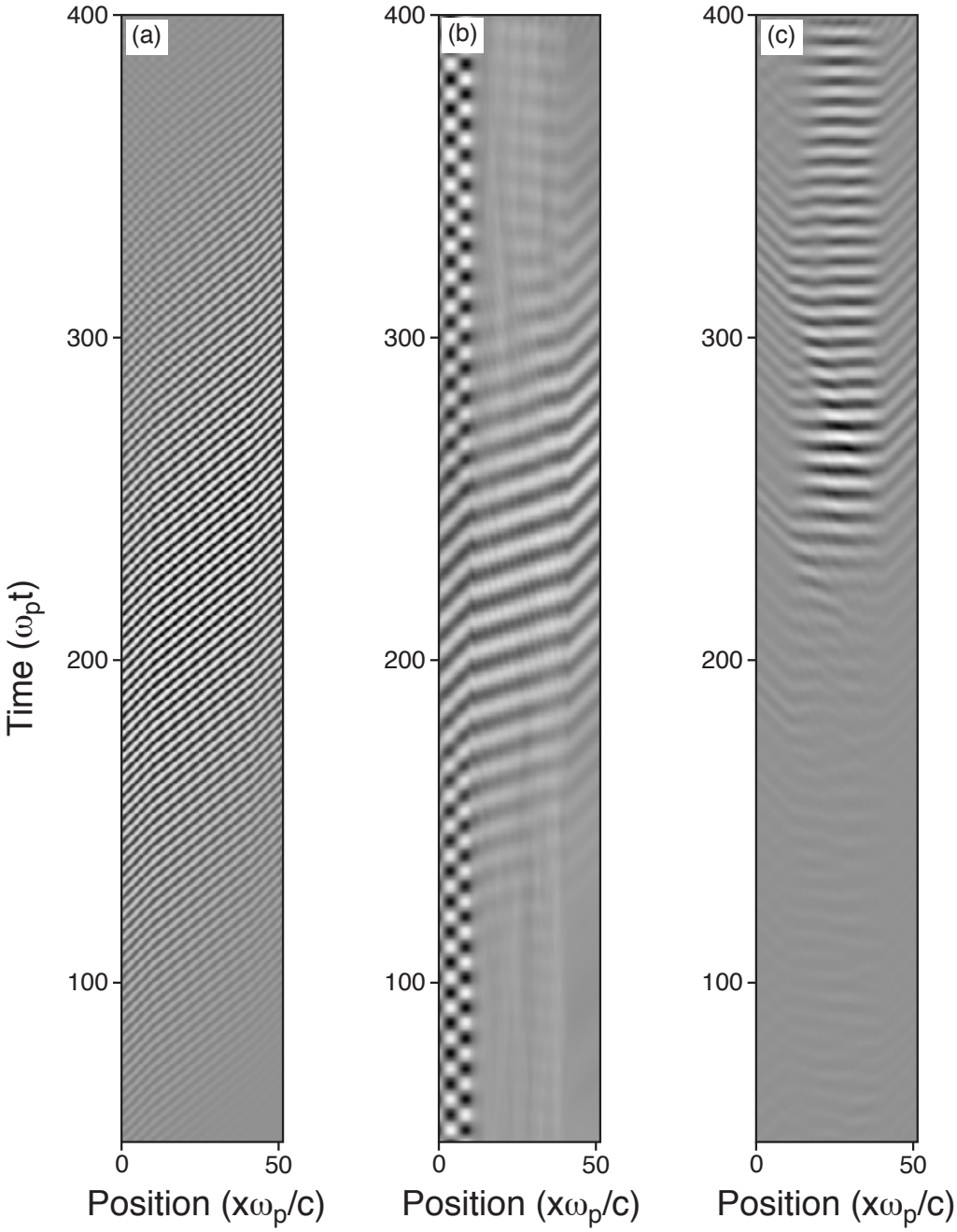

Figure 7.2: Intensity plots of $\hat{F}A_y(x,t)$ where $\hat{F}$ is a filter (a) pump wave (b) injected Stokes wave (c) Stokes wave due to instability. The greyscale used for (a) is different than the one used for (b) and (c).

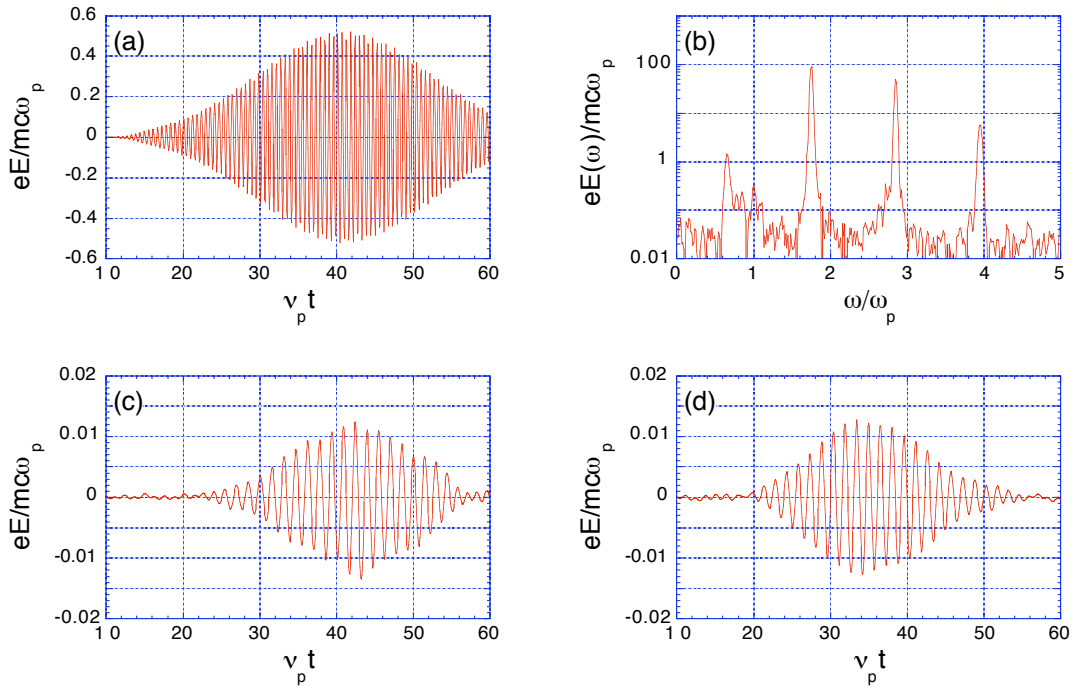

Figure 7.3: Stokes radiation generated by "cascading" (a) transmission of pump (b) transmitted spectrum (c) forward Stokes (d) backward Stokes. This simulation was done after all the others, and featured an improved algorithm to reduce noise.

k-matching considerations. These facts will be discussed in an analytical context later.

Evidently, the process of EIT in the anti-Stokes dominated regime can be understood as follows. First, the injected Stokes wave, or "probe wave", is entirely reflected. Next, the pump and the anti-Stokes *generate* a Stokes wave which propagates in both directions. If the phasing is chosen correctly, the backward propagating Stokes wave will destructively interfere with the reflected probe wave. The transmitted and reflected waveforms then leave the impression that the probe beam was transmitted. However, this is not equivalent to true transmission of the probe beam since for a given A_0 and A_+, the illusion breaks down for any A_- other than that implied by the Raman dispersion relation. Thus, the process cannot truly be called EIT since it does not meet the requirement that the probe wave should be transmitted regardless of its own intensity. That this would be the case could have been predicted from equation 6.7, which reveals that the transparency condition depends upon A_- unless the density perturbation, n, contains A_- as a factor. In other words, the plasma wave must be driven by the Stokes wave.

Finally, for completeness, run 1 is repeated without any anti-Stokes. The results are shown in figure 7.4. Frequencies below the cutoff frequency do emerge from the plasma, but this is clearly not EIT. Figure 7.4(d) shows that the Stokes wave is entirely reflected regardless of the pump amplitude. The low frequency wave which does emerge from the plasma has a higher frequency than the Stokes wave and is generated in the plasma via instability.

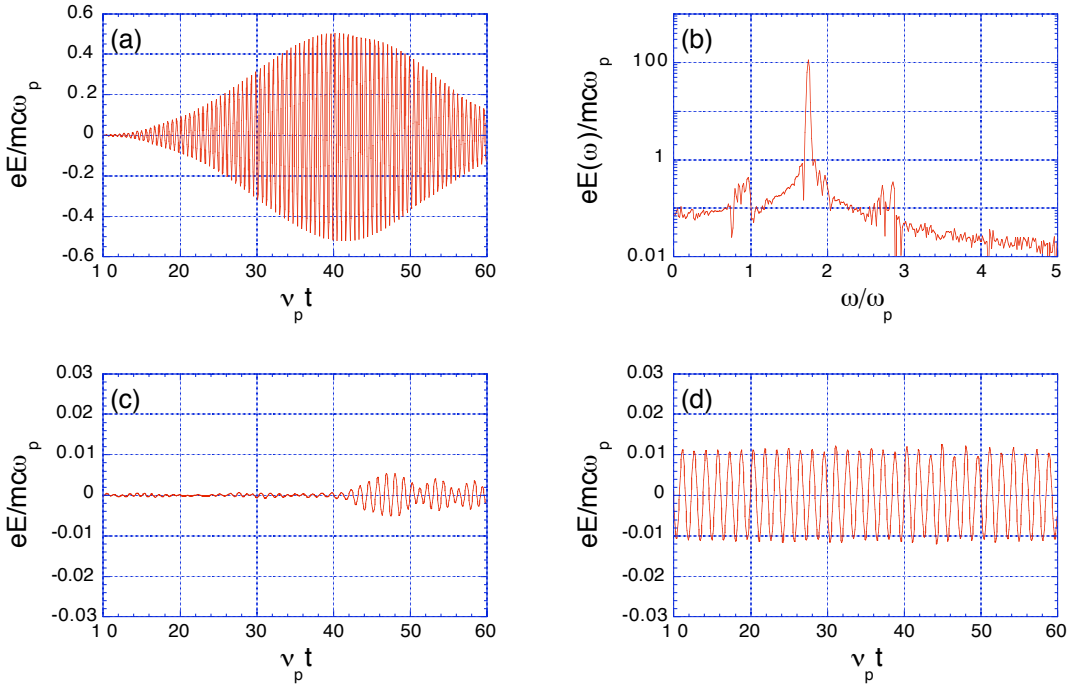

Figure 7.4: Transmission and reflection without the anti-Stokes (a) transmission of pump (b) transmitted spectrum (c) transmission of the unstable frequencies (d) reflection of Stokes

Table 7.3: Injection Parameters for Run 2

Quantity	Pump	Anti-Stokes	Stokes
$A(0,0)$	0.3	0.0	0.03
ω	1.75	-	0.85
Δt	100	-	∞
t_0	50	-	10
τ	200	-	0

Table 7.4: Simulation Parameters for Run 2

Quantity	Value
Time Step	0.1
Steps	4096
Cell Size	0.2
Cells	256
Particles per Cell	500
Ion Mass	∞
Plasma Region	Cells 50-206
Thermal Speed	0.1

7.2 Stokes Dominated Simulations

In the next simulation, called "run 2", the injected frequencies are chosen based on the Stokes-dominated branches of the dispersion relation. The Stokes-dominated dispersion relations demand $\Delta\omega < 1$, so the Stokes frequency of 0.65 used previously should reflect when $A_- \gg A_+$. This is demonstrated in figure 7.4, which has already been discussed. For run 2, then, we choose a Stokes frequency of 0.85 which according to either three wave dispersion relation should propagate. All other parameters are similar to those of run 1 except the anti-Stokes amplitude which is now zero. The details are given in tables 7.3 and 7.4.

The results of run 2 are shown in figure 7.5. There is no clear evidence that EIT is taking place in a controllable fashion. Instead, the unstable mode is strongly encouraged so that electromagnetic radiation with a frequency centered at the plasma frequency emerges from the plasma. Note that the instability is strong enough to noticeably modify the pump. If EIT did take place during run 2, it apparently occured near the time $\nu_p t = 50$ where figure 7.5(d) shows a slight decrease in the reflected Stokes power. However, this apparently results from the modification to the refractive index caused by the instability, which is less controllable than one might desire.

It might be that a Stokes wave with frequency 0.85 is only marginally propagating when $A_0 = 0.3$ since the two wave dispersion relation predicts opacity in this case. We therefore repeat run 2 with a stronger pump amplitude of $A_0 = 0.35$, in which case propagation is predicted by every dispersion relation. The results are shown in figure 7.6. In this case, the instability is very strong and drastically modifies the pump wave. The transmitted spectrum shows very little amplitude at the Stokes frequency compared with what was obtained in the anti-Stokes-dominated regime. Also, the time series of figure 7.6(c) suggests that EIT does not occur the way one would expect based on the dispersion relation. In particular, there is very little energy in the interval $30 < \nu_p t < 40$. Again, the Stokes wave cannot penetrate until there is a density perturbation but there cannot be a density perturbation until the Stokes wave penetrates.

Despite the above findings, a complete dismissal of Stokes-dominated EIT is not yet possible. Simulations can only address a finite number of particular cases and can only be run for limited lengths of simulated time. It could be that very

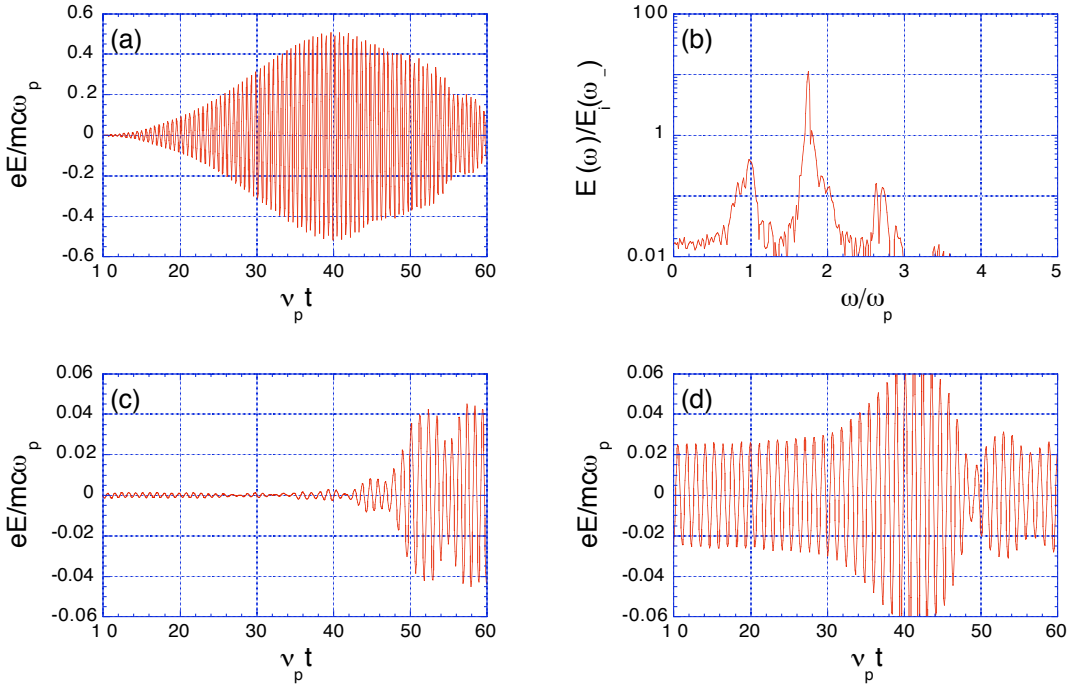

Figure 7.5: Stokes dominated case (a) transmission of pump (b) transmitted spectrum, normalized to incident Stokes feature (c) transmission of Stokes and unstable frequencies (d) reflection of Stokes and unstable frequencies

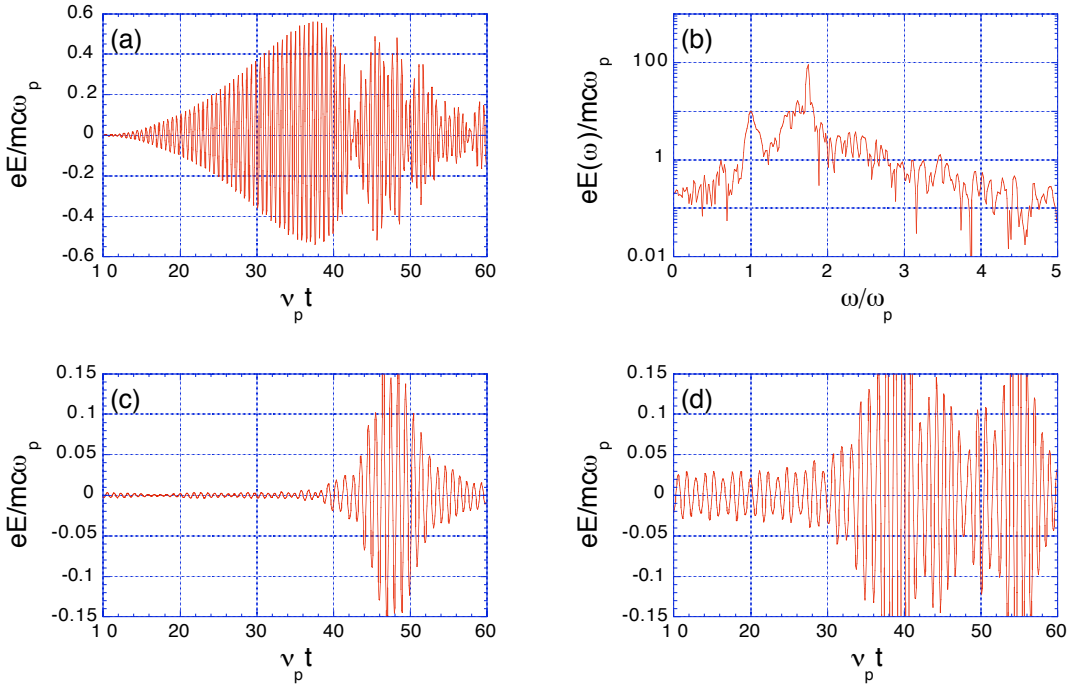

Figure 7.6: Stokes dominated case with $A_0 = 0.35$ (a) transmission of pump (b) transmitted spectrum (c) transmission of Stokes and unstable frequencies (d) reflection of Stokes and unstable frequencies

long risetimes would make it possible for the Stokes wave to be transmitted. In the next section, however, we will give an argument against this possibility.

7.3 Boundary Value Analysis

As discussed above, EIT in the anti-Stokes dominated regime is best understood in terms of the cascading of a two-frequency laser into a comb of Stokes and anti-Stokes satellites. In this section, we derive analytical expressions for the field patterns generated by a pulsed two-frequency laser interacting with a finite plasma slab. The analysis confirms the preceding simulation results, and also provides new insight into the meaning of the dispersion relation.

The analysis to be carried out works as follows. Consider a pump composed of two waves $A_1(x,t)$ and $A_2(x,t)$. Assuming there is no pump depletion, and assuming the pulse width is long compared to the plasma response time, the nonlinearly driven polarization waves induced by the pump can be explicitly described. If a Green's function can be found for the plasma slab, an integral expression for the radiation pattern due to each polarization wave can be obtained. This can be done for polarization waves oscillating at frequencies either in a passband or in a stopband. We obtain closed form expressions for the radiation pattern in each case. We also briefly consider second harmonic generation in a magnetized plasma to illustrate the general applicability of the analysis.

7.3.1 Equation for a Dispersive Slab

Consider a uniform dispersive medium contained within the interval $-l < x < l$. Consider also the vector potential A determined from

$$\left[\partial_{xx} - \partial_{tt}\right] A(x,t) = -J_L(x,t) - J_{NL}(x,t) \tag{7.5}$$

Here, the current has been expressed as the sum of a linear and nonlinear component. Fourier transforming in time we obtain

$$\left[\partial_{xx} + \omega^2\right] a(x,\omega) = -j_L(x,\omega) - j_{NL}(x,\omega) \tag{7.6}$$

where we use the Fourier transform convention

$$a(x,\omega) = \int A(x,t) e^{-i\omega t} dt \tag{7.7}$$

$$A(x,t) = \int a(x,\omega) e^{i\omega t} \frac{dt}{2\pi} \tag{7.8}$$

Using the definition $j_L = \omega^2 \chi(\omega) a$ we obtain

$$\left[\partial_{xx} + \omega^2(1+\chi)\right] a(x,\omega) = -j_{NL}(x,\omega) \tag{7.9}$$

Here, χ can be any function of x. Specializing to the case where the medium is uniform over the interval $-l < x < l$, we take χ to be independent of x and write

$$\left[\partial_{xx} + \tilde{k}^2\right] a(x,\omega) = -j_{NL}(x,\omega) \tag{7.10}$$

where

$$\tilde{k}^2 = \omega^2 \left[1 + H(l - |x|)\chi(\omega)\right] \tag{7.11}$$

and H is the Heaviside step function. We also define $\epsilon = 1 + \chi$ and $k^2 = \epsilon\omega^2$.

In the following analysis, the nonlinear current j_{NL} will be regarded as a known function. The problem therefore reduces to the problem of solving for the radiation pattern produced by a distribution of antennas placed in a dispersive slab. We will henceforth drop the subscript from j_{NL} since the only currents under explicit consideration are the nonlinear ones—the linear current has been absorbed into χ.

7.3.2 Green's Function for a Dispersive Slab

We seek to solve the equation $\hat{L}a = -j$ where

$$\hat{L} = \partial_{xx} + \tilde{k}^2(x) \tag{7.12}$$

Since $\hat{L}$ is a linear operator, the equation $\hat{L}a = -j$ can be inverted via convolution with a Green's function $G(x, x', \omega)$. In particular,

$$a = -G * j \equiv -\int G(x, x')j(x')dx' \tag{7.13}$$

where $G(x, x')$ must satisfy

$$\hat{L}(x)G(x, x') = \delta(x - x') \tag{7.14}$$

and must be consistent with some set of physically meaningful boundary conditions. Note that the frequency dependence has been suppressed.

There are two boundary conditions which must be applied to the Green's function. The first boundary condition expresses the fact that no sources exist outside the plasma. If there are no sources outside the plasma, then in each vacuum region $A(x, t)$ must contain only waves which propagate away from the

plasma. In the case $x > l$, this implies that A must satisfy the right-propagating first order wave equation:

$$(\partial_x + \partial_t)\, A = 0 \tag{7.15}$$

which in frequency space becomes

$$(\partial_x + i\omega)\, a = 0 \tag{7.16}$$

Combining this with $a = -G * j$ gives the right-hand boundary condition:

$$\partial_x G = -i\omega G \quad \text{for} \quad x > l \tag{7.17}$$

The left-hand boundary condition is obtained similarly:

$$\partial_x G = i\omega G \quad \text{for} \quad x < -l \tag{7.18}$$

The second boundary condition is the requirement that $G(x)$ and $G'(x)$ be continuous at the two plasma-vacuum interfaces. This requirement follows from the fact that $G''(x)$ is finite everywhere but at the origin.

To solve for $G(x)$ we identify it with three distinct functions, each corresponding to a particular spatial region:

$$G(x) = \begin{cases} G_-(x) & x < -l \\ G_0(x) & -l \le x \le l \\ G_+(x) & x > l \end{cases} \tag{7.19}$$

In the vacuum regions, we have

$$\left(\partial_{xx} + \omega^2\right) G_\pm = 0 \tag{7.20}$$

so that

$$G_\pm = A_\pm(x')e^{i\omega x} + B_\pm(x')e^{-i\omega x} \tag{7.21}$$

where $A_\pm$ and $B_\pm$ are chosen to match the boundary conditions. The outgoing wave boundary conditions imply that $A_+ = B_- = 0$. Setting $A = A_-$ and $B = B_+$, we then have

$$G_- = A(x')e^{i\omega x} \tag{7.22}$$

$$G_+ = B(x')e^{-i\omega x} \tag{7.23}$$

In the plasma region, we have

$$\left(\partial_{xx} + k^2\right) G_0 = \delta(x - x') \tag{7.24}$$

where again, $k^2 = \epsilon\omega^2$. The general solution to this equation is

$$G_0(x) = \frac{\sin k|x - x'|}{2k} + C(x')e^{ikx} + D(x')e^{-ikx} \tag{7.25}$$

where C and D are chosen to match the boundary conditions. The boundary conditions

$$G_\pm(\pm l) = G_0(\pm l) \tag{7.26}$$

$$\partial_x G_\pm(\pm l) = \partial_x G_0(\pm l) \tag{7.27}$$

provide four equations for the four unknowns A, B, C, and D. The solutions are

$$A(x') = B(-x') = 2e^{i\omega l}\left(\frac{\psi^2 e^{ik(l+x')} - 2\psi\cos k(l - x') + e^{-ik(l+x')}}{4ik(\psi^2 - 1)}\right) \tag{7.28}$$

$$C(x') = D(-x') = e^{-ikx'}\left(\frac{\psi^2 - 2\psi e^{2ikx'} + 1}{4ik(\psi^2 - 1)}\right) \tag{7.29}$$

where

$$\psi = \frac{\omega - k}{\omega + k}e^{-ikL} \tag{7.30}$$

and $L = 2l$ is the length of the plasma. Inserting these expressions into those for G_0 and $G_\pm$ gives

$$G_0(x, x') = \frac{\psi^2 e^{ik|x-x'|} - 2\psi\cos k(x + x') + e^{-ik|x-x'|}}{2ik(\psi^2 - 1)} \tag{7.31}$$

$$G_-(x,x') = G_0(-l,x')e^{i\omega(l+x)} \tag{7.32}$$

$$G_+(x,x') = G_0(l,x')e^{i\omega(l-x)} \tag{7.33}$$

A form of the Green's function which is convenient when constructing $G * j$ is:

$$G(x,x') = \begin{cases} \left[\alpha(l)e^{-ikx'} + \beta(l)e^{ikx'}\right] e^{i\omega(l+x)} & x < -l \\ \alpha(-x)e^{-ikx'} + \beta(-x)e^{ikx'} & -l < x < x' \\ \alpha(x)e^{ikx'} + \beta(x)e^{-ikx'} & x' < x < l \\ \left[\alpha(l)e^{ikx'} + \beta(l)e^{-ikx'}\right] e^{i\omega(l-x)} & x > l \end{cases} \tag{7.34}$$

where

$$\alpha(x) = \frac{e^{-ikx} - \psi e^{ikx}}{2ik(\psi^2 - 1)} \tag{7.35}$$

$$\beta(x) = \frac{\psi^2 e^{ikx} - \psi e^{-ikx}}{2ik(\psi^2 - 1)} \tag{7.36}$$

Note that in deriving these expressions, no assumption was made that k is a real number. Hence, the case where the support of j lies in a stopband can be analyzed by making the substitution $k = i\kappa$ in all formulas.

The Green's function is plotted for two particular cases in figure 7.7. Its physical interpretation is that it represents the fields due to a "unit mass" source concentrated at the point (x', ω) in the x-ω plane. One should note, however, that the Fourier representation of any real current $J(x,t)$ obeys the rule $j(x,\omega) = j(x,-\omega)^*$. In other words, it takes at least two points in the x-ω plane to represent real currents.

7.3.3 General Solution for a Gaussian Polarization Wave

When a Gaussian pulse drives the nonlinear current, most media will respond such that the induced polarization wave is also Gaussian. It is therefore of general

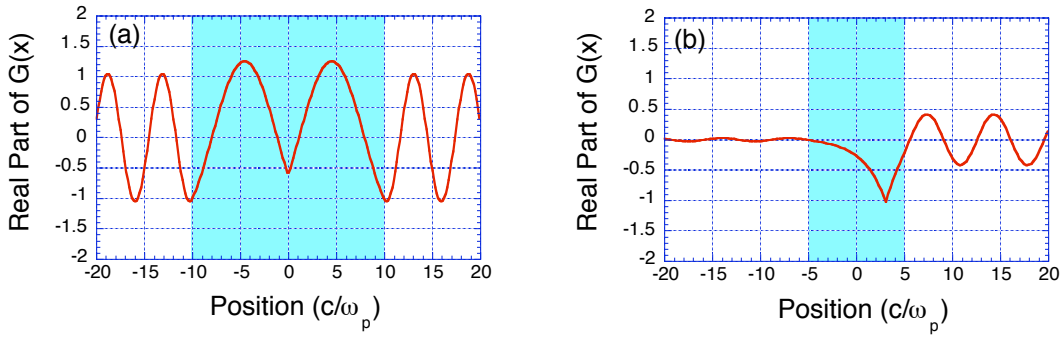

Figure 7.7: Real part of the Green's function for an isotropic plasma, which corresponds to $\epsilon = 1 - \omega_p^2/\omega^2$ (a) with a source at $x = 0$ and $\omega = 1.1\omega_p$ (b) for a source at $x = 3c/\omega_p$ and $\omega = 0.9\omega_p$. In each plot, the shaded area represents the plasma.

importance to consider a polarization wave of the form

$$J(x,t) = J_0 e^{-(t-x/v)^2/T^2} \cos(\omega_0 t - k_0 x) H(l - |x|) \tag{7.37}$$

where v represents the group velocity associated with the pump, and T is the pulse length. The parameters J_0, ω_0 and k_0 depend on both the pump and the particular nonlinear mechanism considered.

The Fourier transform of $J(x,t)$ can be found using elementary methods. The result is

$$j(x,\omega) = j_1(x,\omega) + j_2(x,\omega) \tag{7.38}$$

where

$$j_1 = \frac{J_0 H(l-|x|)}{2} T\sqrt{\pi} e^{-T^2(\omega-\omega_0)^2/4} e^{-ik_0 x} e^{-ix(\omega-\omega_0)/v} \tag{7.39}$$

$$j_2 = \frac{J_0 H(l-|x|)}{2} T\sqrt{\pi} e^{-T^2(\omega+\omega_0)^2/4} e^{ik_0 x} e^{-ix(\omega+\omega_0)/v} \tag{7.40}$$

Note that if the Gaussian profiles are narrow enough, the support of j_1 will be confined to positive frequencies and the support of j_2 will be confined to negative frequencies. In this case, it is only necessary to calculate $a_1 \equiv G * j_1$ since the negative frequency fields can then be found from

$$a_2(x,\omega) \equiv G * j_2 = a_1(x,-\omega)^* \tag{7.41}$$

The integral $G * j_1$ is straightforward to evaluate. A useful way of expressing the answer when k is real is as follows:

$$a_1 = \frac{J_0}{2} g(\omega) \begin{cases} Le^{i\omega(l+x)} \left[\alpha(l)\mathrm{sinc}\Sigma l + \beta(l)\mathrm{sinc}\Delta l\right] & x < -l \\ Le^{i\omega(l-x)} \left[\alpha(l)\mathrm{sinc}\Delta l + \beta(l)\mathrm{sinc}\Sigma l\right] & x > l \\ f_1 + f_2 + f_3 + f_4 & |x| < l \end{cases} \tag{7.42}$$

where

$$g(\omega) = T\sqrt{\pi} e^{-T^2(\omega-\omega_0)^2/4} \tag{7.43}$$

$$\mathrm{sinc}(x) = \frac{\sin(x)}{x} \tag{7.44}$$

$$\Delta = (k - k_0) - (\omega - \omega_0)/v \tag{7.45}$$

$$\Sigma = (k + k_0) + (\omega - \omega_0)/v \tag{7.46}$$

and

$$f_1 = -(x-l)\alpha(-x) e^{-i\Sigma(x+l)/2} \mathrm{sinc}\frac{\Sigma}{2}(x-l) \tag{7.47}$$

$$f_2 = (x+l)\beta(x) e^{-i\Sigma(x-l)/2} \mathrm{sinc}\frac{\Sigma}{2}(x+l) \tag{7.48}$$

$$f_3 = (x+l)\alpha(x) e^{i\Delta(x-l)/2} \mathrm{sinc}\frac{\Delta}{2}(x+l) \tag{7.49}$$

$$f_4 = -(x-l)\beta(-x) e^{i\Delta(x+l)/2} \mathrm{sinc}\frac{\Delta}{2}(x-l) \tag{7.50}$$

Note that when these expressions are evaluated on line center ($\omega = \omega_0$), Δ becomes the k-mismatch in the forward direction while Σ becomes the k-mismatch in the reverse direction. Note also that the Fourier amplitude in either vacuum region is proportional to the length of the plasma.

An alternative expression for the field, useful when k is imaginary, is as follows:

$$a_1 = J_0 \frac{g(\omega)}{\xi^2 + \kappa^2} \begin{cases} e^{i\omega(l+x)} \left[\alpha(l) i\Delta \sinh(i\Sigma l) + \beta(l) i\Sigma \sinh(i\Delta l)\right] & x < -l \\ e^{i\omega(l-x)} \left[\beta(l) i\Delta \sinh(i\Sigma l) + \alpha(l) i\Sigma \sinh(i\Delta l)\right] & x > l \\ f_1 + f_2 + f_3 + f_4 & |x| < l \end{cases} \tag{7.51}$$

where $\kappa = -ik$ and

$$\xi = k_0 + (\omega - \omega_0)/v \tag{7.52}$$

$$f_1 = -(\kappa + i\xi)\alpha(-x) e^{(\kappa - i\xi)(x+l)/2} \sinh(\kappa - i\xi)(x - l)/2 \tag{7.53}$$

$$f_2 = (\kappa + i\xi)\beta(x) e^{(\kappa - i\xi)(x-l)/2} \sinh(\kappa - i\xi)(x + l)/2 \tag{7.54}$$

$$f_3 = (\kappa - i\xi)\alpha(x) e^{-(\kappa + i\xi)(x-l)/2} \sinh(\kappa + i\xi)(x + l)/2 \tag{7.55}$$

$$f_4 = -(\kappa - i\xi)\beta(-x) e^{-(\kappa + i\xi)(x+l)/2} \sinh(\kappa + i\xi)(x - l)/2 \tag{7.56}$$

Also useful is

$$i\Delta = -\kappa - i\xi \tag{7.57}$$

$$i\Sigma = -\kappa + i\xi \tag{7.58}$$

We see that when k is imaginary, the fields do not have a clear dependence on the plasma length. Moreover, the concept of k-matching does not apply.

7.3.4 Approximate Solutions

There are important special cases where the expressions given above simplify greatly. Consider first the case where the index of refraction is not too far from unity so that $k \approx \omega$. It follows that $\psi \approx 0$ which in turn implies that

$$\alpha(x) \approx \frac{-e^{-ikx}}{2ik} \tag{7.59}$$

$$\beta(x) \ll \alpha(x) \tag{7.60}$$

Suppose further that the polarization wave is k-matched such that $\Delta l \ll 1$ and $\Sigma l \gg 1$. Then, the fields are well approximated by

$$a_1 = \frac{J_0}{4ik} g(\omega) \begin{cases} 0 & x < -l \\ -(x+l)e^{-ikx}\text{sinc}\Delta(x+l)/2 & |x| < l \\ -Le^{-ikl}e^{i\omega(l-x)}\text{sinc}\Delta l & x > l \end{cases} \tag{7.61}$$

We see that the field amplitude grows linearly across the plasma and reaches a large value when the k-mismatch is small. Thus, we recover the well known result from nonlinear optics.

Next, consider the case where k is imaginary. In this case, ψ can be expressed as

$$\psi = \frac{\omega - i\kappa}{\omega + i\kappa} e^{\kappa L} \tag{7.62}$$

which is an extremely large number if $\kappa L \gg 1$. Assuming this is so,

$$\alpha(x) \approx \frac{(\omega^2 + \kappa^2)e^{-\kappa(2l+x)} - (\omega + i\kappa)^2 e^{-\kappa(4l-x)}}{2\kappa(\omega - i\kappa)^2} \tag{7.63}$$

$$\beta(x) \approx \frac{e^{-\kappa l}}{\kappa} \frac{\omega[\sinh \kappa(x-l)] + i\kappa[\cosh \kappa(x-l)]}{\omega - i\kappa} \tag{7.64}$$

Calculation of the fields in the vacuum region is facilitated by the following additional simplification:

$$\beta(l) \approx i\frac{\omega + i\kappa}{\omega^2 + \kappa^2}e^{-\kappa l} \tag{7.65}$$

$$\alpha(l) \ll \beta(l) \tag{7.66}$$

In the plasma region, the calculation is simplified if attention is restricted to the region $|x| < l - 1/\kappa$:

$$\beta(x) \approx -\frac{e^{-\kappa x}}{2\kappa} \quad \text{for} \quad x < l - \frac{1}{\kappa} \tag{7.67}$$

$$\alpha(x) \ll \beta(x) \quad \text{for} \quad x < l - \frac{1}{\kappa} \tag{7.68}$$

With these approximations, one obtains

$$a_1 = \frac{1}{\xi^2 + \kappa^2}\begin{cases} j_1(-l,\omega)\frac{(i\kappa+\xi)(i\kappa+\omega)}{\omega^2+\kappa^2}e^{i\omega(l+x)} & x < -l \\ -j_1(x,\omega) & |x| < l - 1/\kappa \\ j_1(l,\omega)\frac{(i\kappa-\xi)(i\kappa+\omega)}{\omega^2+\kappa^2}e^{i\omega(l-x)} & x > l \end{cases} \tag{7.69}$$

If the bandwidth of $j_1(x,\omega)$ is sufficiently narrow, then the inverse transform can be obtained by evaluating all factors except for $j_1 e^{i\omega(l\pm x)}$ at $\omega = \omega_0$ and regarding them as constants within the Fourier-integral. This is equivalent to neglecting dispersion. If this can be done, then the field pattern in the time domain is

$$A(x,t) = \begin{cases} A_v e^{-(t+x+l+l/v)^2/T^2}\cos(\omega_0 t + \omega_0 x + \phi_1) & x < -l \\ A_p e^{-(t-x/v)^2/T^2}\cos(\omega_0 t - k_0 x) & |x| < l - 1/\kappa \\ A_v e^{-(t-x+l-l/v)^2/T^2}\cos(\omega_0 t - \omega_0 x + \phi_2) & x > l \end{cases} \tag{7.70}$$

where

$$A_v = \frac{J_0}{\sqrt{(\omega_0^2 + \kappa^2)(k_0^2 + \kappa^2)}} \tag{7.71}$$

$$A_p = -\frac{J_0}{k_0^2 + \kappa^2} \tag{7.72}$$

$$\phi_1 = \omega_0 l + k_0 l + \tan^{-1}\frac{\kappa}{k_0} + \tan^{-1}\frac{\kappa}{\omega_0} \tag{7.73}$$

$$\phi_2 = \omega_0 l - k_0 l + \tan^{-1}\frac{\kappa}{-k_0} + \tan^{-1}\frac{\kappa}{\omega_0} \tag{7.74}$$

In these expressions, κ is to be evaluated at $\omega = \omega_0$. Also, the positive angle solution must be used for the inverse tangent.

Several important conclusions can be immediately drawn from equation 7.70. First, in the limit $\kappa L \gg 1$, the magnitude of the field does not depend on the length of the plasma. Second, there is no k-matching condition. Third, a propagating wave exists throughout the system, always propagating away from the left plasma-vacuum interface. Finally, the field amplitude is a function of x only within $1/\kappa$ of the plasma boundaries.

7.3.5 Application to EIT in a Plasma

The analysis up to this point has been general enough to be applied to any medium with a dispersion relation $k = k(\omega)$. We now specialize to the case of a cold, isotropic plasma pumped by a two-frequency laser, or "beatwave". We first seek to describe the polarization wave induced by the beatwave. In the plasma region, let the beatwave be described by

$$A(x,t) = e^{-(t-x/v)^2/T^2}[A_1\cos(\omega_1 t - k_1 x) + A_2\cos(\omega_2 t - k_2 x)] \tag{7.75}$$

where

$$k_{1,2} = \sqrt{\omega_{1,2}^2 - 1} \tag{7.76}$$

$$v = \left|\frac{\Delta\omega}{\Delta k}\right| \tag{7.77}$$

Here, $\Delta\omega = \omega_2 - \omega_1$ and $\Delta k = k_2 - k_1$. Also, v is the group velocity and T is the pulse length. The density perturbation induced by this wave is determined from equation 5.16, which for convenience is reproduced here:

$$-(\partial_{tt} + n_0)n_1 = \partial_x n_0 \left(\int n_1 dx - \partial_x \frac{A^2}{2} \right) - n_0 \partial_{xx} \frac{A^2}{2} \tag{7.78}$$

The term containing the factor $\partial_x n_0$ vanishes everywhere except at the boundaries. We will simplify matters by dropping this term completely. Then, in the limit where $T \gg 1$, the density perturbation can be found from equation 5.19. The result is

$$n = e^{-3(t-x/v)^2/T^2} \frac{\Delta k^2}{\Delta\omega^2 - 1} \frac{A_1 A_2}{2} \cos(\Delta\omega t - \Delta k x) \tag{7.79}$$

Taking $\omega_1 < \omega_2$, the beating between this density perturbation and the A_1 wave generates the polarization wave responsible for the Stokes satellite. Similarly, the A_2 wave generates the polarization wave responsible for the anti-Stokes satellite. In each case, the polarization wave is described by equation 7.37. For the Stokes satellite, one inserts the parameters

$$J_0 = \frac{\Delta k^2}{\Delta\omega^2 - 1} \frac{A_1^2 A_2}{4} \tag{7.80}$$

$$\omega_0 = \omega_1 - \Delta\omega \tag{7.81}$$

$$k_0 = k_1 - \Delta k \tag{7.82}$$

For the anti-Stokes satellite, one inserts

$$J_0 = \frac{\Delta k^2}{\Delta\omega^2 - 1} \frac{A_1 A_2^2}{4} \tag{7.83}$$

$$\omega_0 = \omega_2 + \Delta\omega \tag{7.84}$$

Table 7.5: Beatwave Parameters

Quantity	Value
A_1	0.3
A_2	0.1
ω_1	1.75
ω_2	2.85
L	30
T	100

$$k_0 = k_2 + \Delta k \tag{7.85}$$

The radiation pattern in frequency space is then given by equation 7.42 with $k^2 = \omega^2 - 1$. Alternatively, one may use equation 7.51 with $\kappa^2 = 1 - \omega^2$.

We now consider a particular case corresponding to the parameters used for the anti-Stokes dominated EIT simulations discussed previously. One particular aim is to confirm the simulation results depicted by figure 7.3. Table 7.5 gives the relevant parameters.

Figure 7.8 shows the forward spectrum from figure 7.3 alongside the calculated spectrum, which was obtained by evaluating equation 7.42 at $x = 20$. The agreement is excellent. The only important difference is the presence of an electromagnetic mode at $\omega = 1$ in the simulated spectrum. This is a result of the Raman-type instability discussed earlier. Another difference is that the spectral amplitudes of the pumps are smaller in the case of the simulation. This is mostly because in the simulation the waveform of any injected wave is multiplied by a ramping function.

Figure 7.9 shows a plot of $|a(x, \omega)|$ computed both analytically and via simulation. The agreement between simulation and theory is adequate. The only

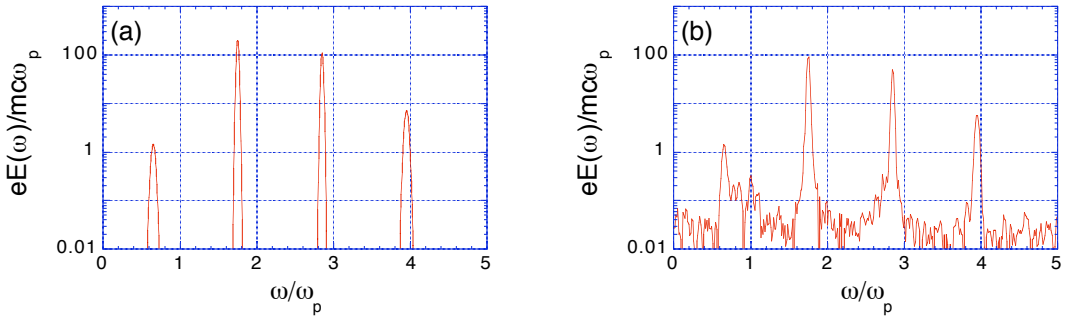

Figure 7.8: Forward spectrum from a dense beat-excited plasma (a) analytical spectrum (b) simulated spectrum. The two central features represent the beat-wave while the outer features are the satellites. The analytical spectrum was scaled to be consistent with the FFT convention.

qualitative difference is that in the case of the theory, the Stokes satellite has a larger Fourier amplitude in the plasma than in the vacuum. This may be due to the fact that the analysis ignored the effects of the steep density gradients associated with the boundaries.

Finally, figure 7.10 shows the time-domain field pattern $A(x,t)$ associated with the Stokes satellite. This was computed using the approximation of equation 7.70. Plotted alongside the analytical result is the simulated result, which was obtained by applying an FFT filter to the overall field pattern. We see that in both cases, an equal amplitude electromagnetic wave exits the plasma in both directions. Moreover, a propagating wave exists in the plasma even though the frequency is below cutoff.

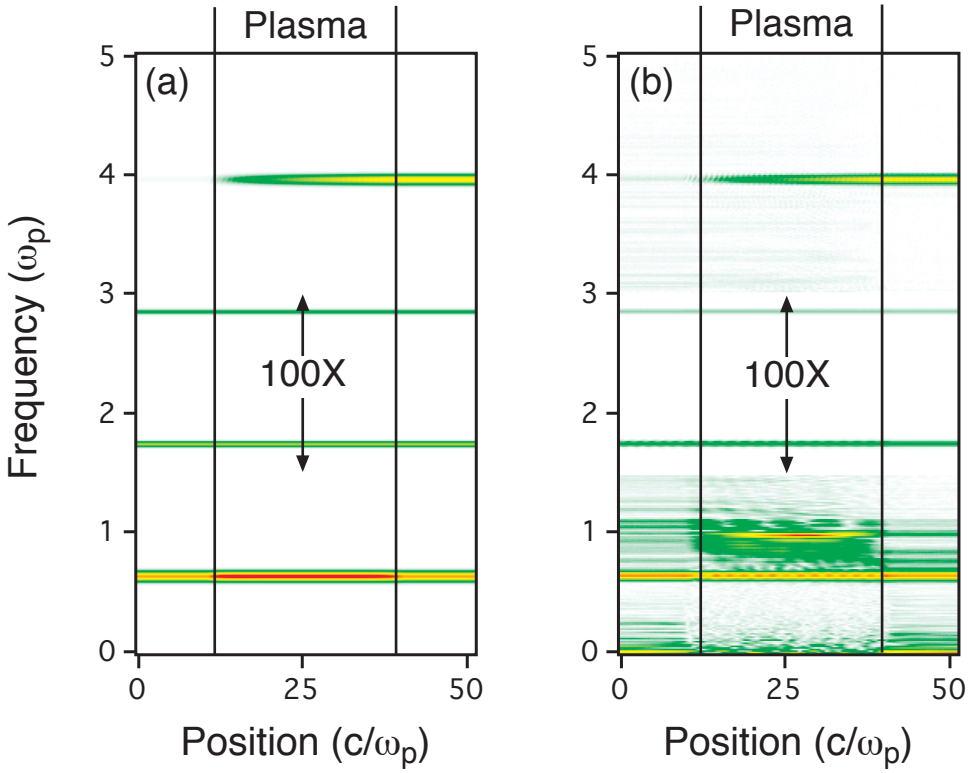

Figure 7.9: Intensity Plot of $|a(x,\omega)|$ (a) Analytical calculation (b) Simulation result. The same color scale (white < green < yellow < red) is used for both plots. The pump frequencies were attenuated by a factor of 100.

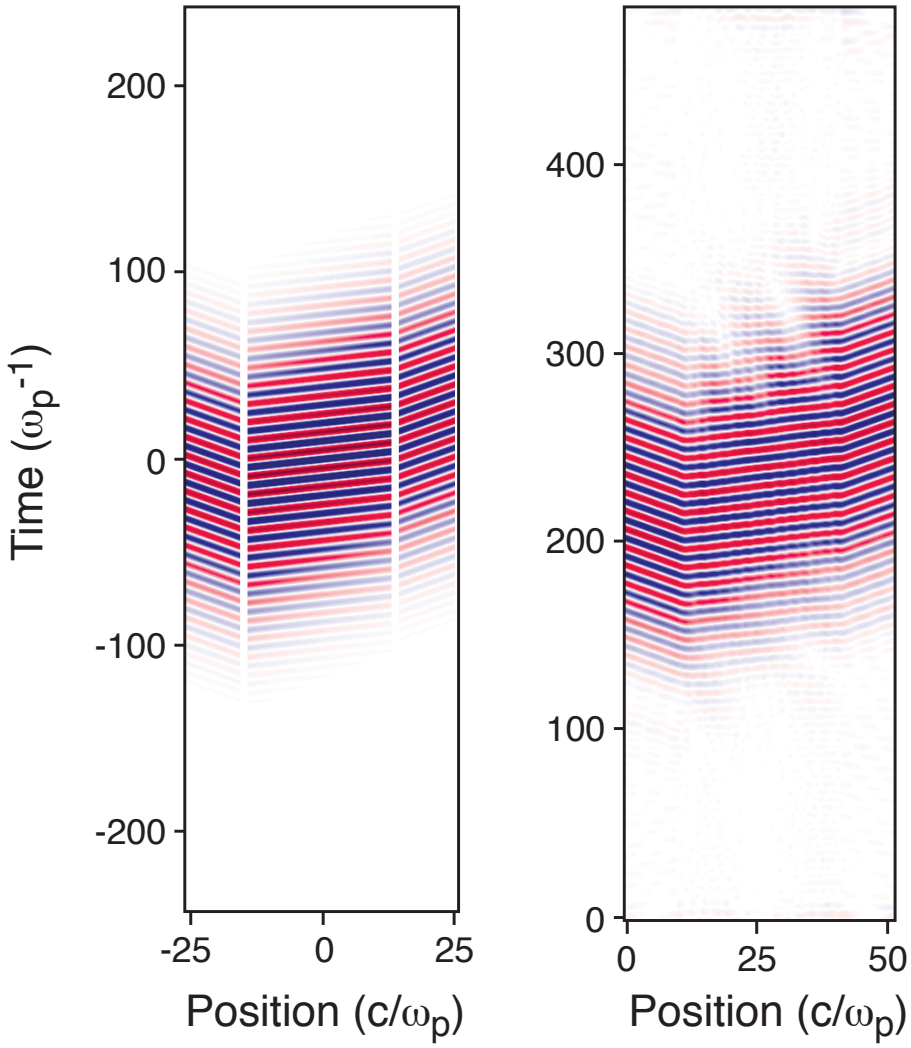

Figure 7.10: Falsecolor plot of $A(x,t)$ for the Stokes satellite. Red is positive and blue is negative. (a) Analytical calculation (b) Simulation result. The vertical white strips in the analytical plot are the regions where the approximation used is invalid. Note that the origin of the coordinate system used in each case was defined differently.

7.3.6 Interpretation and Discussion

Although the mathematics presented in this section has been involved, the physical interpretation of its meaning is simple. The integral expression for the field $a = -G * j$ is essentially a statement that the whole field pattern is obtained by adding up the fields due to an infinite number of phased antennas arrayed in the plasma. When the antennas oscillate at a frequency which lies in a stopband, the waves radiated by them are evanescent. However, when all the evanescent waves are summed up, they form together a propagating wave. This is simply because the driving term is itself a propagating wave.

The reason the Stokes wave exits the plasma in both directions is also easy to explain. As illustrated in figure 7.7, an antenna placed within a skin depth of the plasma-vacuum interface will radiate a propagating wave out of the plasma. This remains true at both boundaries. An antenna deeper in the plasma cannot contribute to the fields outside the plasma since its own field falls off exponentially. Since there cannot be any interference from sources deep within the plasma, there is no k-matching mechanism to eliminate the backward propagating radiation as in the case of the anti-Stokes. The same line of thought explains why the amplitude of the wave does not depend on the plasma length.

Strictly speaking, the analysis developed in this section can only be applied to the case of anti-Stokes dominated EIT. However, the Stokes dominated case can be interpreted from the point of view of the analysis. In the Stokes-dominated regime, there is only a single frequency pump above the plasma frequency and a Stokes wave below the plasma frequency. As discussed above, the Stokes wave can be viewed as a superposition of evanescent waves driven by the beating of

the pump wave with the plasma wave. This superposition is a propagating wave which helps maintain the plasma wave while also coupling energy back into the pump by beating with the density perturbation. The EIT passband indicated by the Raman dispersion relation is simply the equilibrium condition wherein the amplitudes of all the waves are constant.

From this point of view, it is even more clear that the realization of true EIT is prevented by considerations of causality. When boundaries are in place, the Stokes radiation leaving the plasma can be thought of as being composed of two parts. The first is the linear part, which just corresponds to the usual reflection of any incident Stokes wave. The second is the nonlinear part, which as we have seen, comes from nonlinearly driven "antennas" near the plasma boundaries. In order for these antennas to interfere with the incident wave such that transmission is achieved, their oscillation amplitude must depend on the amplitude of the incident wave, and the polarization wave associated with them must be propagating. The incident wave, however, is evanescent within the plasma. It is trivial to show that the nonlinear polarization wave associated with it is also evanescent. This evanescent polarization wave will always be confined to an area within a skin depth of the plasma boundary. Hence, transmission never occurs.

7.3.7 Application to Second Harmonic Generation

To illustrate the general applicability of the concepts described in this section, we consider very briefly the extraordinary wave, or "X-wave", of cold plasma theory. The X-wave is an electromagnetic mode propagating across, and polarized perpendicular to, a uniform magnetic field. It has two stopbands: one between zero

and the left-hand cutoff (ω_L), and another between the upper hybrid frequency (ω_h) and the right-hand cutoff (ω_R). The X-wave has a compressional component, which leads to the presence of a plasma wave whose frequency is the same as that of the electromagnetic field, and whose amplitude is proportional to that of the electromagnetic field. This implies that the electric field will drive currents at the second harmonic by beating with the density perturbation.

If the parameters are chosen correctly, the fundamental frequency (ω_0) could lie in the passband $\omega_L < \omega < \omega_h$ and the second harmonic could lie in the stopband $\omega_h < \omega < \omega_R$. We thus have another example of a nonlinear mechanism which generates a polarization wave at a frequency which lies in a stopband. Without doing any further analysis, we know immediately that if the frequencies ω_0, ω_h, and ω_R are chosen as suggested above, then equal amplitude electromagnetic waves at $2\omega_0$ should exit the plasma in both directions. Figure 7.11 shows a simulation result confirming this prediction.

7.4 Conclusions

Although EIT has been experimentally demonstrated in gas vapor, it is the conclusion of this dissertation that it will not work in a plasma. Fundamentally, this may be due to the fact that in a gas, EIT is a way of neutralizing the process of absorption, whereas in a plasma, EIT is a way of neutralizing the process of reflection. Since the process of reflection is more fundamentally dependent on boundary conditions than absorption is, it is not surprising that boundary conditions play such a crucial role in the description of EIT in a plasma.

This dissertation has shown, however, that it is possible for a two-frequency

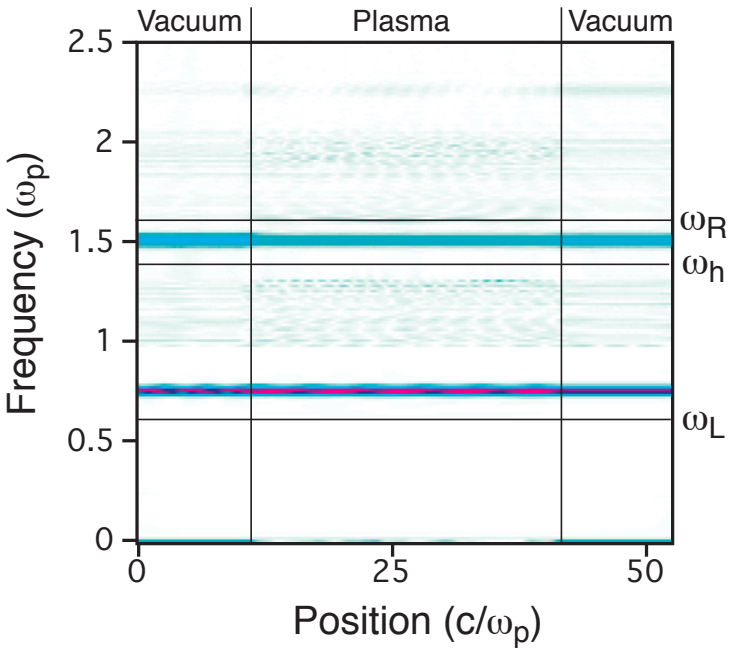

Figure 7.11: Second harmonic generation by an X-wave with $A = 0.2$ and $\omega = 0.75$. Signals with $\omega < 1$ were attenuated a factor of ten. The magnetic field is chosen such that the cyclotron frequency equals the plasma frequency. The second harmonic therefore lies in the stopband between ω_h and ω_R. As expected, radiation at $\omega = 1.5$ escapes the plasma equally in both directions.

laser to generate Stokes satellites with frequencies below the plasma frequency. In addition, we have shown that a Raman-type instability is important even when the plasma density exceeds quarter-critical. The possibility of actually observing a sub-plasma frequency Stokes satellite in an experiment depends on the interplay between the instability and the cascading process. The importance of the instability depends on the inherent noise spectrum of the plasma and the manner in which the incident pulses seed the instability. If the incident pulses are short, they will seed the instability strongly. On the other hand, if the incident pulses are long, the instability will have more time to grow. It is not immediately clear, therefore, what operating condition would be most favorable in terms of generating a clean set of cascaded frequencies.

In the case where a single frequency laser interacts with a plasma above quarter-critical, it should be possible to observe either Stokes-like or anti-Stokes-like radiation as can be seen from figure 7.5. Under certain conditions, the Stokes-like radiation might be less intense than the anti-Stokes because of the difference in group velocity. In a recent experiment at the Rutherford Appleton Laboratories in England [41], anti-Stokes radiation was indeed detected when a laser pulse interacted with a plasma above quarter critical.

Bibliography

[1] T. Tajima and J. M. Dawson. Laser electron accelerator. *Phys. Rev. Lett.*, 43(4):701–705, Jul 1979.

[2] E. Esaray *et al.* Overview of plasma-based accelerator concepts. *IEEE Trans. Plasma Sci.*, PS-24:252, 1996.

[3] S.E. Harris *et al.* Electromagnetically induced transparency in an ideal plasma. *Phys. Rev. Lett.*, 77:5357, 1996.

[4] W.B. Mori *et al.* Raman forward scattering of short-pulse high-intensity lasers. *Phys. Rev. Lett.*, 72:1482, 1994.

[5] C. Decker *et al.* Spatial temporal theory of raman forward scattering. *Phys. Plasmas*, 3:1360, 1996.

[6] P. Sprangle *et al. Phys. Rev. Lett.*, 64:2011, 1990.

[7] A. I. Akhiezer and R. V. Polovin. *Sov. Phys. JETP*, 3:696, 1956.

[8] K.C. Tzeng *et al. Phys. Rev. Lett.*, 79:5258, 1997.

[9] R. L. Williams et al. Studies of relativistic wave-particle interactions in plasma-based collective accelerators. *Lasers and Particle Beams*, 8(3):427–49, 1990.

[10] C.E. Max *et al. Phys. Rev. Lett.*, 33:209, 1974.

[11] C.E. Max. *Phys. Fluids*, 19:74, 1976.

[12] P. Sprangle *et al. IEEE Trans. Plasma Sci.*, 15:145, 1987.

[13] C.N. Danson *et al. Opt. Comm.*, 103:392, 1993.

[14] A. Septier, editor. *Focusing of Charged Particles*, chapter 4. Academic Press, New York, 1967.

[15] K.L. Brown. Technical Report 75, Stanford Linear Accelerator, 1969.

[16] J.V. Jelley. *Cherenkov Radiation and its Applications*. Pergamon Press, New York, 1958.

[17] J. Sheffield. *Plasma Scattering of Electromagnetic Radiation*. Academic Press, New York, 1975.

[18] I.H. Hutchinson. *Principles of Plasma Diagnostics*. Cambridge University Press, Cambridge, 1987.

[19] A. Modena *et al. Nature*, 377:608, 1995.

[20] A. Modena *et al. IEEE Trans. on Plasma Sci.*, 24:289, 1996.

[21] C.E. Clayton *et al.* Plasma wave generation in a self-focused channel of a relativistically intense laser pulse. *Phys. Rev. Lett.*, 81:100, 1998.

[22] C.E. Clayton *et al.* A broadband electron spectrometer and electron detectors for laser accelerator experiments. In *Particle Accelerator Conference Proceedings*, 1995.

[23] D. Gordon *et al.* Observation of electron energies beyond the linear dephasing limit from a laser-excited relativistic plasma wave. *Phys. Rev. Lett.*, 80:2133, 1998.

[24] V. Malka *et al.* Second harmonic generation and its interaction with relativistic plasma waves driven by forward raman instability in underdense plasmas. *Phys. Plasmas*, 4:1127, 1997.

[25] K.C. Tzeng and W.B. Mori. *Phys. Rev. Lett.*, 76:3332, 1996.

[26] A. Lal *et al.* Spatio-temporal dynamics of the resonantly excited relativistic plasma wave driven by a co_2 laser. *Phys. Plasmas*, 4:1434, 1997.

[27] R. Wagner *et al. Phys. Rev. Lett.*, 78:3125, 1997.

[28] M. N. Rosenbluth and C.S Liu. Excitation of plasma waves by two laser beams. *Phys. Rev. Lett.*, 29:701–705, Sep 1972.

[29] C. Decker and W.B. Mori. *Phys. Rev. E*, 51:1364, 1995.

[30] T. Katsouleas and W.B. Mori. *Phys. Rev. Lett.*, 61:90, 1988.

[31] D. W. Forslund, J. M. Kindel, W. B. Mori, C. Joshi, and J. M. Dawson. Two-dimensional simulations of single-frequency and beat-wave heating. *Phys. Rev. Lett.*, 54(6):558–561, Feb 1985.

[32] L. Gorbunov *et al. Phys. Rev. Lett.*, 76:2495, 1996.

[33] K.-J. Boller *et al. Phys. Rev. Lett.*, 66:2593, 1991.

[34] D. W. Forslund et al. Theory of stimulated scattering processes in laser-irradiated plasmas. *Phys. Fluids*, 18(8):1002–1016, Aug 1975.

[35] William L. Kruer. *The Physics of Laser Plasma Interactions.* Addison-Wesley Publishing Co., Redwood City, CA, 1988.

[36] D.F. Gordon. *EZPIC.* UCLA EE Dept., Los Angeles.

[37] R. L. Morse and C. W. Nielson. Numerical simulation of the Weibel instability in one and two dimensions. *Phys. Fluids*, 14(4):830, Apr 1971.

[38] Landau and Lifschitz. *Physical Kinetics*, chapter VI.

[39] C.J. McKinstre and R. Bingham. The modulational instability of coupled waves. *Phys. Fluids B*, 1:230, 1989.

[40] C.J. McKinstre and R. Bingham. Stimulated raman forward scattering and the relativistic modulational instability of light waves in rarefied plasma. *Phys. Fluids B*, 4:2626, 1992.

[41] R. Bingham. private communication.